Title	High-Resolution X-ray Imaging with Multi-Image X-ray Interferometer Module
Author(s)	朝倉, 一統
Citation	大阪大学, 2023, 博士論文
Version Type	VoR
URL	https://doi.org/10.18910/92190
rights	
Note	

High-Resolution X-ray Imaging with Multi-Image X-ray Interferometer Module

Kazunori Asakura
asakura_k@ess.sci.osaka-u.ac.jp

Department of Earth and Space Science,
Graduate School of Science, Osaka University

1-1, Machikaneyama, Toyonaka, Osaka 560-0043, Japan

February 22, 2023

Abstract

High-resolution X-ray imaging plays a crucial role to investigate the physical properties of X-ray astrophysical sources. Although recent X-ray observatories are equipped with imaging systems comprised of X-ray telescopes and X-ray CCDs and have revealed their spatial structure, the angular resolution has not been improved for over 20 years since the advent of the *Chandra* satellite with an exceptionally high angular resolution of $0.5''$. Whereas X-ray interferometers are proposed as alternative ways to achieve high angular resolution, they cannot fit into a size of a single satellite due to their very long baselines, which decreases the feasibility. Hence, we propose a novel X-ray imaging system, Multi-Image X-ray Interferometer Module (MIXIM), with both a very high angular resolution and a small system size. MIXIM is composed of an equally-spaced aperture mask and an X-ray imaging spectrometer, and its angular resolution is inversely proportional to the distance between them. We have performed proof-of-concept experiments with a prototype MIXIM since the invention in 2015, but its performance was quite lower than the expected one mainly due to the limited spatial resolution (4.25 μm) of the adopted sensor. In order to overcome the limit, we newly employed a sensor with a high spatial resolution of 2.5 μm and a multiple pinhole mask with a pitch of 9.6 μm, and evaluated the X-ray imaging performance of the renewed system in the synchrotron radiation facility SPring-8. Our renewed system achieved an angular resolution of $< 0.5''$ at 12.4 keV even with the system size of only ~ 1 m, which shows that MIXIM can simultaneously realize a high angular resolution and compact size. The highest angular resolution achieved in our experiments is $< 0.1''$ with a mask-sensor distance of 866.5 cm. In addition, we replaced the multiple pinhole mask with a multiple coded aperture mask, and demonstrated that such a complex aperture mask can also be used for MIXIM. MIXIM with the multiple coded aperture mask increased its effective area by about 25 times in comparison with that with the multiple pinhole mask, while maintaining a high angular resolution of $< 0.5''$ at 12.4 keV with a system size of ~ 1.5 m. Furthermore, the sensor with a small pixel size enabled us to measure X-ray polarization by tracking trajectories of photoelectrons. Our sensor has a modulation factor of 9.47% and 14.5% at 12.4 keV and 24.8 keV, respectively, which indicates that MIXIM has a potential to conduct X-ray imaging polarimetry with high angular resolution. Whereas MIXIM has some inherent restrictions (such as a narrow field of view and background-limited sensitivity) in the case of X-ray astronomical observations, these results strongly support that this novel imaging system is useful for the study of the unresolved structure of X-ray astrophysical sources.

Contents

Chapter 1

Introduction

Since the first X-ray astronomical observation with a sounding rocket in 1962, a variety of X-ray observatories were launched to obtain X-ray properties of astrophysical sources. In particular, X-ray imaging plays an important role in terms of not only morphological study but also the separation of celestial X-ray signals from background components (which also leads to the improvement of sensitivity). Although an X-ray astronomical imager started from a simple pinhole camera, the continuous development of X-ray imaging systems has improved their imaging performances. Among them, angular resolution is one of the most important features for imaging systems to investigate the spatial structure of observational targets in detail. Recent imaging systems onboard X-ray observatories are basically comprised of Wolter type I mirrors and X-ray CCDs. In this case, their angular resolutions are mainly determined by the surface roughness and alignment accuracy of the mirrors. The highest angular resolution was achieved by *Chandra*, one of the NASA's Great Observatories launched in 1999; its X-ray telescope with monolithic high-precision mirrors has an angular resolution of $0.5''$, which is considerably high in comparison with those of other X-ray observatories. Whereas a variety of discoveries thanks to the high angular resolution of *Chandra* suggests the importance of high-resolution X-ray imaging, no X-ray observatories with higher angular resolution than that of *Chandra* have appeared so far since the fabrication of high-precision X-ray mirrors has difficulty in terms of both techniques and costs.

Hence, X-ray interferometers have been proposed as other types of approaches for high-resolution X-ray imaging. The fact that astronomical observations with interferometers have already achieved high angular resolution in other wavelength bands (radio, infrared and optical bands) implies the great potential of interferometers. In 2000, the experiment of the prototype of an X-ray interferometer succeeded in obtaining interference fringes with an angular resolution of $0.1''$, which demonstrated its powerful performance. However, X-ray interferometry missions proposed so far typically necessitate a very long baseline to form interference fringes (e.g., even the aforementioned prototype required the distance between its optics and sensor to be $\sim$ 100 m). Although some ideas to reduce their baselines were suggested to increase the feasibility, no astronomical X-ray interferometers with both high angular resolution and compactness ($<$ 10 m) have appeared. It implies that currently proposed X-ray interferometry missions need a formation flight of multiple satellites, which has less feasibility due to a variety of technological requirements.

In order to realize high-resolution X-ray imaging with a more compact configuration, we proposed a novel X-ray imaging system named Multi-Image X-ray Interferometer Module (MIXIM), comprised of a mask and X-ray detector. While this system has a totally different imaging principle from other X-ray interferometers, it has a potential to achieve higher angular resolution than that of *Chandra* with only the size of $\sim$ 50 cm at 12.4 keV. Furthermore, its angular resolution can be enhanced by the extension of the distance between the mask and detector. Its unprecedented high angular resolution would reveal the detailed structure of astrophysical X-ray sources spatially-unresolved so far.

The content of this thesis is organized as follows; its basic imaging principle and development progress are summarized in section 2, and numerical calculation of the performance with the ideal configuration is given in section 3. Section 4 and 5 describe proof-of-concept experiments and obtained results with a multiple pinhole mask and multiple coded aperture mask, respectively. We also show a performance evaluation experiment of the polarimetric capability of MIXIM in section 6. In section 7, the specific features and application to X-ray astronomical observations are discussed on the basis of the experimental results mentioned in the previous sections.

Chapter 2

Reviews

In this section, we briefly review the history and recent development progress of high-resolution X-ray imaging and X-ray polarimetry, which are essential performances to grasp the characteristics of astrophysical sources especially with complicated structure. For more detailed reviews of high-resolution X-ray imaging and X-ray polarimetry, see e.g., Uttley et al. (2021)[1] and Chattopadhyay (2021),[2] respectively.

2.1 High-resolution X-ray Imaging

2.1.1 X-ray Telescope

In X-ray astronomy, an X-ray imaging system is essential to resolve the spatial structure of X-ray astrophysical sources and obtain not only morphological but also spectroscopic and photometric information for each area. In particular, angular resolution, one of the most important factors of an X-ray imaging system, has been improved in association with the advance in technology. *Uhuru*, the first X-ray astronomy satellite launched in 1970, performed a comprehensive all-sky survey for the first time, and discovered a variety of X-ray astrophysical sources (their positions and intensities were summarized as a catalog[3]). *Uhuru* restricted the incident direction of X-rays with a collimator with an angular resolution of $\sim 0.5^\circ$, while it could not perform X-ray imaging. The first imaging system for X-ray astronomy is the All-Sky Monitor (ASM) onboard Ariel V launched in 1974: a simple system with pinhole masks and position-sensitive proportional counters. Whereas ASM successfully detected time variation of some X-ray sources, its performance was insufficient to investigate the spatial structure due to its small effective area of $\sim 1\,\mathrm{cm}^2$ and poor angular resolution of $\sim 20'$.[4,5] Since the inherently low opening fraction of the pinhole mask was one of the reason of the small effective area, the application of random hole masks and coded aperture masks were subsequently proposed to enhance effective area, and actually used in e.g., solar X-ray photography onboard a Skylark rocket,[6] and the second Japanese X-ray astronomy satellite *Tenma*.[7] In particular, coded aperture masks have been used in the recent hard X-ray imaging systems such as Burst Alert Telescopes (BAT) onboard *Swift*[8] and IBIS onboard *INTEGRAL*.[9] BAT is mainly comprised of a lead coded aperture mask and a cadmium zinc telluride (CZT) detector array with an element size of $4\,\mathrm{mm} \times 4\,\mathrm{mm} \times 2\,\mathrm{mm}$. Besides, IBIS has a tungsten coded aperture mask and two detector planes: ISGRI (cadmium telluride detector array with the same pixel size as that of BAT) and PICsIT (cesium iodide scintillator array with a pixel size of $9\,\mathrm{mm} \times 9\,\mathrm{mm} \times 30\,\mathrm{mm}$). The angular resolutions of BAT and IBIS are $\sim 17'$ and $\sim 12'$, respectively, which plays an important role in e.g., determining the position of transient sources with high precision.

On the other hand, the imaging system for a soft X-ray band was dramatically advanced with the advent of focusing X-ray telescopes; *Einstein*,[10] the NASA mission equipped with an X-ray telescope for the first time, was launched in 1978, and conducted X-ray imaging with an angular resolution of $\sim 4''$ (Full Width at Half Maximum: FWHM) in a 0.15–3.0 keV band in combination with High-Resolution Imager (HRI). While HRI had relatively small effective area of $\sim 10\,\mathrm{cm}^2$ at 1 keV, the X-ray telescope could also be combined with Imaging Proportional Counter (IPC). IPC had effective area of $\sim 100\,\mathrm{cm}^2$ whereas its less spatial resolution reduced the angular resolution of $\sim 1'$. Such high-resolution imaging was achieved with the Wolter type I monolithic mirror shells made of nickel-coated fused quartz (Fig. 2.1 shows the schematic layout of the Wolter type I mirrors). Notably, the employment of focusing X-ray telescope improves not only the angular resolution but also its sensitivity. In fact, the sensitivity of *Einstein* increased by two orders of magnitude in comparison with the previous non-focusing imaging systems, which enabled *Einstein* to discover a number of serendipitous X-ray sources[11] and study the morphology of diffuse sources such as supernova remnants.[12] Such monolithic mirrors were also employed in the *ROSAT* mission;[13] *ROSAT* was equipped with 4 nested mirrors which were made of zerodur coated with a thin layer of gold, and its angular resolution was $1.7''$[14] (n.b., the angular resolution of the entire system was determined by the adopted detector). With its powerful telescope and position sensitive proportional counter, *ROSAT* completed the first imaging all-sky survey in an X-ray band.[15]

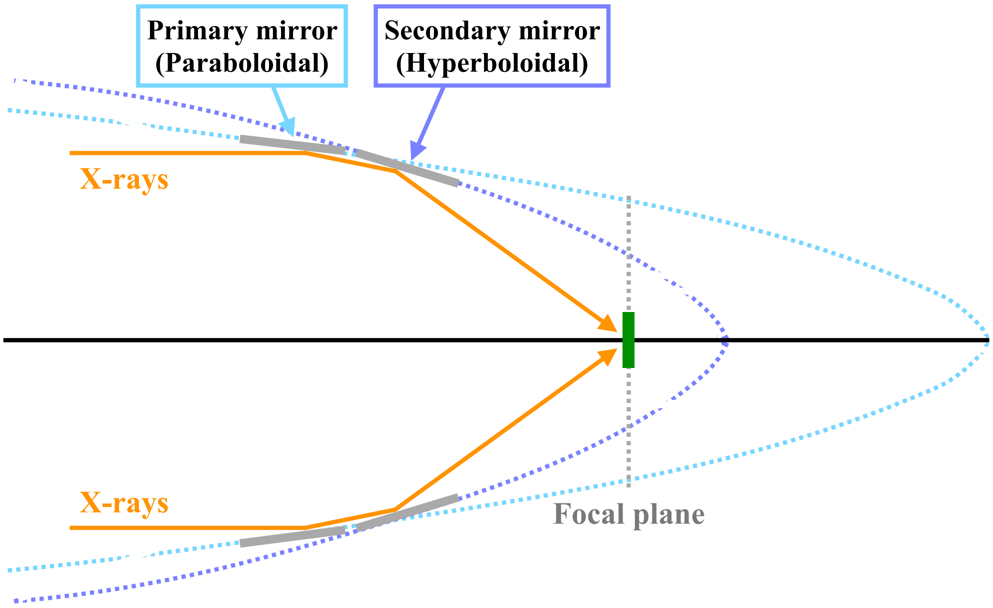

Figure 2.1: Schematic overview of the Wolter type I mirror.

Furthermore, astronomical X-ray imaging system made great progress with the successful launch of the *Chandra* X-ray Observatory[16] in 1999. Figure 2.2 and 2.3 show the illustration of the *Chandra* satellite and actual photo of its optics, High-Resolution Mirror Assembly (HRMA). HRMA consists of 4 pairs of Wolter type I mirrors made of zerodur as with the mirrors of *ROSAT* (their surfaces were polished and coated with iridium). Its large size (the diameter of HRMA is $\sim 1.2\,\mathrm{m}$) yields the effective area of $800\,\mathrm{cm}^2$ and $400\,\mathrm{cm}^2$ at 0.25 keV and 5.0 keV, respectively, whereas its long focal length of 10 m enlarges the entire size of the imaging system. The most distinctive feature is its unprecedentedly superb angular resolution of less than $0.5''$ (FWHM).[17] The focal plane detectors of HRMA is High-Resolution Camera (HRC)[18] and Advanced CCD Imaging Spectrometer (ACIS);[19] HRC is a microchannel plate instrument which has the highest spatial resolution of $\sim 20\,\mu\mathrm{m}$ (i.e., $\sim 0.4''$), while ACIS uses X-ray CCDs with a pixel size of $24\,\mu\mathrm{m}$ for X-ray spectroscopic imaging. In addition, the combination with transmission gratings enables us to perform high-resolution spectroscopy. High-resolution X-ray imaging with *Chandra* has provided a number of significant discoveries to this day (see e.g., Tananbaum et al. 2014[20] for specific results).

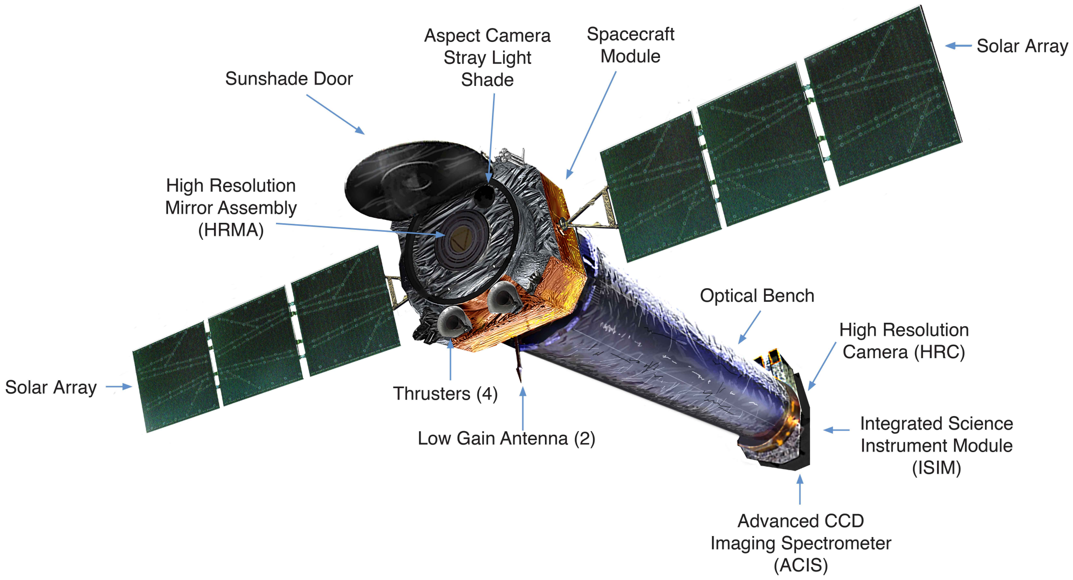

Figure 2.2: Overview of the *Chandra* X-ray Observatory (credit: NASA/CXC).

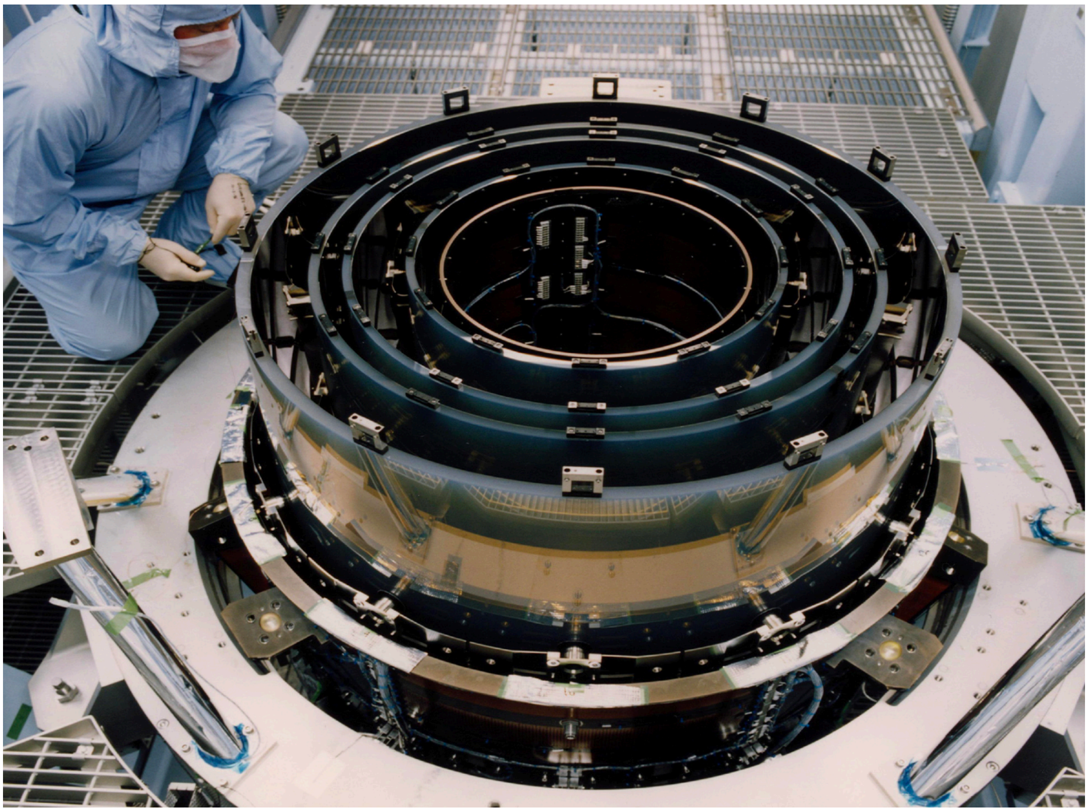

Figure 2.3: Photo of HRMA during the inspection of mirrors (credit: NASA/CXC/SAO).

After the launch of *Chandra*, a variety of X-ray observatories were subsequently launched, some of which were equipped with imaging systems comprised of different type of Wolter type I mirrors. Japanese X-ray observatories such as *Suzaku*[21] and *Hitomi*[22] employed thin-foil-nested X-ray telescopes to pursue large effective area. Such X-ray telescopes with a number of thin foils are light-weight and available with low costs in addition to their large reflecting area, though its angular resolution is not high due to the alignment inaccuracy and surface roughness of the mirrors (e.g., *Suzaku* has 4 X-ray telescopes with an effective area per telescope of $\sim 450\,\mathrm{cm}^2$ at 1.5 keV and an angular resolution of $\sim 2'$ half-power diameter[23]). On the other hand, mirror shells replicated by nickel electroforming were also adopted in some missions such as *XMM-Newton*[24] and *SRG*.[25] They have moderately high angular resolution and large effective area, since they are accurate, stable, and easily re-fabricated from a single mandrel (e.g., *SRG* is equipped with 7 X-ray telescopes, each of which has an effective area of $\sim 400\,\mathrm{cm}^2$ at 1.5 keV and an angular resolution of $16.1''$ half-power diameter[26]). Whereas these missions with nested mirror shells are superior to *Chandra* in terms of effective area, the aforementioned X-ray telescopes with thick monolithic mirror shells were especially excellent in angular resolution. In fact, *Chandra* has the highest angular resolution among existing X-ray observatories even though over 20 years have passed since the launch of *Chandra*. Notably, the angular resolution of *Chandra* is not determined by a diffraction limit but the degree of the surface smoothness and alignment accuracy of the mirrors; it implies that X-ray telescopes with much higher precision can surpass the angular resolution of *Chandra* in principle. However, it is actually unfeasible to achieve further improvement with similar type of mirrors, considering that the enormous cost in manufacturing the *Chandra* mirrors was estimated to be several hundred million dollars.[27]

2.1.2 X-ray Interferometer

As opposed to X-ray telescopes, the angular resolution of current single-dish telescopes in optical, infrared, and radio astronomy is close to the diffraction limit (in fact, the performances at optical wavelengths and radio wavelengths are mainly determined by fluctuations of air density or temperature and water vapor, respectively). Although fabrication of telescopes with a large aperture improves the angular resolution, scaling up of the telescopes has a limit in terms of feasibility. In particular, single-dish radio telescopes have difficulty in achieving high angular resolution due to a long wavelength; even a telescope with a diameter of 100 m has only an angular resolution of about $9'$ for a wavelength of 21 cm.[28] Therefore, a variety of interferometers have been studied in these wavelength bands, in order to obtain high angular resolution.

Application of interferometry to astronomy was first suggested by Fizeau in 1868 for measuring stellar diameters. This idea was implemented with a 80 cm reflector by Stephan in 1874, which derived an upper limit to stellar diameters. Afterwards, Michelson and Pease installed an improved 20-foot interferometer at the Mount Wilson Observatory and succeeded in obtaining the diameter of α Orionis (Betelgeuse) in 1921, which was the dawn of astronomical interferometry.[29] However, no progress had been made for a long time in the field of optical interferometry since that time (n.b., this type of stellar interferometers was subsequently installed at Narrabri Observatory[30] and measured various kinds of stars,[31] though it is not employed for recent optical observation due to its low sensitivity).

On the other hand, the development of interferometers was rapidly advanced in radio astronomy, since the first report of interferometric observation in a radio band in 1946.[32] Following the sea interferometer, a Michelson interferometer with a maximum spacing of $\sim 0.5\,\mathrm{km}$ was built by Ryle & Vonberg in 1946.[33] Moreover, Ryle and coworkers built a new type of an interferometer comprised of a long transit array plus a smaller moveable element, which resulted in the first star observation with the technique of aperture synthesis[34] (n.b., Blythe had previously demonstrated the aperture synthesis in 1957[35,36]). This novel technique can provide high angular resolution which cannot be obtained with single-dish telescopes in principle, and hence has been improved with the following studies (see e.g., Kellermann & Moran 2001[37] for detailed history of the development of radio interferometers). It is currently employed not only for radio telescopes (e.g., the Atacama Large Millimeter/submillimeter Array in Chile, Very Large Array in New Mexico), but also for optical and infrared telescopes (e.g., Very Large Telescope Interferometer in Chile) to overcome the restricted performance due to a diffraction limit.

In a radio band, a long wavelength enables us to get phase information with receivers as distinct from optical and infrared bands. Hence, recording the phase information at different points with two separated radio telescopes, we can calculate the cross-correlation between them electronically (the obtained cross-correlation shows a fringe pattern of which amplitude is proportional to the intensity of a source). The Fourier transform of the cross-correlation provides a visibility for a particular baseline (i.e., the spacing between the telescopes), which includes both the position and intensity of the source for a particular wavelength. Obtaining the visibility as a function of a baseline with multiple telescopes, the intensity distribution of the source is reconstructed with the inverse Fourier transform of the visibility (for detailed explanation, see e.g., Thompson et al. 2017[38]). Notably, high angular resolution necessitates an interferometer with a long baseline, since the longest baseline determines the maximum angular resolution in the case of aperture synthesis.

This technique can be also applied with multiple telescopes located throughout the world, by gathering signals from each telescope with accurate time information. It virtually makes the baseline thousands of kilometers and dramatically improves angular resolution, known as Very Long Baseline Interferometry (VLBI).

However, since phase information cannot be technically obtained in an infrared or optical band (i.e., a short wavelength), optical or infrared interferometers need to adjust light paths from telescopes to a detector with delay lines so that interference fringes appear on the detector, and directly measure the amplitude of the fringe visibility as an observable. This measurement requires the very precise adjustment of the light paths, and has to take into account phase shifts due to atmospheric fluctuation. Whereas these features made the fringe detection in these bands difficult until the early 1900s, the development of this field has steadily made progress in association with the improvement of control technology of light paths. In 1974, Labeyrie directly detected the interference fringes with an optical Michelson interferometer with a baseline of 12 m,[39] and then the Mark I stellar interferometer demonstrated photoelectric fringe detection in 1979.[40] Afterwards, the Mark II and Mark III interferometers were constructed in 1980s as a successor to the Mark I, and the Mark III with a baseline of 20 m successfully performed aperture synthesis imaging with a precision of $\sim$ 20 milliarcseconds[41] (for more detailed information, see Shao & Colavita 1992[42] and Monnier 2003[43]). In recent years, European Very Large Telescope Interferometer with four 8.2 m Unit Telescopes and movable 1.8 m Auxiliary Telescopes finished the first light in 2002, and achieved very high angular resolution with a variety of beam combiners (e.g., GRAVITY,[44] MATISSE[45]).

As with these wavelength bands, interferometers are also useful imaging systems for an X-ray band to obtain high angular resolution. X-ray interferometers also need to measure fringe visibility instead of phase information as with optical interferometers. Besides, the measuring method used in optical interferometers cannot be applied in the case of X-ray interferometry, since both complicated delay lines with multiple reflection and the light path adjustment with a wavelength-scale precision are unfeasible in an X-ray band. In addition, X-ray interferometers must be operated in space to avoid air-absorption as with existing X-ray observatories, which implies that they would have a variety of technical difficulties in comparison with optical interferometers.

The first practical X-ray interferometer was demonstrated with perfect crystals in 1965,[46] though such crystal X-ray interferometers have not been used in X-ray astronomy due to the low efficiency. Instead, a variety of interferometric approaches have been proposed for ultra-high angular resolution so far (summarized in e.g., Cash 2003[47]). Among them, pioneering X-ray interferometry projects are *MAXIM*[47] and *MAXIM pathfinder*;[48]

the goals of their angular resolutions are planned to be 0.1 micro-arcseconds and 100 micro-arcseconds, respectively. The basic design of their X-ray optics is comprised of four flat mirrors, with the “X-shape” configuration as depicted in Fig. 2.4; a pair of primary mirrors collect incident X-rays (with a wavelength of λ) to a pair of secondary mirrors, and they carry to a downstream X-ray detector. This configuration provides two different light paths which eventually intersect with different incident angles, and makes interference fringes on the detector plane. A fringe spacing s is given by $s = L\lambda/d$, where L is the distance between the secondary mirrors and detector and d is the spacing between the secondary mirrors (d is actually the baseline of this interferometer). In 2000, Cash et al. successfully detected interference fringes at 1.25 keV with an angular resolution of $0.1''$ in the laboratory, employing this type of X-ray interferometers with $d = 0.5\,\mathrm{mm}$ and $L = 100\,\mathrm{m}$.[49]

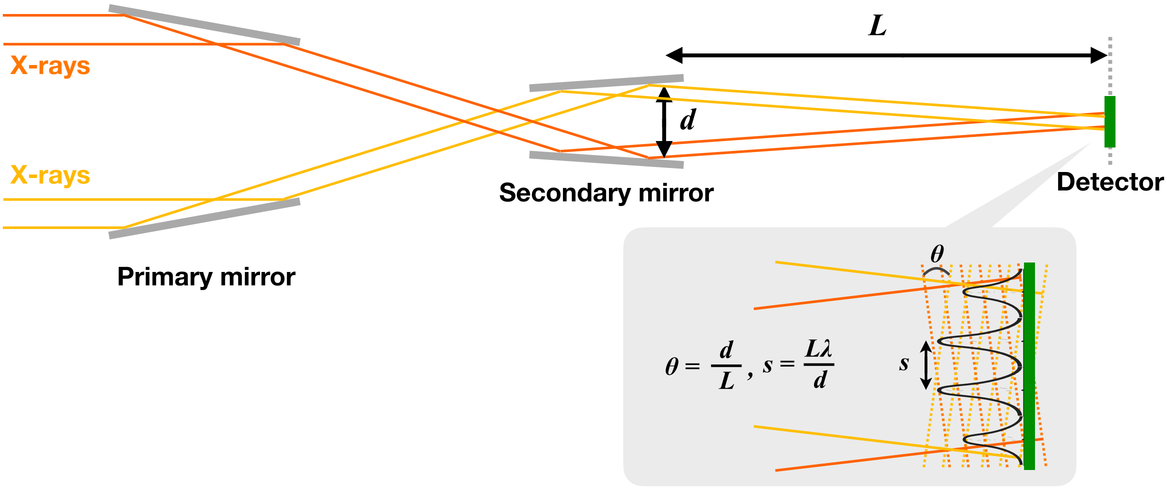

Figure 2.4: Basic design of X-ray optics employed in *MAXIM* and *MAXIM pathfinder*.

Notably, while the baseline d determines the angular resolution of the interferometer (approximated to be $\lambda/2d$), the long d decreases the fringe spacing s, which makes the fringe detection difficult with a typical X-ray detector. Specifically, when $d \sim 1\,\mathrm{m}$ and $\lambda = 1\,\mathrm{nm}$, the interferometer has an angular resolution of 100 micro-arcseconds, though the distance L has to be 200 km in order to resolve fringes with the detector with a spatial resolution of 15 µm. Whereas these interferometry projects suggested a formation flight of multiple satellites to elongate the distance L as shown in Fig. 2.5, such a long-distance formation flight with high precision is very challenging, and no X-ray interferometers have been achieved in orbit so far.

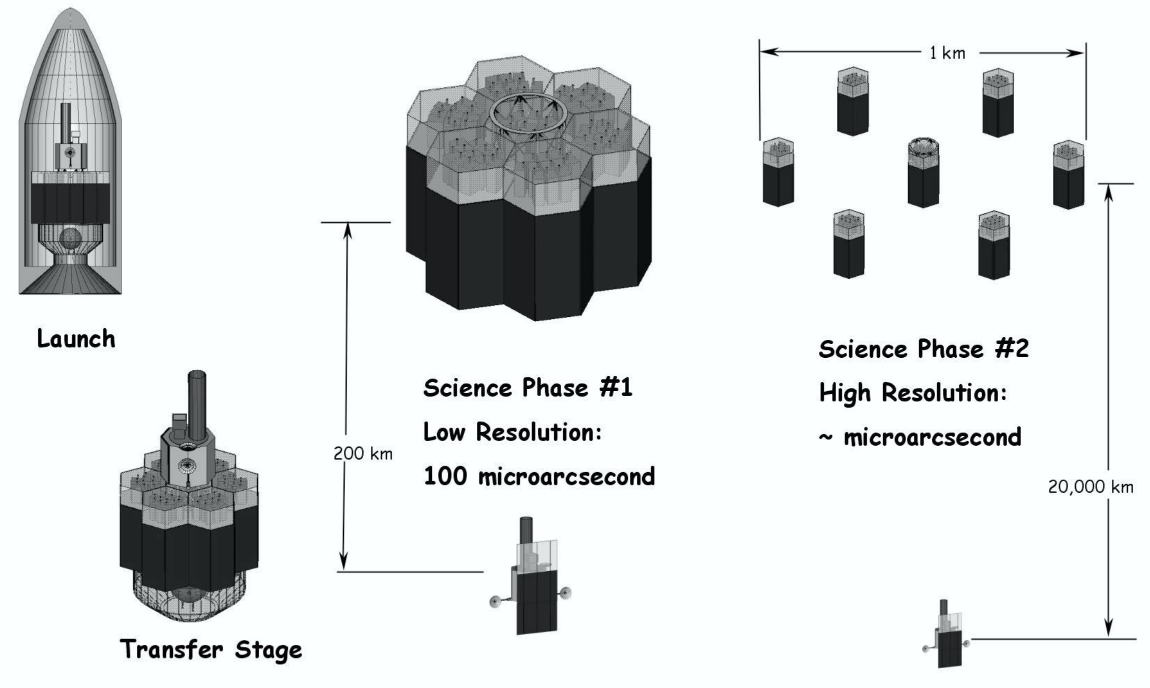

Figure 2.5: Conceptual designs of *MAXIM pathfinder* (Science Phase #1) and *MAXIM* (Science Phase #2), adapted from Fig. 4 in Gendreau et al. (2003).[48] Even *MAXIM pathfinder* necessitates the distance between the optics and detector of 200 km to resolve the fringes.

Hence, several alternative interferometers have been proposed to reduce the size and increase the feasibility. In 2004, Willingale reported the X-ray interferometer with more practical configuration as illustrated in Fig. 2.6. This interferometer could have an angular resolution of sub-milliarcseconds for 1.24 keV X-rays, even with the entire size of < 20 m. The key component for the reduction of the distance is the slatted mirror which can reflect a fraction of an incident X-ray beam. However, while the fabrication of the slatted mirror and its demonstration in an optical band have already succeeded, no interference fringes have been detected in an X-ray band since the slatted mirror requires higher precision for its shape and surface smoothness as the wavelength decreases.[50,51] In other words, it has been a serious challenge to realize an X-ray imaging system with a higher angular resolution than that of *Chandra* within the scale of a single satellite (< 10 m).

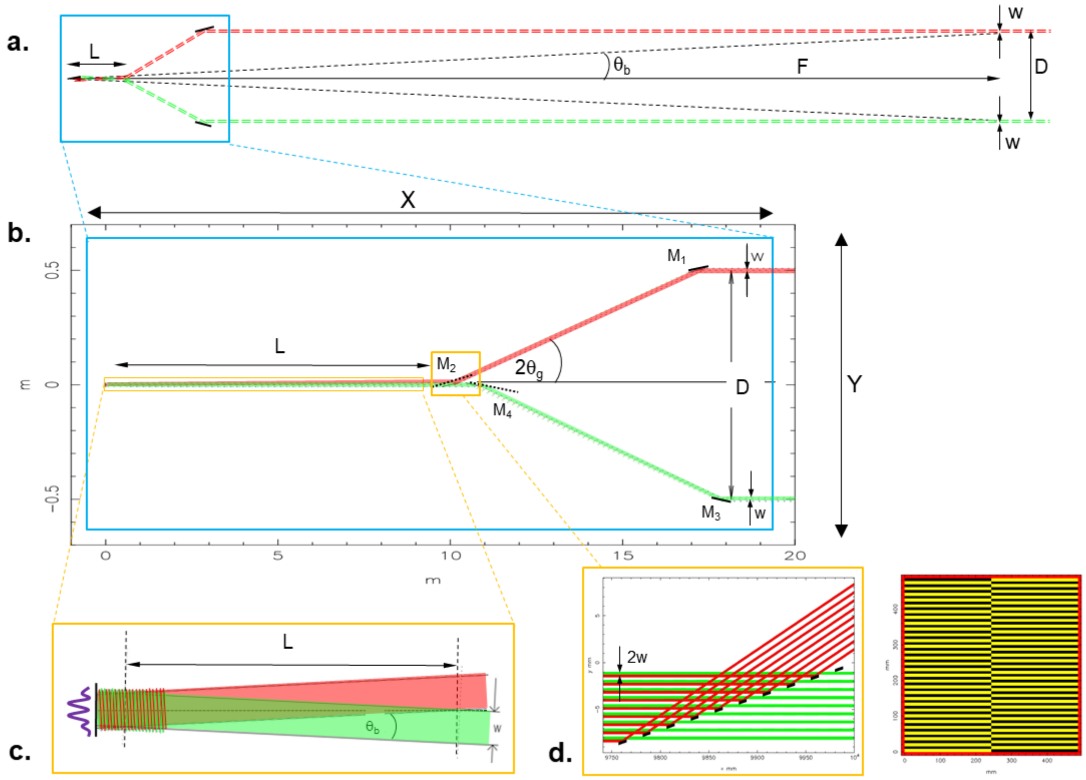

Figure 2.6: Configuration of the X-ray interferometer proposed by Willingale (Fig. 5 in Uttley et al. 2021[1]). In order to reduce the distance and improve the collecting area, it adopts the slatted mirror for the downstream mirror (M2).

2.2 X-ray Polarimetry

As with the high-resolution imaging, X-ray polarimetry is also a useful tool to diagnose the structure of astrophysical X-ray sources. When a primary X-ray photon from an astrophysical X-ray source is reflected by surrounding objects (e.g., molecular clouds), it is more likely to be emitted to the direction perpendicular to its electric field vector. It means that X-rays reflected in a particular direction are polarized even if primary X-rays are unpolarized since they include much more photons with electric field vectors perpendicular to the reflection direction. Thus, the polarization properties of reflected X-rays depend on the geometry of X-ray sources and reflectors, i.e., we can estimate their structure from the measurement of X-ray polarization, even for spatially-unresolved observational targets. (n.b., the obtained polarization includes three-dimensional geometric information which cannot be directly obtained with X-ray imaging). In addition, X-ray polarization offers the information of magnetic fields throughout the observation of synchrotron emission from relativistic electrons, since the synchrotron emission has a polarization angle perpendicular to the magnetic fields. In short, X-ray polarimetric observations give the independent restriction for such 3D geometric and magnetic structures of X-ray sources, which implies the importance of X-ray polarimetry.

The first detection of X-ray polarization from astrophysical sources was made in the observation of the Crab nebula (including its pulsar) with a sounding rocket.[52] It obtained the average polarization degree of the Crab Nebula to be $15.4\% \pm 5.2\%$ at a position angle of $156° \pm 10°$ with a confidence level of over 99%. Afterwards, the more precise polarimetric measurement with Orbiting Solar Observatory 8 (OSO-8) derived the polarization degree to be $19.2\% \pm 1.0\%$ and $19.5\% \pm 2.8\%$ at 2.6 keV and 5.2 keV, respectively.[53] Notably, since the polarimeters onboard OSO-8 had time resolutions high enough to conduct phase-resolved polarimetry for the Crab pulsar, they used only the off-pulse phase to exclude the contamination from the Crab pulsar. Though OSO-8 also observed other sources, significant polarization was obtained only for the bright X-ray binary Cygnus X-1,[54] while only upper limits were given for the observations of e.g., Cygnus X-2, Cygnus X-3,[54] Scorpius X-1,[55] Centaurus X-3 and Hercules X-1.[56] These results were partly ascribed to the fact that OSO-8 adopted Bragg-reflection type polarimeters which have very low effective areas of $< 1\,\mathrm{cm}^2$ due to their inherently narrow-bands instead of high modulation factors of nearly over 90%.[57] Following OSO-8, some missions for X-ray polarimetry were proposed; Stellar X-Ray Polarimeter[58] onboard the Spectrum-X-Gamma mission was developed for the launch in 1998, and Gravity and Extreme Magnetism Small Explorer[59] were planned to be launched in 2014. However, both missions were unfortunately cancelled, i.e., no missions for X-ray polarimetry had been launched for a few decades after the first detection of X-ray polarization from the Crab nebula.

In recent years, polarization measurements in hard X-ray and soft Gamma-ray bands have been activated, applying spectroscopic instruments as Compton-scattering type polarimeters. Defining the angle between the polarization vectors of an incident and scattered X-ray photon as θ, a differential cross section of the Compton-scattering is given by

$$\frac{d\sigma}{d\Omega} = \frac{1}{4}{r_0}^2 \left(\frac{k}{k_0}\right)^2 \left(\frac{k}{k_0} + \frac{k_0}{k} - 2 + 4\cos^2\theta\right), \tag{2.1}$$

where k_0 and k is the energy of an incident and scattered photon normalized by the electron rest mass (r_0 is a classical electron radius).[60] It indicates that photons are more likely to be scattered to the direction perpendicular to the incident X-ray polarization vector and hence Compton-scattering type polarimeters measure the angular distribution of scattered X-ray photons. The first result of such a case was the observation of the Crab nebula with

IBIS and SPI onboard *INTEGRAL*.[61–63] Although the obtained polarization information has uncertainty since these instruments were not calibrated for X-ray polarimeters, they detected polarization in the direction nearly parallel to the pulsar rotation axis above 100 keV, for both phase-averaged and off-pulse observation. These instruments also observed Cygnus X-1, and detected significantly polarized Gamma-rays only above 230 keV, which implies that the polarization was probably associated with the relativistic electrons in the jet.[64,65] As for the Crab Nebula, Soft Gamma-ray Detector (SGD) onboard *Hitomi* and Cadmium Zinc Telluride Image (CZTI) onboard *AstroSat* performed polarimetric measurements as with *INTEGRAL*, SGD detected polarized Gamma-rays in a 60–160 keV band in spite of short exposure time of ~ 5 ks,[66] while CZTI performed phase-resolved X-ray polarimetry in a 100–380 keV band and found a variation of polarization even in the off-pulse phase.[67] In addition, dedicated X-ray polarimetry balloon missions with Compton-scattering type polarimeters were proposed and some of them were actually launched, although scientific results were only performed with PoGO+ so far (the Crab nebula and Cygnus X-1).[68,69] As a short summary, Fig. 2.7 shows the energy dependence of the polarization degree and angle of the Crab nebula measured with aforementioned X-ray polarimeters, which suggests that both the phase-averaged and off-pulse plots show the higher polarization degree as the energy increases. The polarimetric observations in not a particular but wide energy range are required to grasp such a tendency.

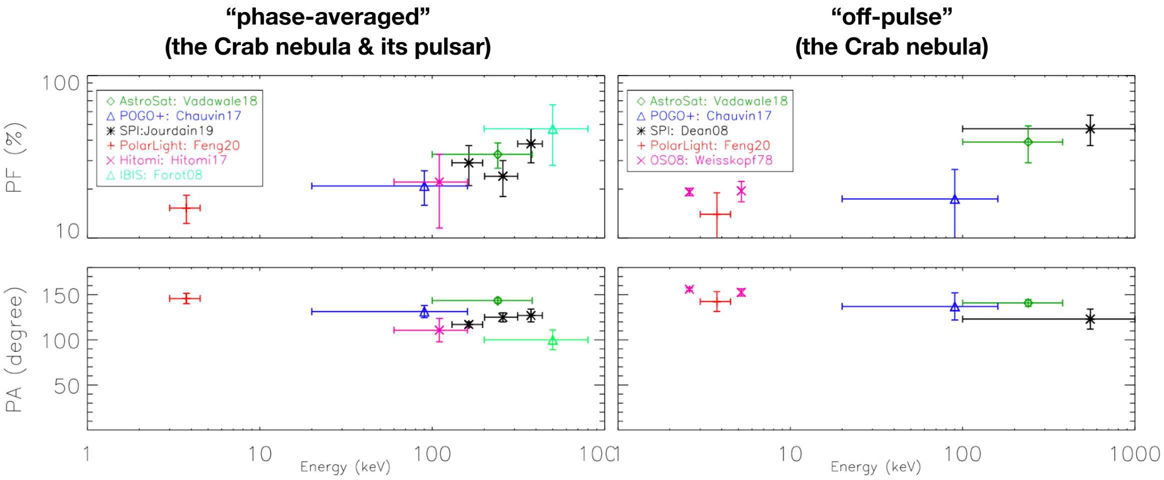

Figure 2.7: Observed energy dependence of the (top) polarization fraction and (bottom) polarization angle of the Crab nebula, adapted from Fig. 8 in Chattopadhyay (2021).[2] Left and right panels show the results of "phase-averaged" and "off-pulse" observations, respectively.

Besides the Crab nebula and Cygnus X-1, Gamma-Ray Bursts (GRBs) have been observed with X-ray polarimeters so far. Whereas IBIS and SPI reported the detections of the strong polarization from GRBs (e.g., Mcglynn et al. 2007,[70] Götz et al. 2009[71]), these detections had low levels of significance due to large systematic and statistical errors. On the other hand, Gamma-Ray Burst Polarimeter (GAP) aboard *IKAROS*, the Compton-scattering type polarimeter specifically designed for polarimetric observation of GRBs, was launched in 2010 and successfully measured the Gamma-ray polarization for three GRBs: GRB100826A, GRB110301A, and GRB110721A.[72,73] Moreover, POLAR, the instrument dedicated for GRBs observation with large effective area and a FOV, was launched as a part of Chinese Tiangong-2 Space Lab in 2016, and measured the polarization properties of a total of 14 GRBs even in less than a year (from September 2016 to April 2017) thanks to its high sensitivity.[74] Though these results still have relatively large statistical errors, the following experiment POLAR-2[75] which has larger effective area by an order of magnitude compared with POLAR will be placed aboard new Chinese space station Tiangong-3 in 2024, which can yield more precise polarimetric measurement of GRBs.

While X-ray polarimeters mentioned so far are basically Compton-scattering type and for observation in hard X-ray or soft Gamma-ray bands, *PolarLight*,[76] a 6U CubeSat mission with a different type polarimeter was recently launched and performed observation. The polarimeter onboard PolarLight is a photoelectron tracking type; it derives X-ray polarization by utilizing the anisotropy of photoelectron emission angles (a photoelectron is more likely to be emitted to the direction parallel to the X-ray polarization vector). This anisotropy is most enhanced in the K-shell photoelectric absorption, and its differential cross section is given by

$$\frac{d\sigma}{d\Omega} \propto \frac{\sin\theta^2 \cos\phi^2}{(1-\beta\cos\theta)^4}, \tag{2.2}$$

where θ and ϕ are the zenith and azimuth angles of the emitted photoelectron with respect to the X-ray polarization vector (illustrated in Fig. 2.8), and β is the speed of the photoelectron normalized by the speed of light. Whereas X-ray polarization information cannot be obtained for each photon, the distribution of emission direction statistically derived from multiple photons represents the polarization degree and angle of incident X-rays.

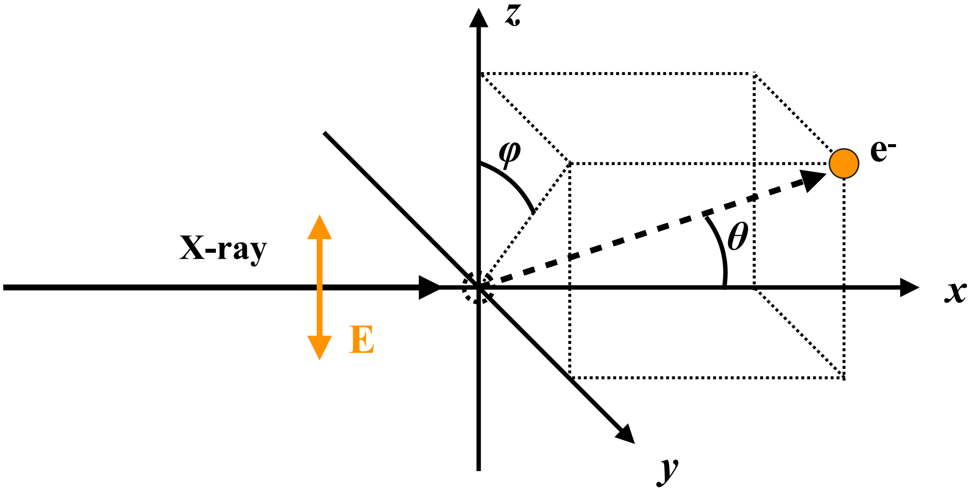

Figure 2.8: Schematic view of photo-absorption. We defined the zenith angle θ and azimuth angle ϕ based on this configuration.

Since this technique needs to measure the track images of photoelectrons, *PolarLight* employed a gas pixel detector to increase the lengths of trajectories. Figure 2.9 illustrates the structure of *PolarLight* and its gas pixel detector; when an incident X-ray photon is absorbed by the gas enclosed in the spacer, an emitted photoelectron ionizes molecules passing through the gas and yields primary electrons. The primary electrons go to gas electron multiplier (GEM) along the electric field, and the GEM converts them to a number of secondary electrons by avalanche. Then the secondary electrons are collected with the pixelated ASIC chip with a pitch of 50 µm. From the position and pulse heights of triggered pixels, the detector can obtain the energy and track image for each photon. Such a photoelectron-tracking type polarimeter can measure the polarization in a soft X-ray band where aforementioned Compton-scattering type polarimeters cannot be observed. In 2020, *PolarLight* was successfully detected the X-ray polarization from the Crab nebula in 3.0–4.5 keV,[77] which reopens the window of soft X-ray polarimetry. In addition, *PolarLight* recently detected the polarization from Scorpius X-1 in a 4–8 keV band for the first time.[78] However, *PolarLight* does not have an imaging capability due to its simple collimator system, as with previous X-ray and Gamma-ray polarimeters.

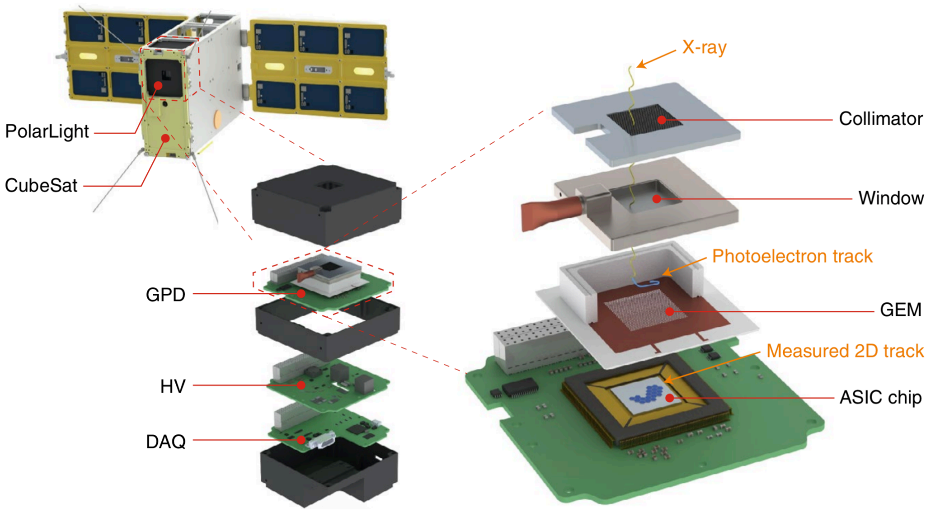

Figure 2.9: Overview of *PolarLight* and its gas pixel detector (Fig. 1 in Feng & Bellazzini 2020[79]). The detector is mainly comprised of a collimator, beryllium window, GEM and ASIC chip with a pitch of 50 µm.

Under these circumstances, Imaging X-ray Polarimetry Explorer (*IXPE*)[80] was successfully launched in December 2021. *IXPE* performed X-ray imaging polarimetry with an angular resolution of $\sim 25''$, which enables us to measure the spatially-resolved polarization information for the first time. Figure 2.10 shows the entire view; it is mainly comprised of three pairs of a mirror module assembly (MMA) and a detector unit (DU). MMA is a Wolter type I X-ray telescope which consists of 24 nested full-shell mirrors, with an effective area of 167 cm^2 and 197 cm^2 at 2.3 keV and 4.5 keV, respectively.[81] Each mirror shell was fabricated by electroformed-nickel replication (n.b., additional reflective coating inside of the mirror shell was not performed). On the other hand, DU was equipped with the gas pixel detector with a pixel size of 50 µm, as illustrated in Fig. 2.11. While the basic imaging principle is the same as that of the detector aboard *PolarLight*, the combination with MMAs enables *IXPE* to obtain the image of an observational target. The gas pixel detector has an energy resolution of $\sim 17\%$ (FWHM) at 5.9 keV, and its observable energy range is 2–8 keV; the lower and upper limits are determined by beryllium window transparency and gas absorption efficiency, respectively (for more detailed specification, see Baldini et al. 2021[82]). The imaging capability of *IXPE* is especially beneficial for the case an observational target has diffuse structure and its polarization angle varies for each area, since previous X-ray polarimetry without imaging can only measure the integrated polarization signal which results in the dilution of the polarization. In addition, *IXPE* can observe relatively dim sources whose polarization cannot be detected with previous polarimeters in terms of the sensitivity, though the effective area of *IXPE* is still quite lower in comparison with existing X-ray observatories with X-ray CCDs. Some scientific results of a variety of astrophysical sources have already reported (e.g., Cassiopeia A,[83] 4U 0142+61[84]), which provides the intriguing polarimetric features necessary to reveal the X-ray emission mechanism.

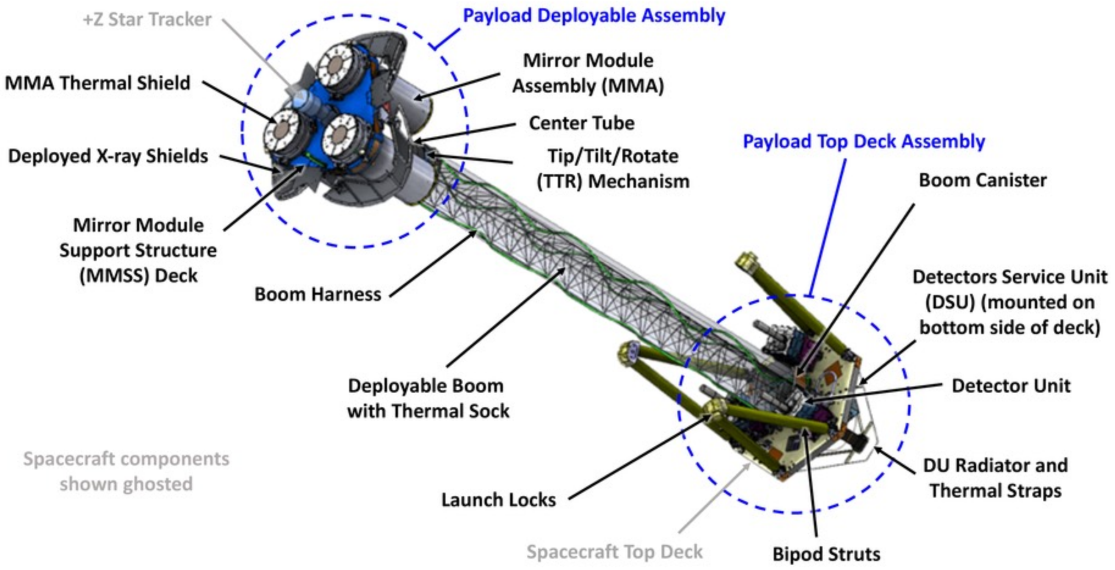

Figure 2.10: Illustration of the IXPE payload components (Fig 4. in O'Dell et al. 2019[85]). Three MMA and three DU are installed into Payload Deployable Assembly and Payload Top Deck Assembly, respectively.

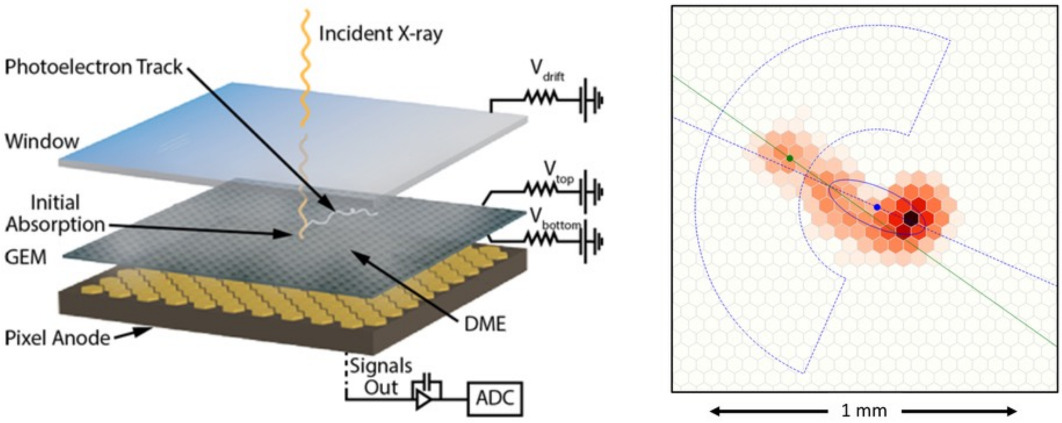

Figure 2.11: (left) Schematic view of GPD. (right) Actual photoelectron track resulting from absorption of a 5.9 keV X-ray photon (Fig. 7 in O'Dell et al. 2019[85]).

Figure 2.12 shows the summary of the recent X-ray polarimeters, along the horizontal axis of observable energy bands and the vertical axis of their spatial resolutions. It indicates that the gas pixel detectors onboard *PolarLight* and *IXPE* have the highest spatial resolution of 50 µm among the existing astronomical X-ray polarimeters. Whereas this spatial resolution is sufficient for the X-ray mirrors which currently equipped with *IXPE*, it would limit the angular resolution when we employ higher precision X-ray mirrors such as HRMA, to realize high-resolution X-ray imaging polarimetry. In addition, Fig. 2.12 implies that we have no suitable X-ray polarimeters for a 10–20 keV band, where photo-absorption cross section is dominant even for low-Z materials but gas pixel detectors have quite low absorption efficiency. This feature is also associated with the effective area of current photoelectron-tracking type polarimeters; since the absorption efficiency of the gas pixel detectors is inherently low, considerable improvement of the effective area would be challenging (even *IXPE* can observe a limited number of X-ray sources with respect to its sensitivity). Namely, a novel type of polarimeters should be developed to explore the unexploited fields of X-ray polarimetry.

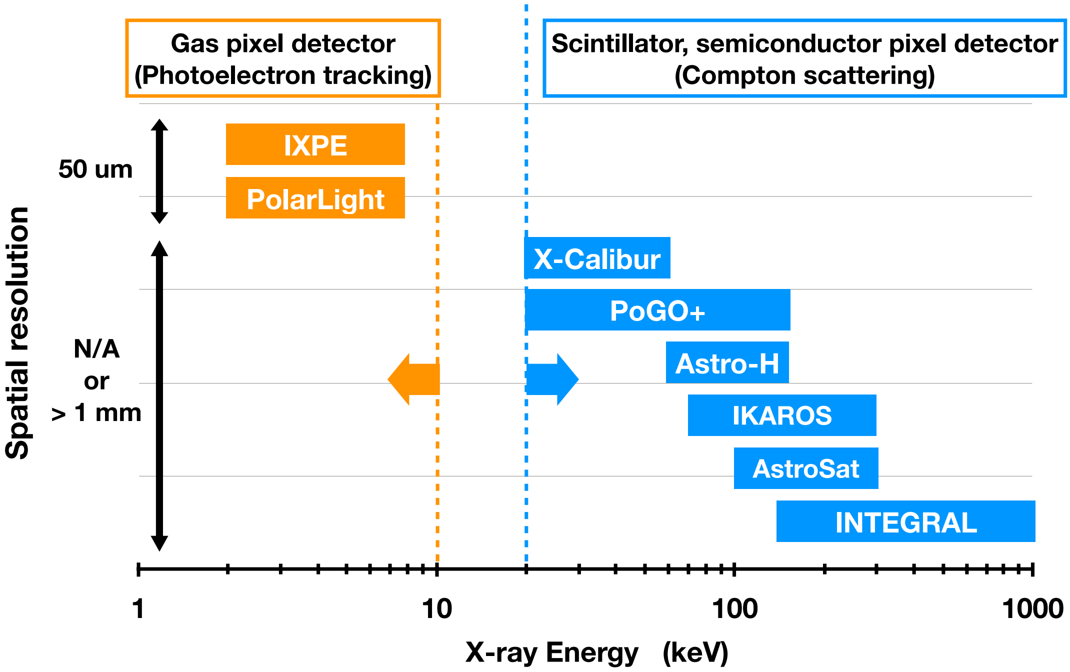

Figure 2.12: Summary of the recent X-ray and Gamma-ray polarimeters (orange: photoelectron-tracking type, blue: Compton-scattering type). The horizontal and vertical axes represent the observable energy band and spatial resolution of each polarimeter, respectively.

Chapter 3

Concepts of Novel X-ray Imaging System

As mentioned in section 2.1, the angular resolution of X-ray imaging systems plays a critical role in observing various kinds of astrophysical X-ray sources. However, recent imaging systems onboard X-ray astronomical satellites have no progress with respect to the angular resolution after the launch of *Chandra* in 1999. Therefore, we have developed Multi-Image X-ray Interferometer Module (MIXIM): a novel X-ray imaging system for achieving unprecedentedly high angular resolution.[86] Though MIXIM has the same purpose with the aforementioned X-ray interferometers, its imaging principle is totally different from those of any other imaging systems. In this section, we introduce the principle and briefly summarize the development history of MIXIM.

3.1 Principle

The imaging principle of MIXIM is basically the same as that of a slit camera, often used in X-ray astronomical imaging systems (e.g., MAXI/GSC,[87,88] MAXI/SSC[89,90]). Figure 3.1 (a) depicts the slit camera with a slit width of r and distance between the slit and detector of z. In this case, the angular resolution θ can be approximately described as rz^{-1} where $r \ll z$, which apparently suggests that reduction of the width r unlimitedly improves the angular resolution. However, in fact, a diffraction effect blurs the image and limits the angular resolution θ to $\sim \lambda/r$, as displayed in Fig. 3.1 (b).

We then focused on the Talbot effect (also referred to as the self-imaging effect), first discovered by H. F. Talbot in 1836[92] and first explained by L. Rayleigh in 1881.[93] This effect has been already applied in a variety of fields including X-ray imaging[94,95] (see the reviews by e.g., Wen et al. 2013[96]). As mentioned in Wen et al. (2013),[96] the Talbot effect is an interference phenomenon that periodic apertures form self-images for incident

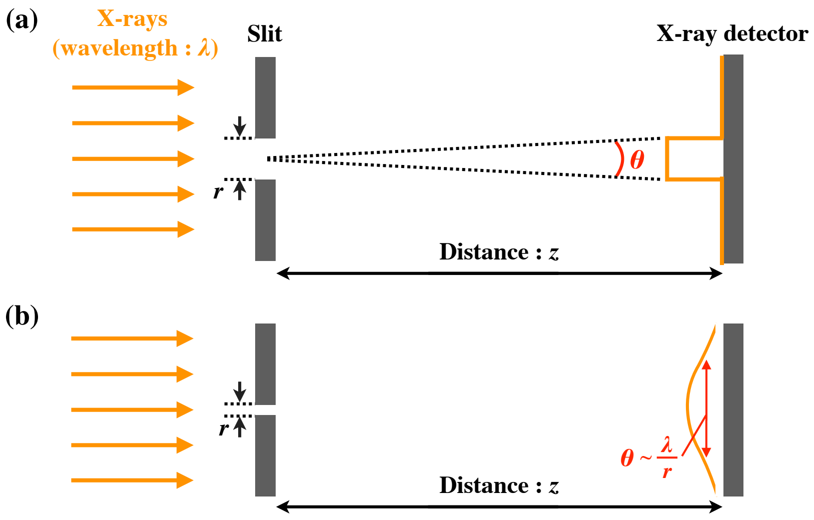

Figure 3.1: (a) Configuration of the single slit camera with a slit width of r. (b) Same as (a), but in the case where diffraction dominates (Fig. 1 in Asakura et al. 2023a[91]).

monochromatic parallel light at a distance

$$z_{\mathrm{T}} = m\frac{d^2}{\lambda}\ (m = 1, 2, 3...), \tag{3.1}$$

where d is the pitch of the apertures and λ is the wavelength of the incident light (the self-images are shifted by $d/2$ for odd integers). We applied this phenomenon to MIXIM for circumventing the diffraction problem; when we use equally-spaced multiple slits with a pitch of d and opening fraction of f instead of the single slit and adjust the distance z to satisfy Eq. 3.1 for the wavelength of our interest (hereafter we refer to it as the target wavelength), each slit forms the self-image as with the slit camera even with the fine slit width, as illustrated in Fig. 3.2. As the images are arranged with a pitch d same as the apertures, we can obtain one image with high photon statistics by stacking them, which represents the X-ray source profile at the target wavelength (actually convolved with the aperture pattern).

Notably, although this imaging principle assumes monochromatic incident X-rays, celestial objects usually have a broad band of X-rays. Hence, MIXIM adopts a photon-counting X-ray detector with a spectroscopic capability in order to extract only X-rays with the target wavelength. With the configuration illustrated in Fig. 3.2, the angular resolution in the ideal case is derived as

$$\theta = \frac{fd}{z} = 0.4'' \left(\frac{f}{0.2}\right) \left(\frac{d}{5\,\mu\mathrm{m}}\right) \left(\frac{z}{50\,\mathrm{cm}}\right)^{-1}. \tag{3.2}$$

We note that the pitch d and distance z must satisfy Eq. 3.1 for the target wavelength λ. For example, the configuration with $d = 5\,\mu\mathrm{m}$ and $z = 50\,\mathrm{cm}$ satisfies Eq. 3.1 for X-rays

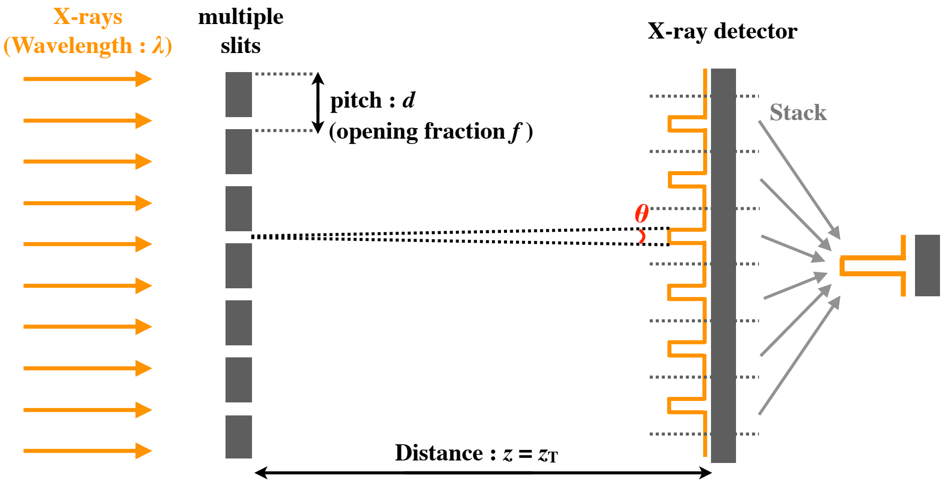

Figure 3.2: Schematic drawing of the configuration of MIXIM. The distance z_T and aperture size fd determine the angular resolution of this system, since we can eliminate the diffraction effect by the Talbot effect (Fig. 2 in Asakura et al. 2023a[91]).

with a wavelength of 0.1 nm (i.e., 12.4 keV); in this case, we can rewrite Eq. 3.2 with the wavelength λ and a positive integer m as

$$\theta = \frac{f\lambda}{dm} = 0.4'' \left(\frac{f}{0.2}\right)\left(\frac{\lambda}{0.1\,\mathrm{nm}}\right)\left(\frac{d}{5\,\mu\mathrm{m}}\right)^{-1}\left(\frac{m}{2}\right)^{-1}. \tag{3.3}$$

These equations suggest that multiple slits with a pitch of a few μm can surpass the angular resolution of *Chandra* for 12.4 keV X-rays with the typical size of micro-satellites, which indicates the potential of MIXIM as a compact imaging system with a high angular resolution.

3.2 Calculation of Diffraction Patterns

To calculate interference patterns with an arbitrary aperture, let us consider the simple configuration with a mask and a screen; the mask and screen lie in the (ξ, η) plane and (x, y) plane, respectively, and the distance between them is defined as z. When parallel monochromatic light with a wave number of k (and a wavelength of λ) perpendicularly passes through the mask, and the distance z satisfies

$$z^3 \gg \frac{\pi}{4\lambda}\left((x-\xi)^2 + (y-\eta)^2\right)^2_{\max}, \tag{3.4}$$

diffracted field amplitude $E(x, y)$ on the screen can be simplified with the Fresnel approximation, according to the following formula:

$$E(x, y) = \frac{\exp(ikz)}{i\lambda z} \int\int U(\xi, \eta) \exp\left(\frac{ik}{2z}\left[(x-\xi)^2 + (y-\eta)^2\right]\right) d\xi d\eta, \tag{3.5}$$

where i is the imaginary unit and $U(\xi, \eta)$ is the aperture function of the mask (see Goodman 2005[97] for detailed calculations). With this equation, we calculated diffraction patterns in the various cases, to evaluate the ideal performance of MIXIM before proof-of-concept experiments.

First, we calculated diffraction patterns at $z = 50$ cm for 12.4 keV X-rays with a single slit, varying the slit width r from 20 µm to 1 µm. Figure 3.3 (a) shows the result; whereas the slit with a width of a few tens of μm forms an image even if somewhat affected by a diffraction effect, the image with the 1 µm-slit is highly blurred to $\sim 20''$, which indicates that it does not function as a slit camera. On the other hand, Fig. 3.3 (b) represents the diffraction patterns at the same z with equally-spaced multiple slits ($d = 5$ µm and $f = 0.2$), varying the number of slits. Since this configuration satisfies Eq. 3.1 for 12.4 keV (corresponding to $m = 2$), the slits form self-images by the Talbot effect when the number of slits is sufficient, while the diffraction cannot be negligible with just a few slits.

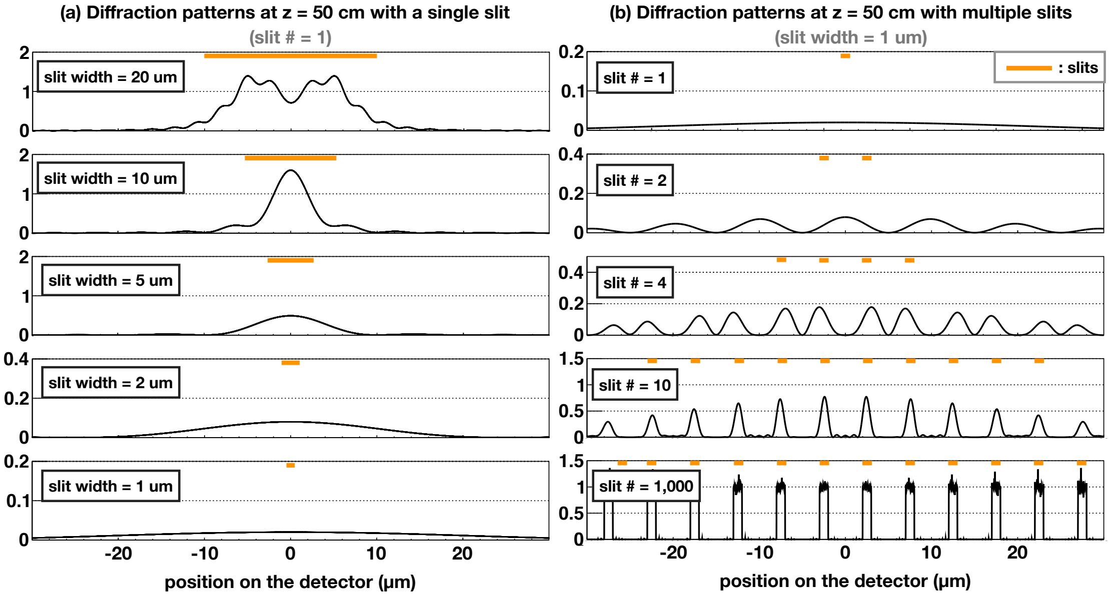

Figure 3.3: Calculated diffraction patterns for X-rays with a wavelength of 0.1 nm, in the case of the (a) single slit and (b) multiple slits (adapted from Fig. 3 in Asakura et al. 2023a[91]). Each panel of (a) and (b) shows the different slit width and the different number of slits, respectively (n.b., the range of the vertical axis is different for each panel). The slit position and width are depicted as orange lines.

In fact, these ideal patterns cannot be realized since the energy band has a non-zero width due to the limited energy resolution of the detector. Hence, we also calculated the diffraction patterns with a slit number of 1000, varying a wavelength from 0.095 nm to 0.105 nm in steps of 10^{-4} nm, and derived the accumulated patterns within the energy band ($\Delta\lambda/\lambda$) of 0%, 1%, 3%, 5% and 10% centered on 0.1 nm for each distance z. Figure 3.4 shows the plane diagram which arranges the one-dimensional intensity patterns at each distance z (so-called the Talbot carpet), for each energy band. The horizontal and vertical axes represent the distance z and slit coordinates, respectively (n.b., only a small part of the slits is displayed in Fig. 3.4). These Talbot carpets indicate that the equally-spaced multiple slits form the self-images at the distances where m is an integer, whereas the self-images are gradually blurred as m increases unless monochromatic X-rays (i.e., $\Delta\lambda/\lambda = 0$).

For particular distances at $z = 50\,\mathrm{cm}, 100\,\mathrm{cm}, 200\,\mathrm{cm}$ (corresponding to $m = 2, 4, 8$), we additionally over-plotted the accumulated patterns for each energy band, as depicted in Fig. 3.5. It indicates that the system with $z = 50\,\mathrm{cm}$ ($m = 2$) can maintain an angular resolution of $0.5''$ even with the energy band of 10%, whereas the blurring due to the extension of the energy band is increasingly high as m increases, which implies that MIXIM requires a detector with higher energy resolution as m increases for imaging at large m. However, it is not a crucial problem for MIXIM to achieve high angular resolution; the configuration with a large pitch d and a long distance z can yield a high angular resolution even with small m, and typical solid state detectors (including X-ray CCDs and CMOS sensors) have an energy resolution of about 3%, high enough to obtain the self-images for such small m.

While the calculations performed so far assume 1D-imaging with the multiple slits, we can also calculate two-dimensional diffraction patterns with e.g., a multi-pinhole mask, using Eq. 3.5. Figure 3.6 shows the assumed configuration and calculated diffraction patterns for 12.4 keV X-rays, with a 100×100 pinhole mask with a pitch of 5 μm and a pinhole radius of 1 μm. The diffraction patterns endorse that this imaging principle can be applied to 2D-imaging, only employing a 2D mask with periodic apertures (n.b., self-images can be obtained with not only such a periodic pinhole mask but also more complicated aperture patterns). These calculation results also support the high performance of MIXIM in spite of its simple and compact configuration.

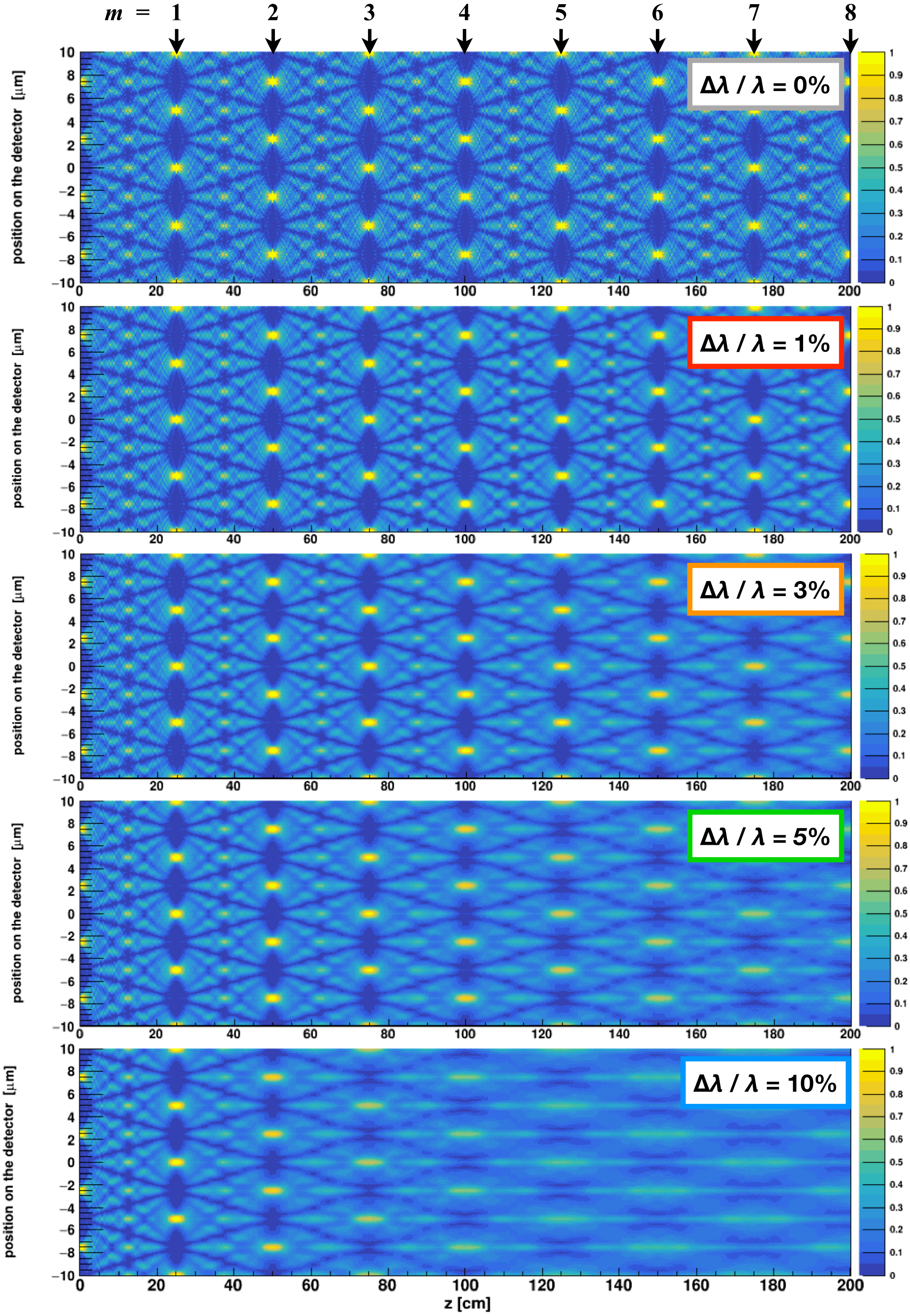

Figure 3.4: From the top panel, the Talbot carpets within the energy band ($\Delta\lambda/\lambda$) of 0%, 1%, 3%, 5% and 10%. Black arrows denote the distances where the self-images are formed by the Talbot effect (i.e., $m = 1, 2, 3...$).

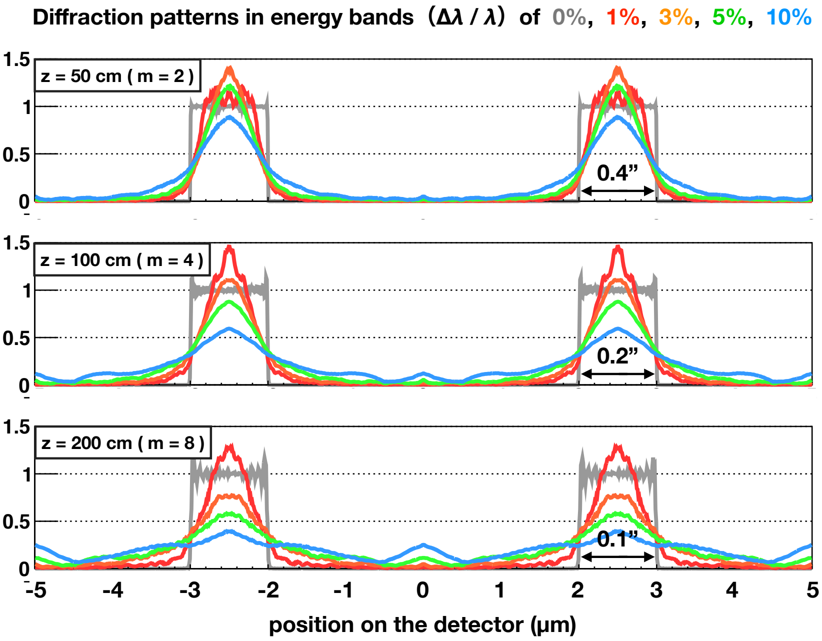

Figure 3.5: Calculated diffraction patterns within the energy band of (gray) 0%, (red) 1%, (orange) 3%, (green) 5% and (blue) 10% at three distances (Fig. 4 in Asakura et al. 2023a[91]). Black arrows show the angular widths of the self-images derived with Eq. 3.2.

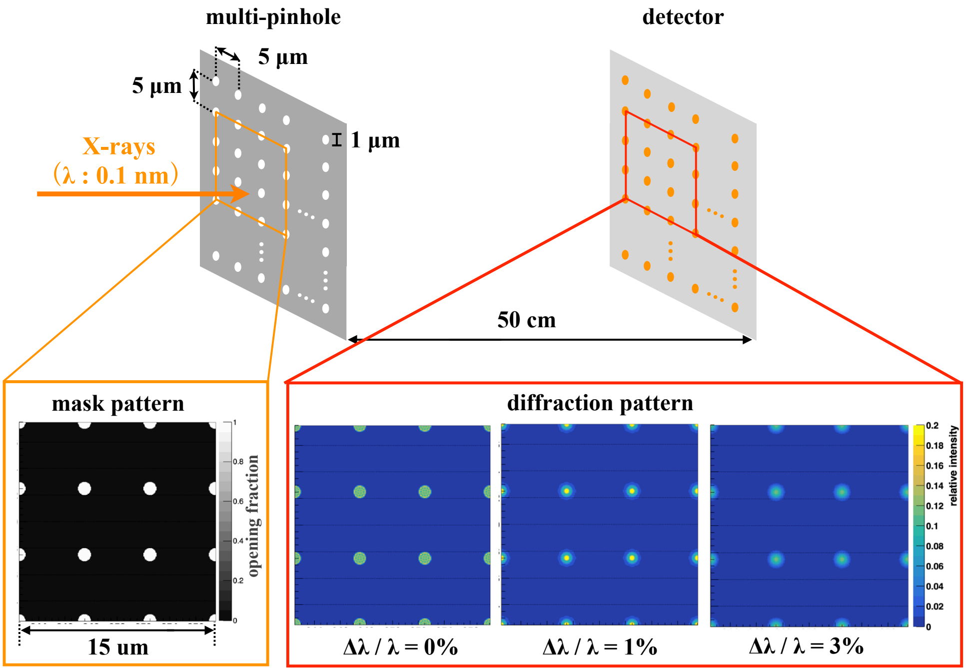

Figure 3.6: Configuration with the multi-pinhole mask and detector, and calculated 2D diffraction patterns at $z = 50\,\mathrm{cm}$ within the energy band of 0%, 1% and 3%.

3.3 Development Progress

3.3.1 Invention of MIXIM

MIXIM was originally inspired by a Talbot-Lau interferometer for X-ray phase contrast imaging.[94,95] As with X-ray absorption contrast imaging, phase contrast imaging is a method for investigating the internal structure of samples, whereas it can realize high sensitivity to low-Z materials with low absorption cross sections by utilizing phase information instead of intensity. Specifically, a Talbot-Lau interferometer is comprised of gratings and a detector as illustrated in Fig. 3.7, and obtains the phase information from the contrast of a Moiré pattern which is distorted by a sample inserted in the interferometer. Hence, accurate measurement of the contrast results in the improvement of the imaging quality.

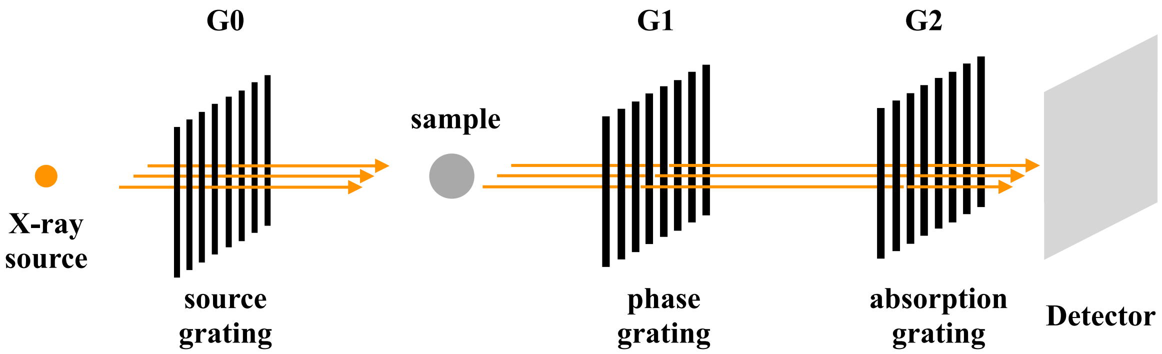

Figure 3.7: Schematic overview of the Talbot-Lau interferometer.

In medical and industrial fields, the detector used in a Talbot-Lau interferometer usually measures incident X-ray flux, with a monochromatic X-ray beam. In this case, the detector counts not only the signals originated from the X-ray beam but also background, which decreases the contrast of a Moiré pattern. We then considered the application of a detector developed for X-ray astronomy to a Talbot-Lau interferometer, in order to prevent the decrease; the detector can measure both the incident position and energy of each X-ray by operating it in the photon counting mode, which enables us to distinguish the beam signals and background by spectroscopy.

In order to demonstrate this idea, we introduced a $\pi/2$ phase grating with a pitch of 3 µm and XRPIX2b, an active pixel sensor with a pixel size of 30 µm based on the silicon-on-insulator pixel technology.[98] With these components and a micro-focus X-ray source L8321-01 manufactured by Hamamatsu Photonics, we assembled a simple system in our laboratory and irradiated 8.4 keV X-rays to the system as a first step in 2015 (shown in Fig. 3.8), to confirm that the grating could form the self-image for spherical-wave X-rays by the Talbot effect. As a consequence of the experiment, we detected the possible periodicity with a pitch of about 3.16 pixels in the obtained 8.4 keV photon count map though the amplitude of the self-image of the grating is quite low, partly due to the fact that the X-ray source had a spatial extent (the periodicity was derived with a sub-pixel analysis and folding analysis; specific procedures of these analyses are explained in section 4.2). While the performance as the prototype of a Talbot-Lau interferometer was not as good as expected, the result serendipitously implied that this configuration could be used to measure the small spatial extent of an X-ray source, i.e., high-resolution X-ray imaging, since the image on the detector is actually the convolution of the grating aperture and the X-ray source profile. Therefore, we named this novel imaging system as MIXIM, and attempted to rebuild the system for X-ray astronomical observation.

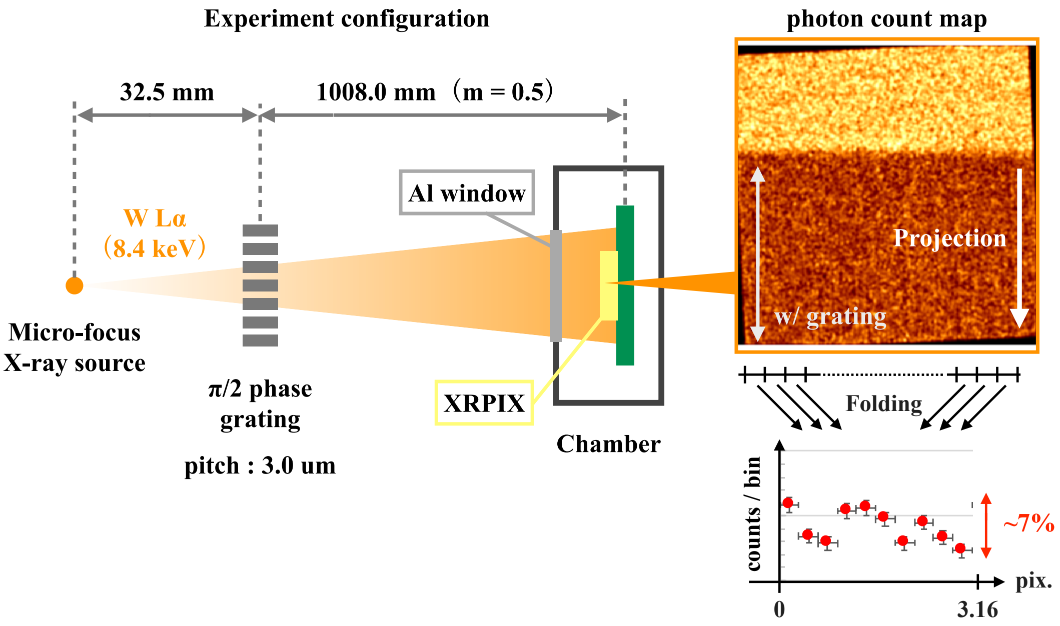

Figure 3.8: Experiment configuration with a phase grating and XRPIX2b in 2015. We detected possible self-images with a small amplitude of $\sim 7\%$ in the photon count map by folding analysis. This experiment and its result shown here was courtesy of H. Kurubi.

3.3.2 Past Proof-of-concept Experiments

In 2016, we conducted an experiment with XRPIX2b and an absorption grating with a pitch of 4.8 µm with the similar setup to the first experiment in 2015, and verified that equally-spaced self-images due to the Talbot effect appeared in the obtained photon count map (shown in Fig. 3.9). Notably, the pitch of the self-images obtained in our laboratory was elongated due to the spherical wave X-rays, which made the self-images resolvable even with the spatial resolution of XRPIX2b. However, such an elongation does not occur in the case of parallel X-rays from celestial sources, which indicates that MIXIM needs a detector with a higher spatial resolution than XRPIX2b (we note that a spatial resolution of tens of µm is sufficient if the adopted grating also has a pitch of tens of µm, though such a system requires the very long distance between the grating and sensor to utilize the Talbot effect in the X-ray regime).

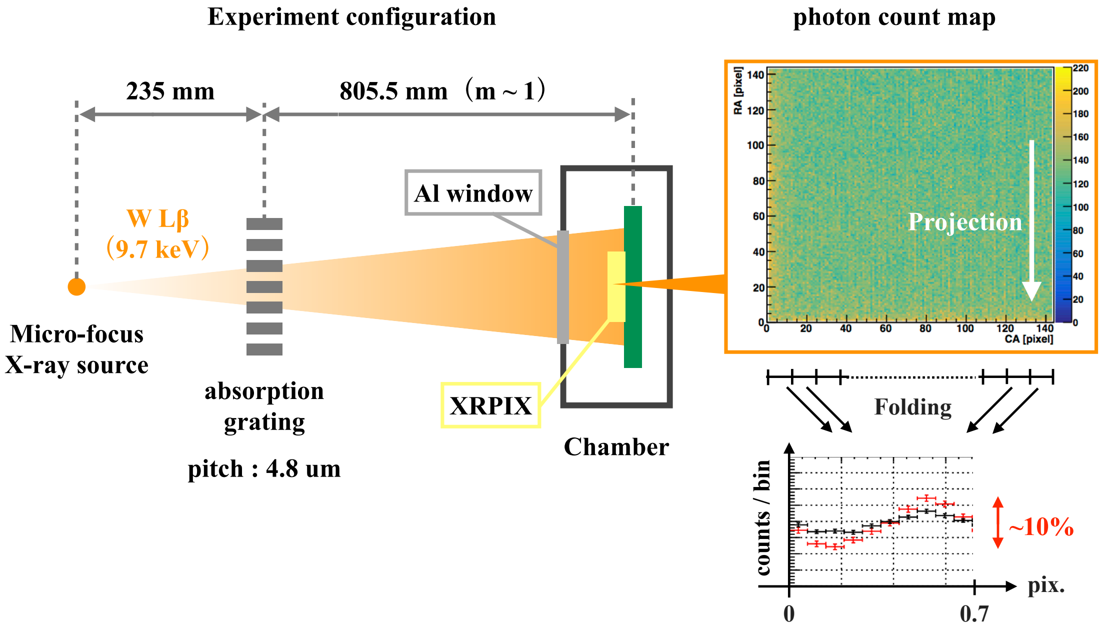

Figure 3.9: Experiment configuration with an absorption grating and XRPIX2b in 2016. The renewal of the grating slightly increased the visibility of self-images, though its amplitude was still low. This experiment and its result shown here was courtesy of T. Kawabata.

Therefore, we newly adopted GSENSE5130, a front-illuminated scientific CMOS sensor with a pixel size of 4.25 µm developed by Gpixel Inc. Though GSENSE5130 was originally developed for not X-rays but visible light, we demonstrated that it could also work as an X-ray detector with a spectroscopic imaging capability (its energy resolution was derived to be ~ 220 eV at 5.9 keV at room temperature). In 2017, we adopted this sensor and the grating with a pitch of 4.8 µm and an opening fraction of 0.5, and conducted an experiment at a beamline BL20B2 in SPring-8, the synchrotron radiation facility in Japan.[99] Since this beamline with a length of about 200 m provides an X-ray beam with a high degree of parallelization, this experiment was the first demonstration of MIXIM assuming X-ray astronomical observation. The schematic view of this experiment is illustrated in Fig. 3.10; the absorption grating and sensor were installed on the beam axis, and the distance between them z was set to be 46 cm so that the system satisfied Eq. 3.1 for a 12.4 keV X-ray beam. Although the short spacing of the self-images (~ 1.2 pixels) made the detection difficult, we successfully detected periodic patterns from the 12.4 keV photon count map. Figure 3.10 shows the schematic view of the experiment and the 1D-profile of the folded self-images. In addition, periodicity was not detected at the configuration where m was not integer, which endorsed that the obtained patterns in Fig. 3.10 were surely formed by the Talbot effect. The self-image width was calculated to be approximately $1''$ in this case, which suggests the excellent potential of MIXIM. However, the imaging performance was far from the ideal case; the highly blurred self-images had considerably low visibility, mainly due to the insufficient spatial resolution of the detector. In order to perfectly resolve the self-image and derive the original performance of MIXIM, further improvement of the spatial resolution is essential, though commercially-available X-ray CCDs and CMOS sensors did not have such a capability at that time.

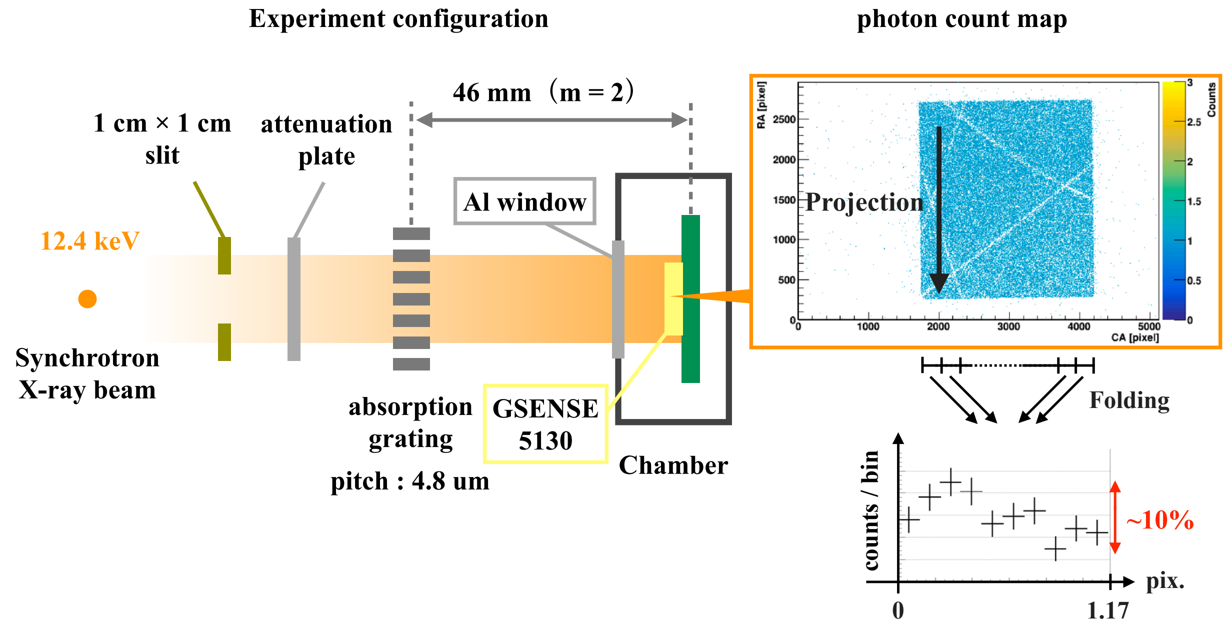

Figure 3.10: Experiment configuration with an absorption grating and GSENSE5130 in 2017. We used a 12.4 keV X-ray beam with both high degree of parallelization and high intensity in SPring-8 BL20B2, and found the periodicity of the self-images of the grating only in the case where m was an integer. This result was also courtesy of T. Kawabata.

3.3.3 Application of a New CMOS Sensor

In 2018, GMAX0505, a front-illuminated scientific CMOS sensor with a pixel size of $2.5\,\mu\mathrm{m}$, was newly released by Gpixel Inc.[100] This news was sensational for MIXIM, since it may be able to overcome the performance limit determined by the spatial resolution of the detector. Whereas this sensor was fabricated for visible light as with GSENSE5130, we immediately introduced GMAX0505, and conducted a pioneering experiment in our laboratory to evaluate its X-ray spectroscopic imaging capability. During the experiment, we removed a cover glass originally installed on the sensor, and employed a moderate gain level (with a register value of 4, $\sim 4\,\mathrm{eV/ch}$). For operation and data acquisition, we adopted an evaluation board (as displayed in Fig. 3.11) and a software which were developed by Gpixel Inc.

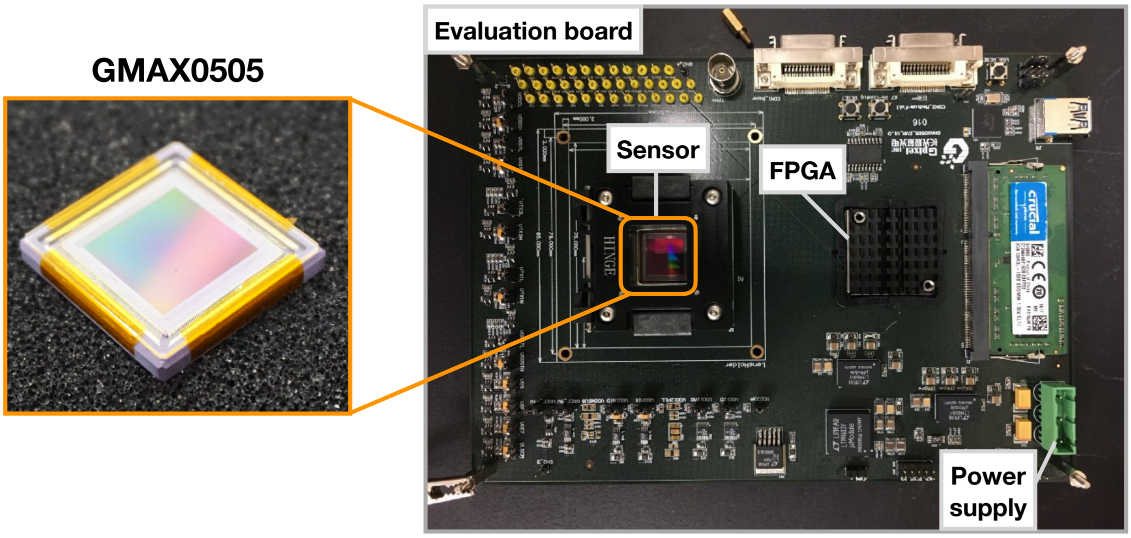

Figure 3.11: Image of (left) GMAX0505 and (right) its evaluation board provided by Gpixel Inc. The sensor was installed in a socket (denoted with the orange box) and its cover glass was removed for the experiment.

First we obtained 100 raw frame data at room temperature without X-ray irradiation, and calculated the mean and standard deviation of the pulse height for each pixel (the raw frame data consist of 5120×5120 pixels with 12-bit resolution). Figure 3.12 shows the 2D-histogram which represents the distribution of the mean and standard deviation (with an exposure time of 0.1 seconds); while the majority of pixels have a similar feature, a small fraction of pixels have irregular pulse heights, which can be incorrectly detected as X-ray events. Hence, we set a certain threshold for the mean and standard deviation as shown in Fig. 3.12, and regard the pixels which exceed the thresholds as 'bad pixel'.

We note that the distribution depends on the situation such as e.g., exposure time, a gain level and temperature of the sensor. In our experiments, when we obtained X-ray irradiation data with a certain gain and exposure time, we also took frame data without X-ray irradiation in the same condition and derived the appropriate thresholds to eliminate bad pixels.

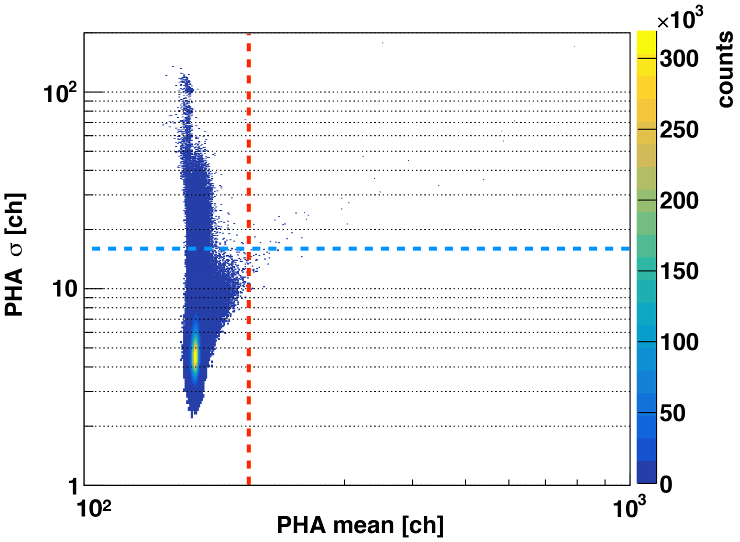

Figure 3.12: 2D-histogram which shows the distribution of the mean and standard deviation of each pixel's pulse height. Red and blue dashed lines represent the upper thresholds for the mean and standard deviation, respectively.

Afterwards, we obtained raw frame data with X-ray irradiation from ^{55}Fe. Figure 3.14 shows a part of X-ray events in the raw frames, which had pulse heights much higher than the dark level. In order to extract these X-ray events, we utilized event selection algorithm which is the almost same as that adopted in Soft X-ray Imager onboard Astro-H;[101] after dark level subtraction, the information of 5×5 pixels centered on the pixel whose pulse height surpasses an event threshold (75 ch) is extracted as an X-ray event. Notably, the dark level for each pixel is continuously updated with the pulse heights of the pixel in the previous few frames (except when the pixel detects an X-ray event), since it is different for each pixel and time-variable. In our analyses, extracted X-ray events are classified into three types based on the pulse heights of neighboring pixels as illustrated in Fig. 3.13: single pixel events (all X-ray signals reside within a pixel), double-pixel events (signals stride across two pixels), and extended events (signals spread over multiple pixels). The pixels whose pulse heights are less than a split threshold (45 ch) are ignored in this classification.

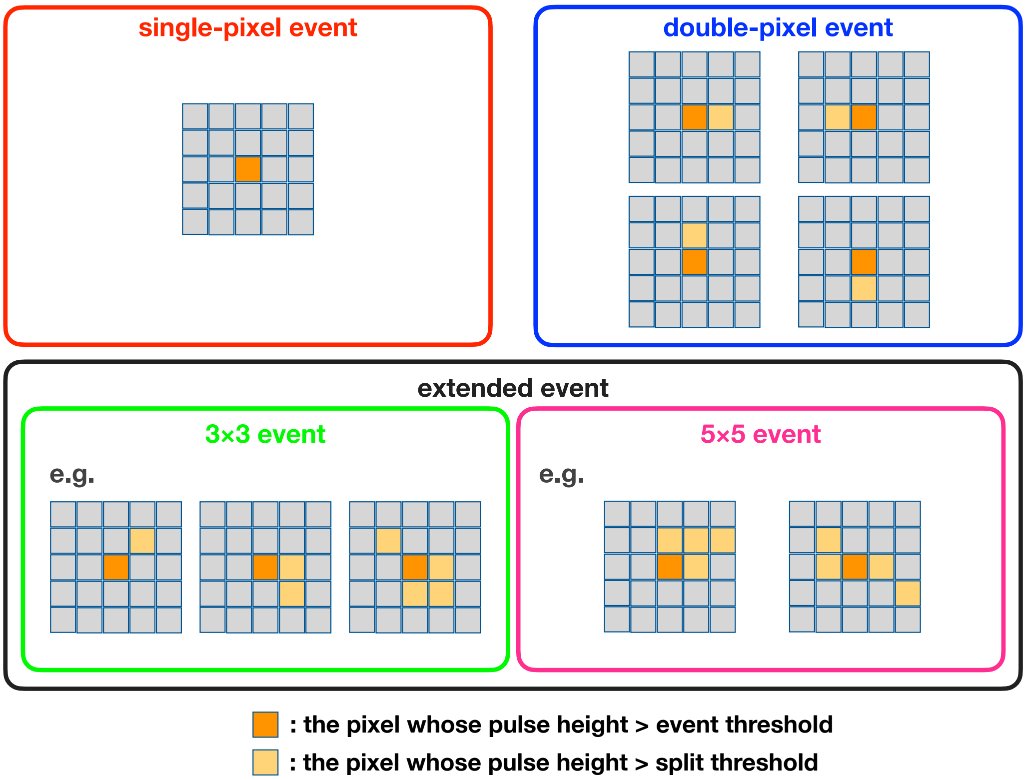

Figure 3.13: Event type categories in our algorithm. We detected and classified X-ray events based on the event threshold and split threshold, respectively (the pulse heights of the bad pixels are fixed to 0).

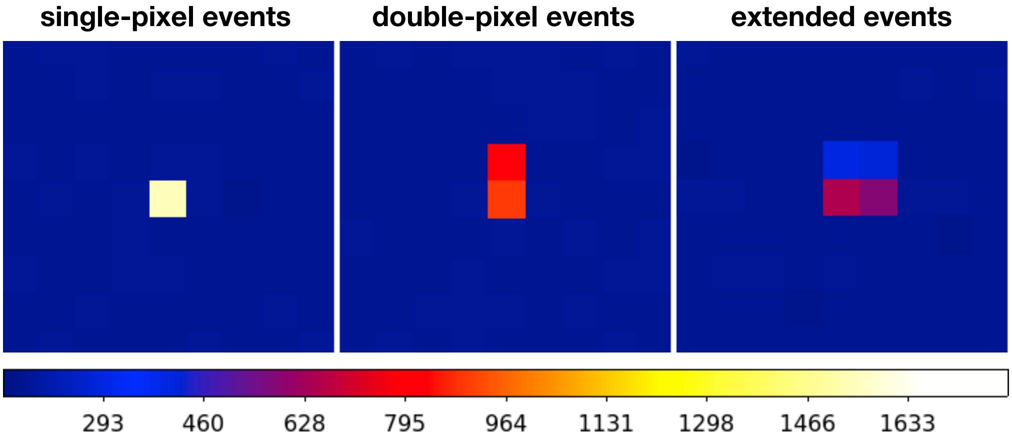

Figure 3.14: Image of a (left) single-pixel event, (center) double-pixel event and (right) extended event in the raw frame (adapted from Fig. 2 in Asakura et al. 2019[102]). For each event, the total pulse heights of neighboring pixels represent the energy of an incident X-ray photon.

Figure 3.15 shows an X-ray spectrum for each event type, obtained with ^{55}Fe at room temperature and the atmospheric condition. All X-ray spectra have a photopeak at the almost same pulse height of ~ 1400 ch, which shows that our event selection algorithm properly measures the incident X-ray energy. The energy resolution of GMAX0505 derived from the spectrum with single-pixel events is 176 eV (FWHM) at 5.9 keV even without cooling systems (the detailed analyses were summarized in Asakura et al 2019[102]). It indicates that GMAX0505 has the superior performance than that of GSENSE5130 in terms of the spatial and energy resolution. Hence, the adoption of this sensor would provide the self-images with higher sharpness (i.e., higher angular resolution). In the following sections, we report the proof-of-concept experiments with the new CMOS sensor with fine-pitch slits in section 4 and with coded apertures in section 5.

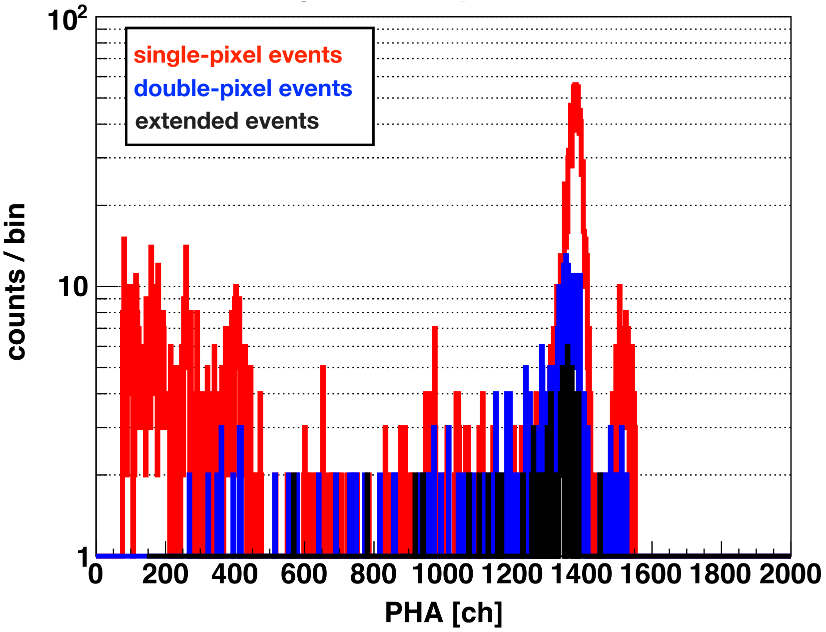

Figure 3.15: X-ray spectra with (red) single-pixel events, (blue) double-pixel events and (black) extended events, obtained with GMAX0505 at room temperature and the atmospheric condition (the same as Fig. 3 in Asakura et al. 2019,[102] but with different event and split thresholds). Photopeaks of Mn Kα and Kβ lines are clearly seen in the spectra.

Chapter 4

Proof-of-concept Experiments with Fine-pitch Slits

As mentioned in the previous section, whereas the prototype of MIXIM could not perform its potential angular resolution due to the lack of the spatial resolution of the adopted sensor, the renewed system of MIXIM with a new sensor with a high spatial resolution would overcome the performance limit. Hence, we re-evaluated the performance of one-dimensional (1D) imaging with this renewed system in 2018, then performed the demonstration of two-dimensional (2D) imaging for the first time for MIXIM in 2019. In this section, we report the detailed procedures and results of these experiments (see also Asakura et al. 2020,[103] 2023a[91]).

4.1 Setups

The proof-of-concept experiments in the following sections were performed in the beamline BL20B2 in SPring-8, of which schematic view is illustrated in Fig. 4.1; the length from the initial beam spot to the end of the downstream hutch is 215 m. As the beam spot size is 0.29 mm (H) and 0.06 mm (V), the beam divergence can be derived to be $0.28''$ (H) and $0.06''$ (V). Since the X-ray beam at BL20B2 has also high intensity, an attenuation plate was inserted so that we could run the sensor in a photon-counting mode. The X-ray beam was monochromatized with a double crystal monochromator upstream of the experiment hutches, and the beam size was set to be 10 mm × 10 mm, within the size of the imaging area of GMAX0505.

The experiment system was mainly comprised of two modules: a slit module and a sensor module. Figure 4.2 shows the actual experimental setup in the downstream and upstream hutches. Optical rails parallel to the beam axis were set in the both hutches, and a slit module and a sensor module were installed on the rail so that the beam could hit both the slits and sensor. Therefore the distance between these modules could be easily adjusted by moving them along the rails. While the slit module was basically fixed to the downstream hutch, it was moved to the upstream hutch in the case we elongated the slit-sensor distance beyond the length of the downstream rail.

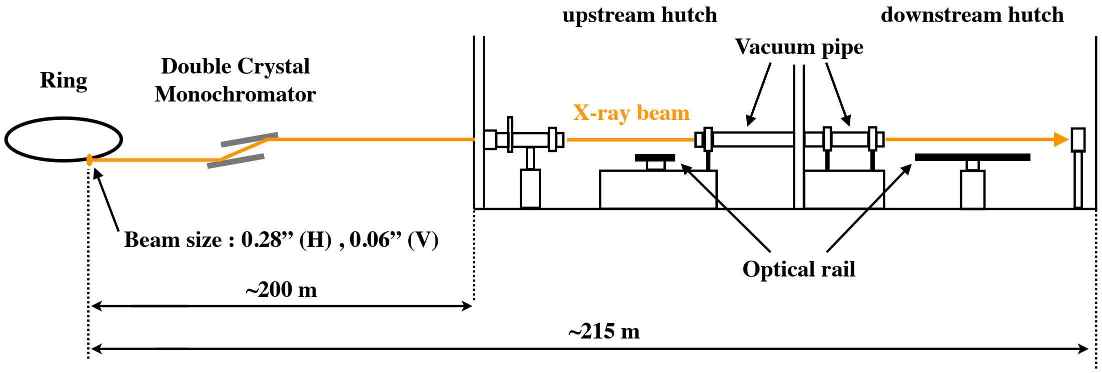

Figure 4.1: Schematic overview of SPring-8 BL20B2 (adapted from Fig. 6 in Asakura et al. 2023a[91]). The length of the beamline is ∼ 200 m, which provides us an X-ray beam with a high degree of parallelization. The X-ray beam passes through vacuum pipes to avoid attenuation due to air absorption.

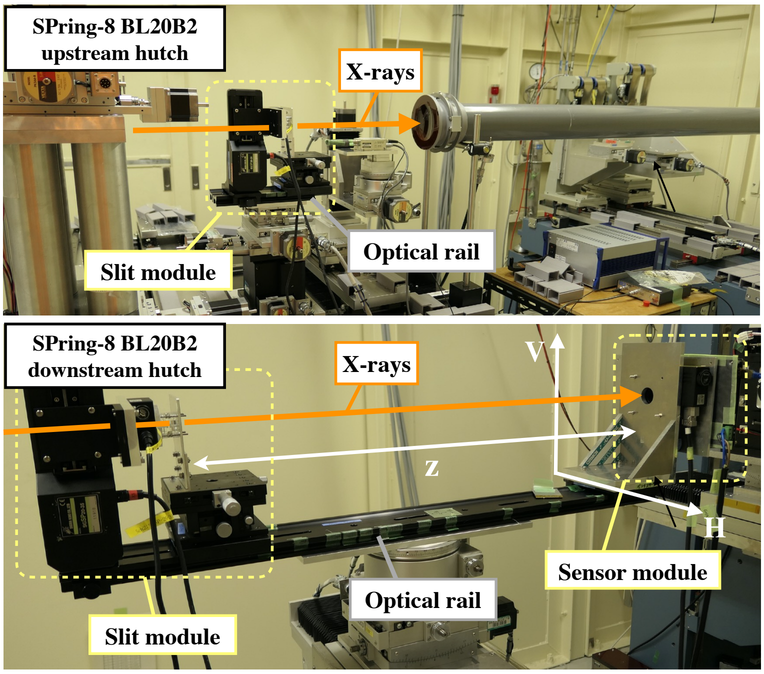

Figure 4.2: Actual setups in the upstream and downstream hutches during the experiment in 2019. The slit and sensor modules were movable to adjust the distance between them (n.b., the slit module was installed into either the upstream or downstream hutch while the sensor module was fixed into the downstream hutch).

GMAX0505, a sensor described in section 3.3, was installed to the sensor module with its evaluation board. It could be rotated in the H-V plane since the module had a rotation stage, which was required for the evaluation for the polarimetric performance (see section 6). As for the slit module, we adopted an absorption grating with a pitch of 9.6 µm and an opening fraction of 0.18 as multiple slits, which was manufactured by the LIGA (the german acronym for lithography, electroplating and molding) process at Karlsruhe Institute of Technology. The right panel of Fig. 4.3 shows a micrograph of the grating, from which we see the vertical slit structure with a pitch of 9.6 µm. Notably, the gold absorbers also have grooves, which are necessary for structural support. In the case of 2D imaging, we prepared two identical gratings with a pitch of 9.6 µm, and assembled a periodic pinhole mask by combining them so that their slit directions intersected perpendicularly.

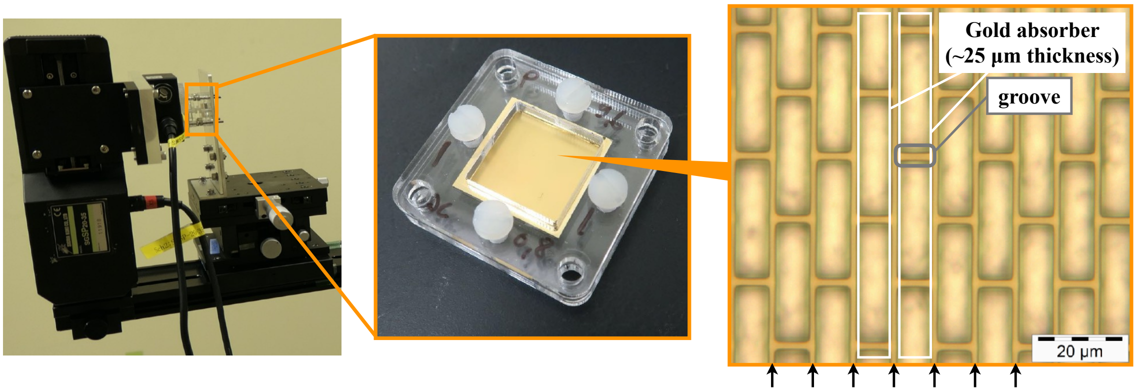

Figure 4.3: Image of the grating with a pitch of 9.6 µm and its micrograph, from which we see the vertical slit structure (denoted with black arrows). We also confirm that gold absorbers have grooves for structural support.

4.2 Analysis Procedures

First we irradiated an X-ray beam to the imaging system and extracted X-ray events in the same way described in section 3.3. As an example, Fig. 4.4 shows the X-ray spectrum for each event type derived from the frame data with the irradiation of 12.4 keV X-rays. The intense peak seen at ~ 2850 ch corresponds to 12.4 keV, which was ascribed to the primary X-ray beam. Besides, the spectra also have X-ray events which did not originate from the primary beam (e.g., low energy events due to background and fluorescent X-rays). Since these events unrelated to the primary X-rays could blur self-images, we basically extracted only X-ray events within an energy band of 3% centered on the target energy.

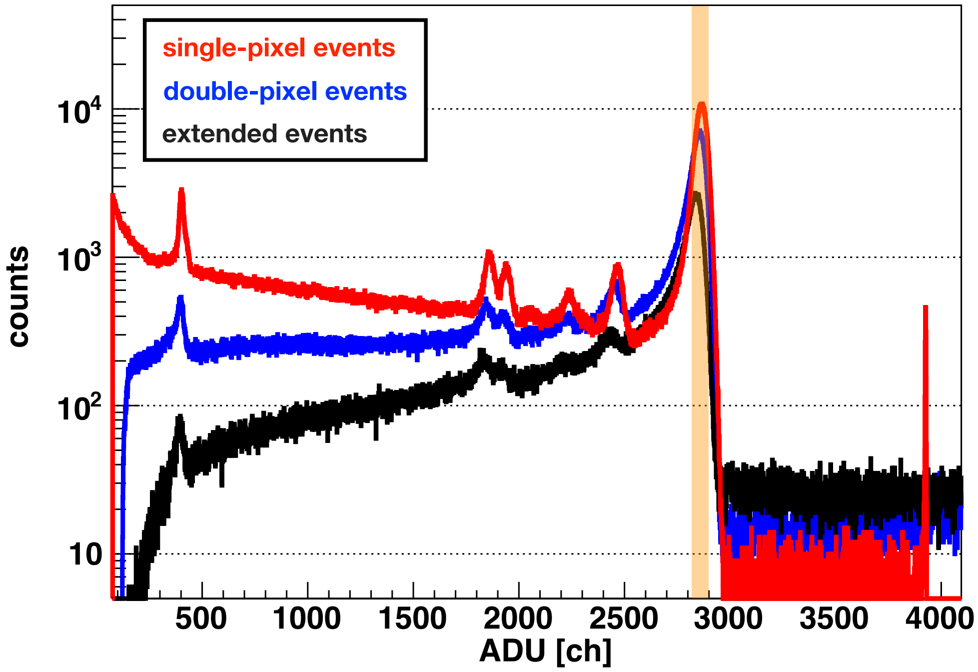

Figure 4.4: X-ray spectra with (red) single-pixel events, (blue) double-pixel events and (black) extended events, derived with GMAX0505. Besides the photopeak of the incident X-ray beam, some fluorescent lines appear in the spectra. X-ray events with higher energy than the beam energy are mainly due to high-order components of the X-ray beam.

Figure 4.5 and 4.6 show schematic charts of the analysis procedures of the 1D and 2D imaging, respectively. First we generated a photon count map with extracted X-ray events. In the case of the 1D imaging, the count map was projected along the slit direction, then it was folded along the axis shifting a folding period. For each folding period, we fitted the folded profile with a constant model (with a value of the average counts per bin) and derived a chi-square value, assuming that it reached the maximum when the folding period was perfectly consistent with the periodicity of the self-images while we obtained an acceptable fit when the folded profile was nearly flat. The procedures of the 2D imaging were almost the same as those of the 1D imaging, while the count map was folded two-dimensionally without projection. Hereafter, we define the folding period with the maximum chi-square value as the best-estimate period, and refer to the 1D and 2D profiles folded with the best-estimate period as the folded curve and folded map, respectively (n.b., folded curves and maps in the following sections are basically depicted so that the maximum bin is centered).

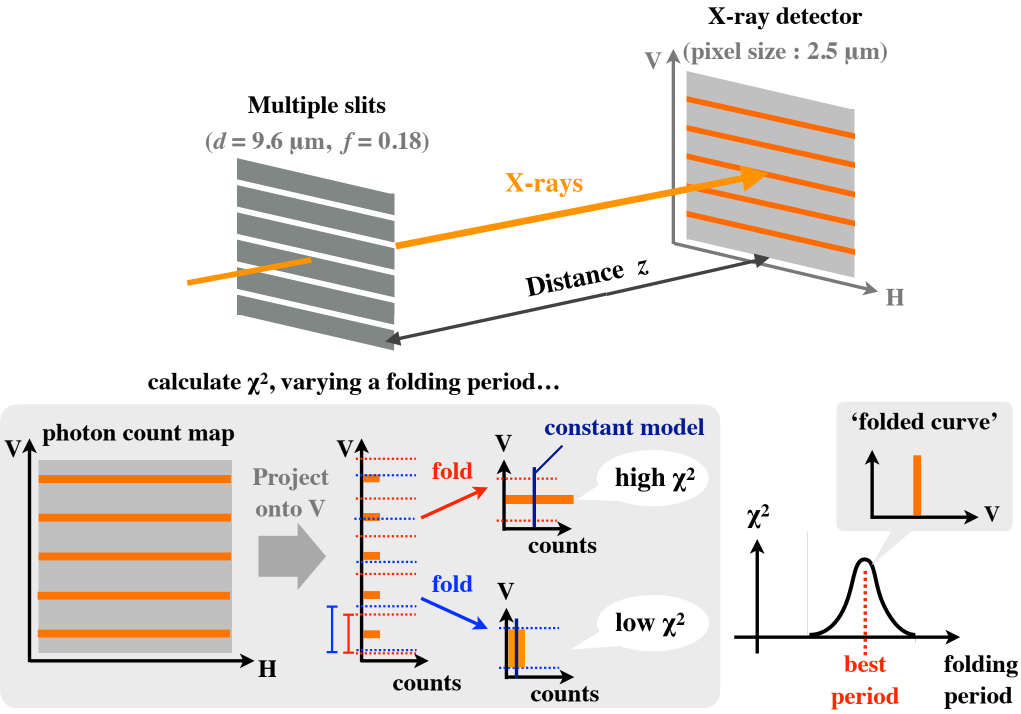

Figure 4.5: Schematic chart of the analysis procedures of the 1D imaging (Fig. 7 in Asakura et al. 2023a[91]).

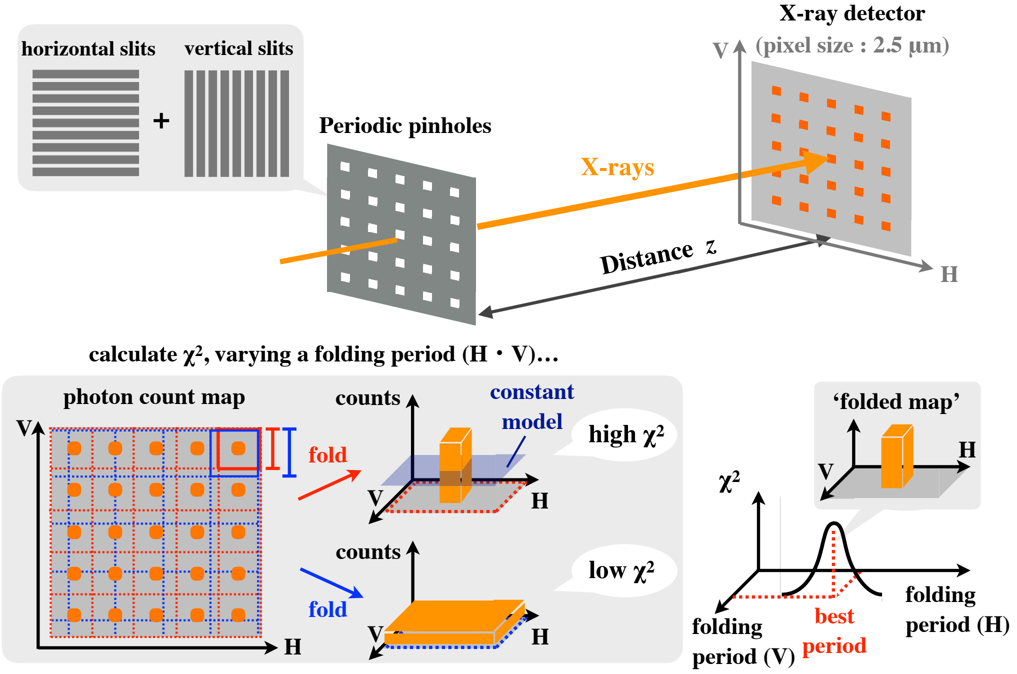

Figure 4.6: Schematic chart of the analysis procedures of the 2D imaging (Fig. 8 in Asakura et al. 2023a[91]).

In order to enhance the spatial resolution of the detector, we applied a sub-pixel analysis technique before creating the photon count map. Our sub-pixel analysis employed only single-pixel and double-pixel events (i.e., discarded extended events), and defined an incident area for each event type as shown in Fig. 4.7, assuming that single-pixel and double-pixel events are located in the center and the boundary area of a pixel, respectively.[104] The parameters for defining these areas, r_{S} and r_{D}, were determined so that the area ratio of these event types equals their counting ratio. Since accurate incident position cannot be identified by this technique, the sub-pixel incident coordinates of each event were randomly determined within the area for its event type. Although these areas have energy dependence, r_{S} and r_{D} were derived to be approximately 0.8 and 0.2 pixel at 12.4 keV in our experiments. Therefore, our detector has a spatial resolution of $\sim 2\,\mu\mathrm{m}$ for single-pixel events and $\sim 0.5\,\mu\mathrm{m}$ for double-pixel events, respectively.

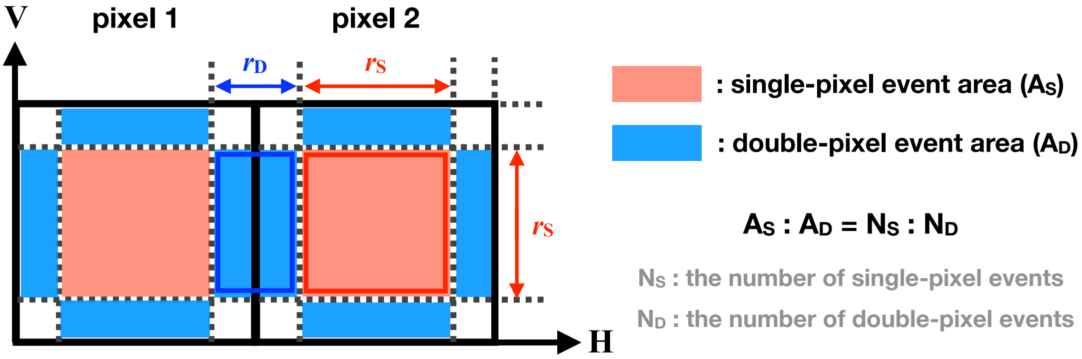

Figure 4.7: Definition of the single-pixel and double-pixel event areas in our sub-pixel analysis technique (Fig. 9 in Asakura et al. 2023a[91]). r_{S} and r_{D} are derived from the counting ratio of the single-pixel and double-pixel events.

4.3 Demonstration of 1D Imaging

4.3.1 Folded Curve

We took frame data at 12.4 keV and derived the folded curves with three types of configuration in 2018: $z = 92\,\mathrm{cm}$ ($m = 1$), $z = 184\,\mathrm{cm}$ ($m = 2$) and $z = 368\,\mathrm{cm}$ ($m = 4$). Figure 4.8 displays the 50-bin folded curves at these distances, normalized by the average counts per bin. Since a folding period corresponds a field of view (FOV), the horizontal axes of the folded curves are converted into incident angles; the FOVs of these configurations are $2.16''$, $1.08''$ and $0.54''$ at $z = 92\,\mathrm{cm}$, $z = 184\,\mathrm{cm}$ and $z = 368\,\mathrm{cm}$, respectively. Although the folded curves should ideally become square shapes, they are smoothed due to some reasons: e.g., the beam divergence, fabrication accuracy of the slit structure, and the limited spatial resolution of the detector.

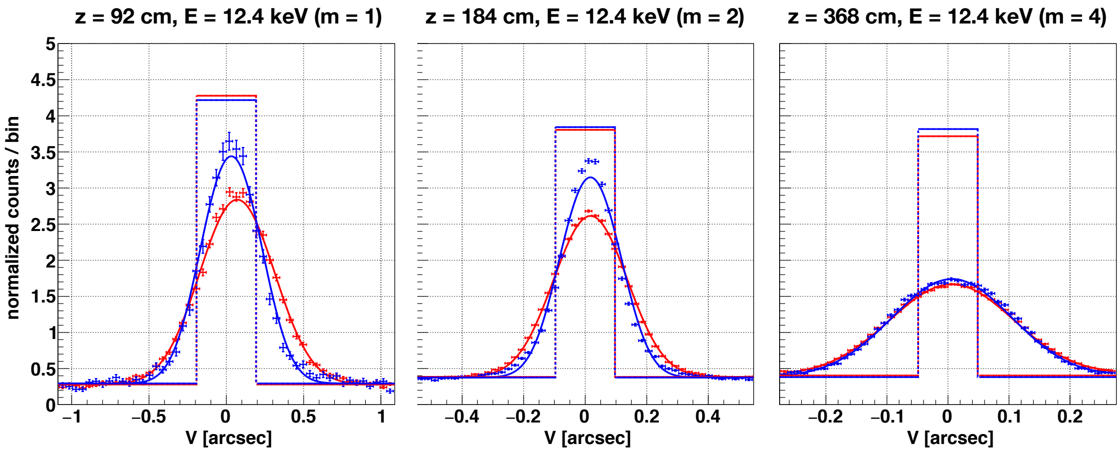

Figure 4.8: Folded curves at $z = 92\,\mathrm{cm}$, $z = 184\,\mathrm{cm}$ and $z = 368\,\mathrm{cm}$, where the horizontal and vertical axes show incident angles and normalized counts per bin (Fig. 10 in Asakura et al. 2023a[91]). The color indicates the event type used in the analyses (red: single-pixel events, blue: double-pixel events). The dotted and solid lines are the best-fit square models before and after Gaussian smoothing respectively.

We also irradiated X-rays with a variety of energy (ranging from 6 keV to 15 keV) at $z = 92\,\mathrm{cm}$ to investigate the energy dependence. Figure 4.9 shows folded curves at several kinds of incident energy, which indicates that the self-images are gradually blurred as m departs from integers. Notably, the folded curve at 14.8 keV have an almost flat profile, which endorses that a diffraction cannot be ignored in this configuration and the obtained self-images are surely ascribed to the Talbot effect. Since the shift of X-ray energy (see Eq. 3.1) is equivalent to the shift of the slit-sensor distance, this result also implies the tolerance level of slit-sensor distance accuracy.

4.3.2 Model Fitting

In order to evaluate the specific imaging performance, we fitted the folded curves with a smoothed square model: the convolution of a square shape plus a constant and a normalized Gaussian. The square width and normalization of the entire model were fixed to be the slit width and total counts respectively, while the square center, the ratio of the constant to the entire model and the standard deviation of the Gaussian were set to

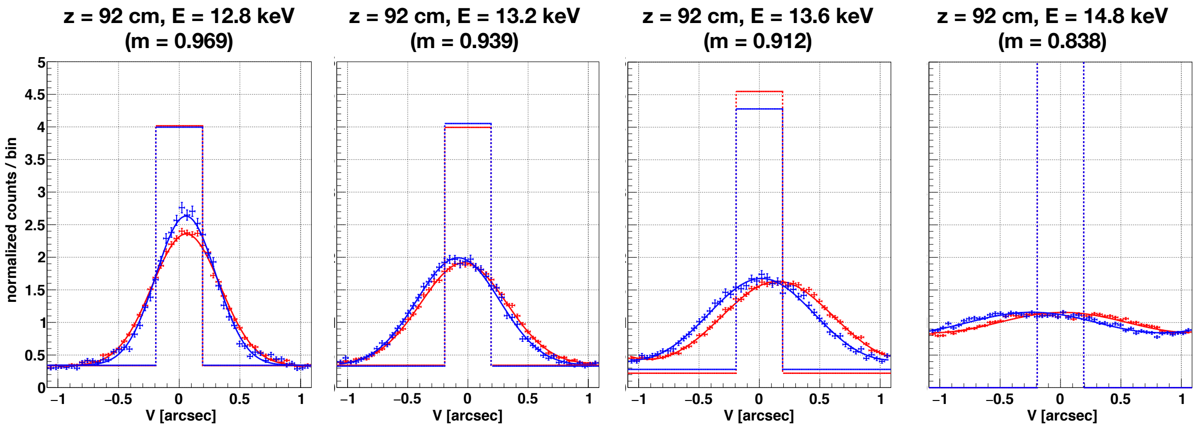

Figure 4.9: From the left panel, the folded curve with incident X-ray energy of 12.8 keV, 13.2 keV, 13.6 keV and 14.8 keV obtained with the same configuration as Fig. 4.8 (red: single-pixel events, blue: double-pixel events). As the X-ray energy shifts from 12.4 keV ($m = 1$), the visibility gradually decreases due to blurring.

be free. From the fitting results, we derive the FWHM and visibility $\mathcal{V}$ as the measures of actual angular resolution and constant contribution. In this paper, the FWHM was calculated excluding the constant, and $\mathcal{V}$ was defined as the following equation:

$$\mathcal{V} = \frac{C_{\max} - C_{\min}}{C_{\max} + C_{\min}}, \tag{4.1}$$

where $C_{\max}$ and $C_{\min}$ are the maximum and minimum counts per bin of the best-fit model. FWHM and $\mathcal{V}$ derived from the best-fit parameters are summarized in table 4.1, and the best-fit square models before and after smoothing are over-plotted as dotted and solid lines, respectively, in Fig. 4.8 and 4.9.

We note that the folded curve at $z = 368$ cm is more blurred than that at $z = 92$ cm, though the incident X-rays were almost monochromatized; the main reason is that the parallel beam approximation used for deriving z gets worse as z increases. Regarding the beam with a divergence as a spherical wave, Eq. 3.1 can be replaced by the following equation:

$$z_{\mathrm{T}} = m\frac{d^2}{\lambda}\frac{z_0}{z_0 - \frac{md^2}{\lambda}} (m = 1, 2, 3...), \tag{4.2}$$

where z_0 represents the distance between the X-ray source and slits.[105] It means that the optimal distance z with a spherical wave becomes larger than that derived with the Eq. 3.1. Although this effect deteriorated the self-imaging in this experiment, even the folded curve at $z = 368$ cm retains the visibility of more than 0.5. Consequently, these results show that MIXIM has an angular resolution as high as that of *Chandra* even though the size of the system is less than 1 m, and can realize higher angular resolution than that of *Chandra* by the elongation of the distance z.

Table 4.1: Summary of the 1D fitting results. Ideal values are derived with Eq. 3.2.

Configuration					Performance index	
z (cm)	E (keV)	m	event type	ideal value	$\mathcal{V}$	FWHM (arcsec)
92	12.4	1	single-pixel	$0.39''$	$0.829^{+0.004}_{-0.004}$	$0.531^{+0.010}_{-0.009}$
			double-pixel		$0.842^{+0.006}_{-0.006}$	$0.450^{+0.011}_{-0.011}$
	12.8	0.969	single-pixel		$0.749^{+0.003}_{-0.003}$	$0.665^{+0.007}_{-0.007}$
			double-pixel		$0.771^{+0.005}_{-0.005}$	$0.583^{+0.009}_{-0.009}$
	13.2	0.939	single-pixel		$0.673^{+0.004}_{-0.004}$	$0.846^{+0.011}_{-0.011}$
			double-pixel		$0.699^{+0.006}_{-0.006}$	$0.813^{+0.015}_{-0.014}$
	13.6	0.912	single-pixel		$0.580^{+0.005}_{-0.005}$	$1.110^{+0.038}_{-0.034}$
			double-pixel		$0.598^{+0.008}_{-0.008}$	$1.036^{+0.039}_{-0.035}$
184	12.4	2	single-pixel	$0.19''$	$0.740^{+0.002}_{-0.002}$	$0.286^{+0.003}_{-0.002}$
			double-pixel		$0.750^{+0.004}_{-0.004}$	$0.287^{+0.004}_{-0.004}$
368	12.4	4	single-pixel	$0.097''$	$0.564^{+0.004}_{-0.004}$	$0.264^{+0.006}_{-0.006}$
			double-pixel		$0.589^{+0.007}_{-0.007}$	$0.258^{+0.009}_{-0.008}$

Figure 4.10 and 4.11 show the energy dependence of the FWHM and $\mathcal{V}$, respectively. Figure 4.10 demonstrates that the visibility has peaks around 12.4 keV ($m = 1$) and 6.2 keV ($m = 2$), and maintains more than 0.5 within the energy band of $\pm(10/m)\%$ at these peaks. The energy band extension is actually a trade-off with the imaging performance since it leads to the deterioration of not only the visibility but also the angular resolution as shown in Fig. 4.11, yet the wide energy band can work as a great advantage for actual observation considering the low photon flux from astrophysical X-ray sources.

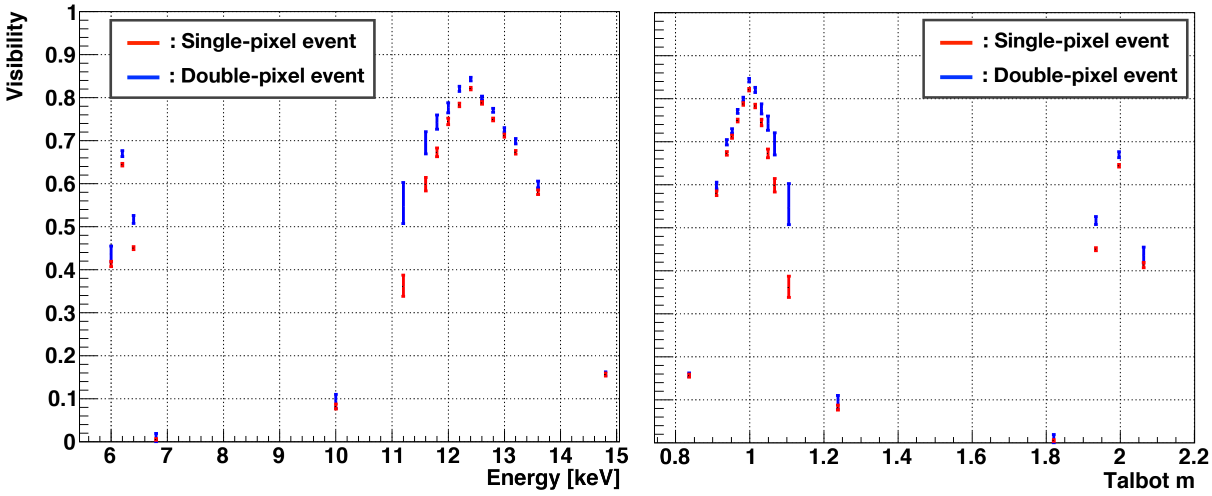

Figure 4.10: (Left) Energy dependence of the visibility with $z = 92\,\mathrm{cm}$ and $d = 9.6\,\mu\mathrm{m}$ (Fig. 11 in Asakura et al. 2023a[91]). The visibility has more than 0.5 within an energy band of ±$(10/m)$%. (Right) Same as the left panel, but the horizontal axis is transformed from an X-ray energy to m.

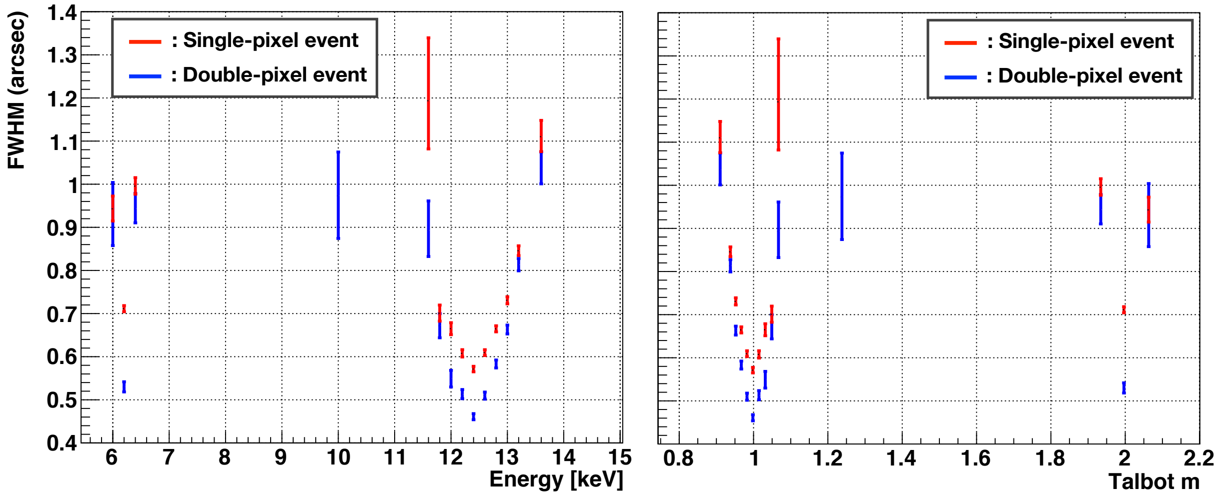

Figure 4.11: (Left) Energy dependence of the FWHM with $z = 92\,\mathrm{cm}$ and $d = 9.6\,\mu\mathrm{m}$. (Right) Same as the left panel, but the horizontal axis is transformed from an X-ray energy to m.

4.4 Demonstration of 2D Imaging

4.4.1 Folded Map

As for the 2D-imaging, we first adjusted the mask-sensor distance z to 92 cm, and irradiated a 12.4 keV X-ray beam. Figure 4.12 represents the folded maps at $z = 92$ cm (binned with 50 × 50 pixels), with single-pixel and double-pixel events. In this case, the FOV is derived to be $2.16'' \times 2.16''$. Both folded maps clearly demonstrate that we succeeded in obtaining the 2D profile of the X-ray beam. In particular, the folded map with the double-pixel events significantly extends along the horizontal axis, which gives a hint of the intrinsic beam divergence. Afterwards, we also took data at $z = 92$ cm with varying the incident X-ray energy as with the case of the 1D-imaging, and confirmed the similar energy dependency to the result of the 1D-imaging.

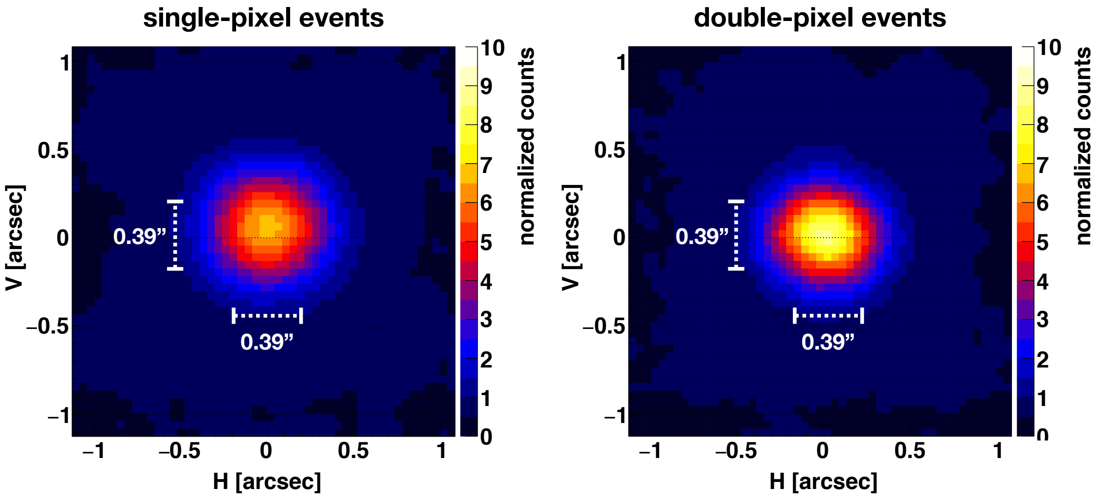

Figure 4.12: Folded maps at $z = 92$ cm with (left) single-pixel events and (right) double-pixel events, smoothed with a Gaussian filter for better visualization (Fig. 12 in Asakura et al. 2023a[91]). The color bar represents the normalized counts and the dotted white lines show the expected performance derived with Eq. 3.2.

Then we extended the distance z from 92 cm ($m = 1$) to 866.5 cm ($m = 9$), the maximum distance achievable in the experiment hutches, in order to enhance the angular resolution. This distance was derived with Eq. 4.2 taking into account the effect of the beam divergence. Combining both single-pixel and double-pixel events, we obtained the folded map (binned with 50 × 50 pixels) as shown in Fig. 4.13. The intrinsic beam profile can be successfully resolved, since the elongation of the distance z corresponds to zooming-in, which provides us high angular resolution in return for a narrow FOV. Notably, the horizontal beam divergence ($0.28''$) is more extended than the FOV at $z = 866.5\,\mathrm{cm}$ ($0.24''$). In this case, the outskirt of the image which protrudes from the one side of the FOV contaminates the other side, because of the folding analysis procedure (hereafter we refer to it as the wrap-around effect).

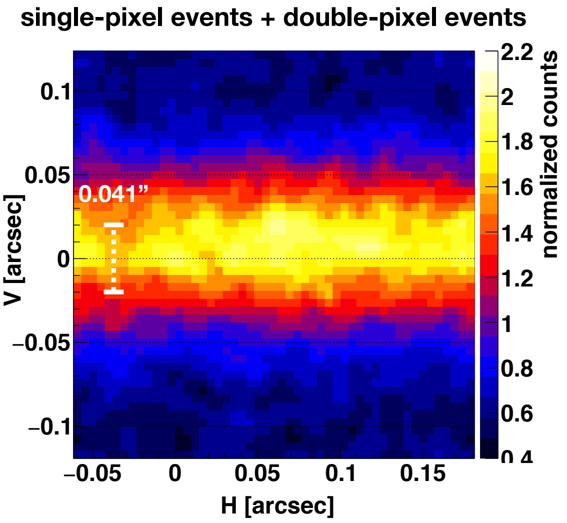

Figure 4.13: Same as Fig. 4.12, but it was obtained at $z = 866.5\,\mathrm{cm}$ with both single-pixel events and double-pixel events (Fig. 13 in Asakura et al. 2023a[91]).

4.4.2 Model Fitting

To evaluate the specific performance, we extended the 1D smoothed square model used in section 4.3 to 2D: the convolution of a square box plus a constant plane with a normalized 2D Gaussian. The horizontal and vertical standard deviations of the 2D Gaussian and the ratio of the constant plane were set to be free, whereas the other parameters were fixed in the same way as the 1D model fitting. The wrap-around effect seen at $z = 866.5\,\mathrm{cm}$ was taken into account in the 2D model. The horizontal and vertical FWHM and visibility derived from the model fitting are summarized in table 4.2. We obtained the horizontal and vertical FWHM to be $0.51''$ and $0.48''$ at $z = 92\,\mathrm{cm}$, which agrees with the result of the 1D imaging. Besides, the folded map at $z = 866.5\,\mathrm{cm}$ has the vertical FWHM of less than $0.1''$, while the horizontal FWHM cannot be available due to the almost flat profile. Notably, the derived FWHM includes the intrinsic beam divergence of $0.06''$, which causes the overestimate of the angular resolution. Subtracting the beam divergence, the angular resolution at this configuration is estimated to be $0.054''$.

Table 4.2: Summary of the 2D fitting results.

Configuration				Performance index	
z (cm)	E (keV)	m	event type	$\mathcal{V}$	H-FWHM / V-FWHM (arcsec)
92	12.4	1	single-pixel	$0.860^{+0.002}_{-0.002}$	$0.560^{+0.002}_{-0.002}$ / $0.546^{+0.001}_{-0.003}$
			double-pixel	$0.885^{+0.002}_{-0.002}$	$0.506^{+0.002}_{-0.002}$ / $0.476^{+0.003}_{-0.002}$
866.5	12.4	9	single+double	$0.522^{+0.011}_{-0.011}$	N/A / $0.081^{+0.001}_{-0.002}$

4.4.3 Separation of Two Point-sources

Finally, we simulated the observation of two point-sources sub-arcseconds apart from each other; we rotated the imaging system in azimuth direction in steps of $0.09''$ centered on the beam axis, extracted X-ray events for each rotation angle, and merged X-ray events obtained with on-axis configuration and slightly rotated off-axis configuration (as shown in 4.14). Analysis procedures after creating a photon count map are the same as that we explained in section 4.2, while horizontal and vertical folding periods were fixed to the best-estimate values derived from non-merged on-axis data.

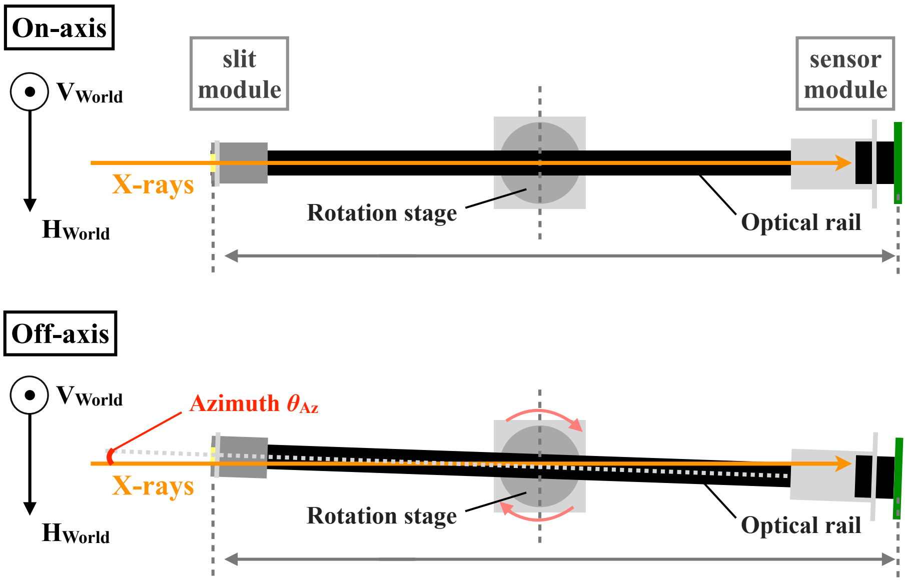

Figure 4.14: Illustration of the on-axis and off-axis configuration. We rotated the imaging system in steps of $0.09''$ using a rotation stage.

Figure 4.15 shows the folded maps with two point-sources for each elongation, from $0.09''$ to $0.81''$. It clearly demonstrates that MIXIM succeeded in resolving the two point-sources $0.5''$ apart from each other, and simultaneously verifies that imaging performance is almost unchanged for even off-axis angles. Notably, MIXIM at $z = 92\,\mathrm{cm}$ should resolve smaller elongation than $0.54''$ in the case of ideal two point-sources, since the beam profile intrinsically has a divergence of $0.28''$ in the horizontal direction.

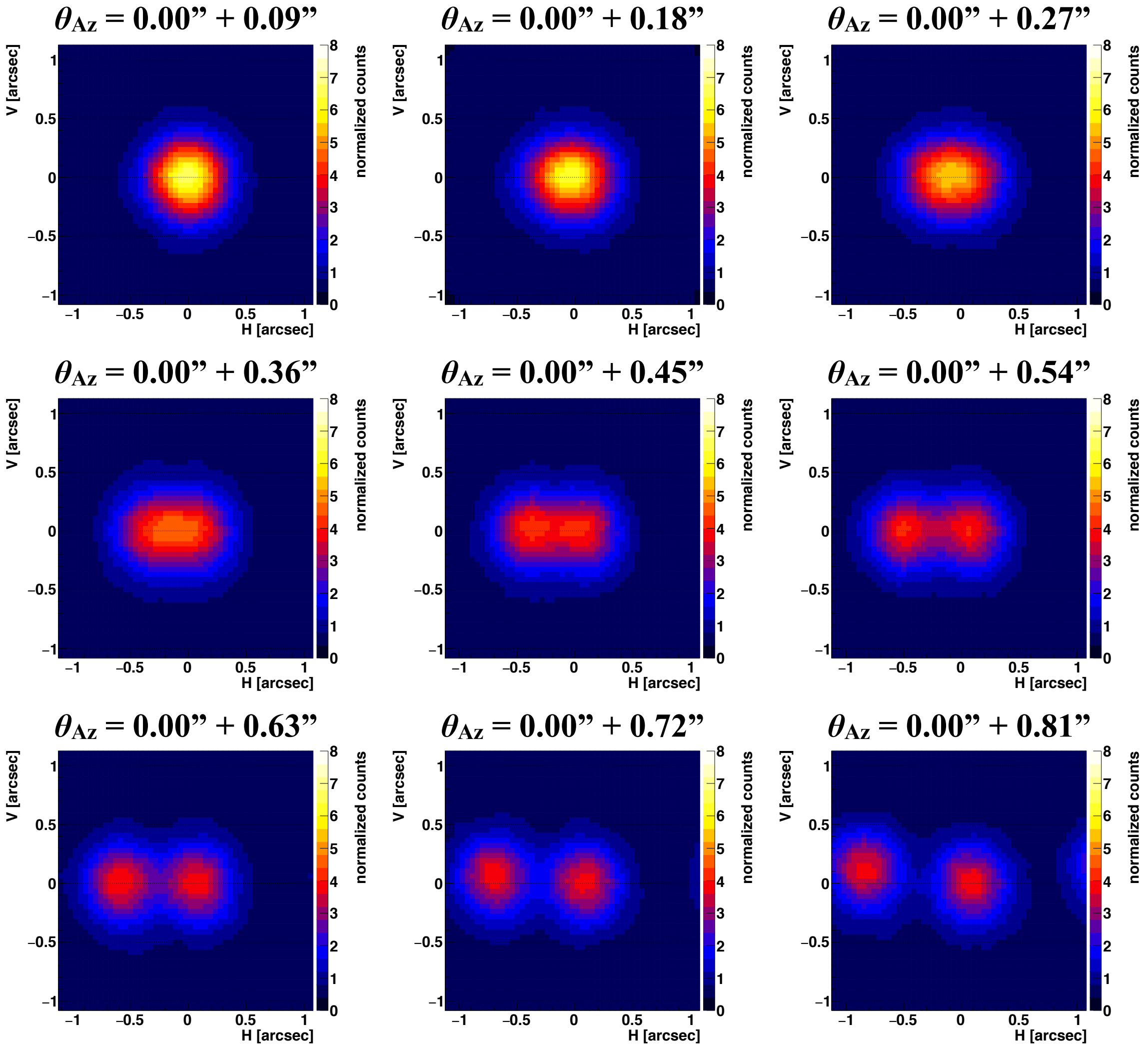

Figure 4.15: Results of two point-sources observation, resulting from the combination of the on-axis and off-axis data. We can distinguish two point-sources at least where $\theta_{\mathrm{Az}} \geq 0.54''$, which supports MIXIM has an angular resolution of $0.5''$ even with a system size of $92\,\mathrm{cm}$.

Chapter 5

Experiments with Multiple Coded Aperture Masks

In the previous chapter, we achieved high-resolution X-ray imaging with a multi-pinhole mask. However, MIXIM still has some issues for practical observation; one of them is the low effective area, mainly ascribed to the opening fraction. The opening fraction and transmittance of the multi-pinhole mask used in 2019 were only 3.2% and 1.3% at 12.4 keV, respectively. It means that the great majority of incident X-rays were absorbed by the multi-pinhole mask and cannot contribute X-ray imaging. Hence, we introduced a novel method for improving the effective area of MIXIM, and conducted proof-of-concept experiments with a new method in February and July 2020 (see also Asakura et al. 2022[106]).

5.1 Multiple Coded Aperture Masks

As mentioned in section 2.1, a random hole mask or a coded aperture mask were employed in a variety of X-ray and Gamma-ray observatories so far, instead of a simple pinhole mask with a low opening fraction. Whereas these masks cannot be applied as they are since MIXIM requires equally-spaced apertures for the Talbot effect, periodic arrangement of these masks is supposed to form self-images, because the Talbot effect occurs with arbitrary aperture patterns in principle. Therefore, we newly introduced multiple coded aperture (MCA) masks instead of the periodic pinhole mask. We note that opening fractions are comparable between MCA masks and conventional coded aperture masks. However, MCA masks can provide higher angular resolution circumventing a diffraction effect, while conventional coded aperture masks have much wider FOVs than that of a MCA mask. The angular resolution and opening fraction of a MCA mask can be determined by the aperture element size and aperture pattern. Employing an aperture element size of few µm and a pattern with an opening fraction of about 0.5, an effective area can be enhanced by one digit compared with the multiple pinhole mask used so far, maintaining high angular resolution.

Figure 5.1 shows a schematic view of the procedures with both a multiple pinhole mask and MCA mask. Although self-images obtained with a MCA mask are the convolution of an X-ray source profile and a coded aperture pattern as they are, the original source profile can be derived by a decoding process same as conventional coded aperture imaging (reviewed by e.g., Caroli 1987,[5] Cieslak 2016[107]). Notably, an aperture pattern is independent of imaging itself while it is related to a decoding process; a decrease of the aperture element size improves angular resolution for a certain mask pitch, though it also necessitates spatial resolution high enough to resolve the aperture pattern. While arbitrary aperture patterns can be utilized for self-imaging, a pattern whose autocorrelation has non-constant sidelobes yields systematic errors (often called artifacts). In our experiments, we adopted a modified uniformly redundant array (MURA)[108] as the aperture pattern of a MCA mask.

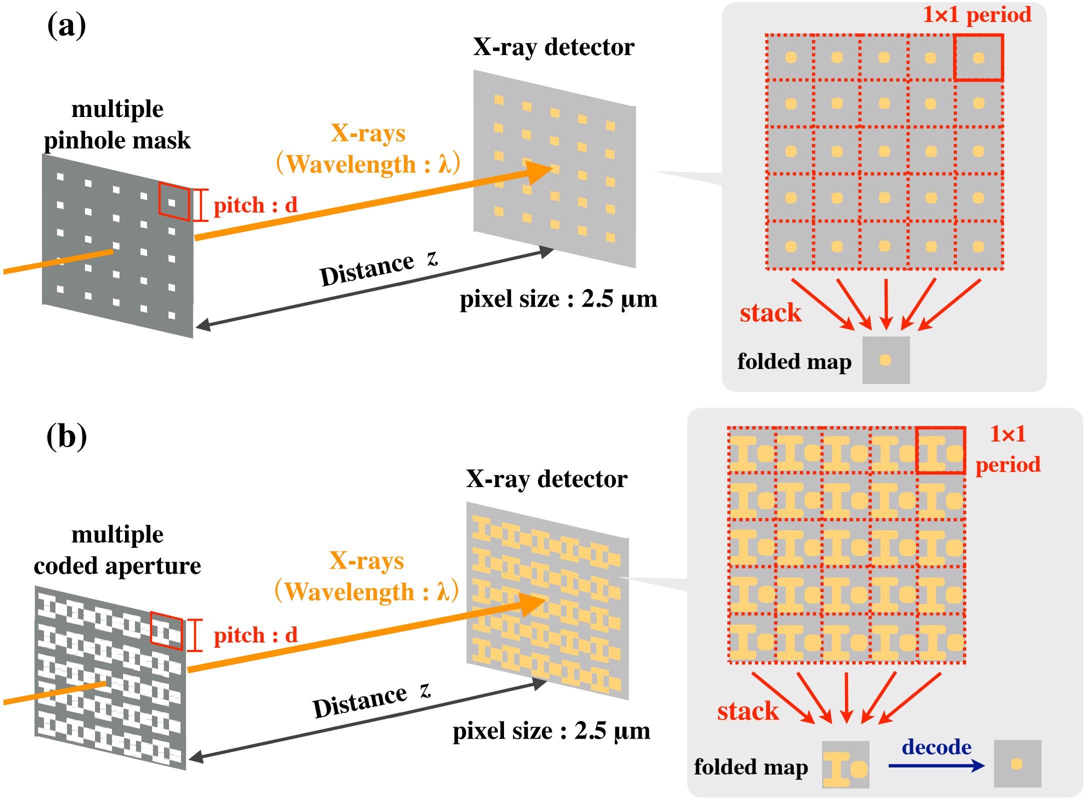

Figure 5.1: Schematic drawings of (a) the previous analysis chart with a multiple pinhole mask, and (b) newly proposed analysis chart with a MCA mask. The newly proposed one has a quite larger effective area thanks to its high opening fraction.

5.2 Components

In order to demonstrate the novel idea, we newly introduced three types of MCA masks which were fabricated by the LIGA process at Karlsruhe Institute of Technology (same as the gratings used so far). The masks consist of gold absorbers with a thickness of $> 20\,\mu\mathrm{m}$ and polyimide substrates with a thickness of $550\,\mu\mathrm{m}$ (including chromium and gold). Whereas all of them have the same size of $15\,\mathrm{mm} \times 15\,\mathrm{mm}$, their periodic absorber patterns are different for each type. Pattern A (5×5 MURA) and B (5×5 random pattern: for comparison with MURA) have pitches of $12.5\,\mu\mathrm{m}$, while pattern C ($11{\times}11$ MURA) has a pitch of $27.5\,\mu\mathrm{m}$. Figure 5.2 illustrates the original design of each mask pattern and micrographs after production. We note that the original design cannot be completely reproduced due to processing accuracy, and the transmittance of the opening area is not unity due to absorption by substrates. It implies that the original binary patterns cannot be applicable for a decoding process as they are. While we changed the multiple pinhole mask to the MCA mask, we adopted GMAX0505, the same sensor as that used in 2019. Even in the case of the MCA masks, both spatial resolution high enough to resolve the fine structure of the periodic patterns and spectral resolution high enough to extract only X-ray events within a target energy band are required to obtain the self-images without degradation. Therefore, GMAX0505 also played an important role as the detector of MIXIM, as with the previous experiments.

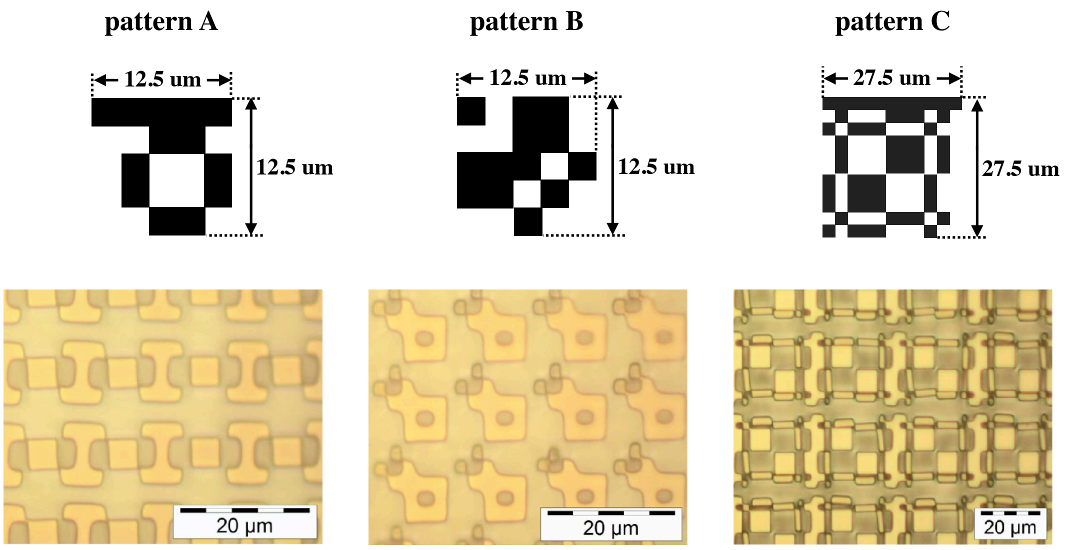

Figure 5.2: (Top) Original design of each mask pattern. Gold absorbers based on each pattern are arranged on the substrate. (Bottom) Micrographs of three types of MCA masks, fabricated by the LIGA process.

5.3 Setups

In order to evaluate the performance of the renewed system with the MCA masks, we conducted proof-of-concept experiments in February and July 2020 at BL20B2 in SPring-8. Figure 5.3 and 5.4 illustrate schematic overview and actual photos of the entire experimental system, respectively. As with the previous experiment, the beam was monochromatized by a double crystal monochromator installed upstream of the hutches, and attenuation plates were inserted on the beam axis to reduce the beam intensity since we run the sensor in a photon-counting mode. A mask module and sensor module were installed onto an optical rail so that the distance between them z can be adjusted. We set z to 157 cm and 786 cm when we used the mask with a pitch of 12.5 µm (pattern A and B) and 27.5 µm (pattern C), respectively, so that 12.4 keV X-rays satisfy Eq. 4.2 (corresponding to $m = 1$).

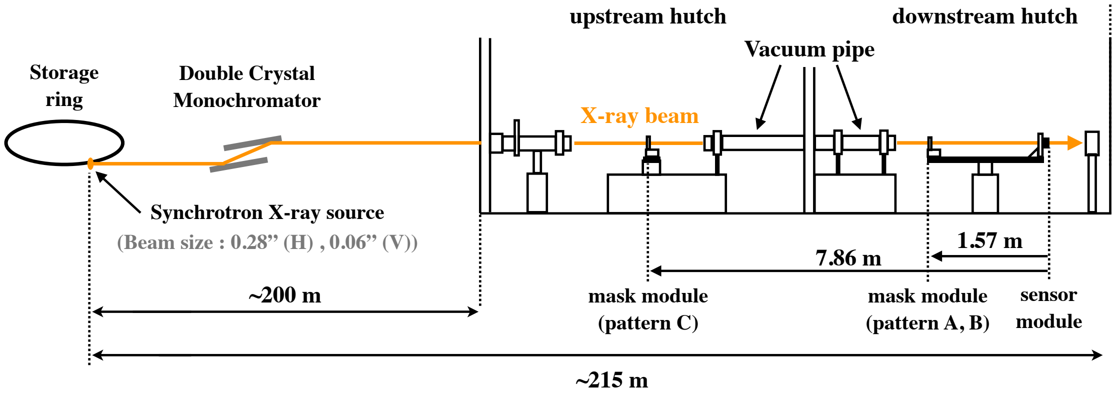

Figure 5.3: Overview of the entire experimental system. The monochromatized synchrotron X-ray beam is irradiated to the experimental hutches. Vacuum pipes are installed in the beam path to prevent air absorption.

5.4 Analysis Procedures

The analysis procedure in this experiment is basically the same as that explained in section 4.2 until creating a folded map. Since a folded map represents the convolution of an X-ray source profile and the transmittance pattern of a MCA mask, it has to be decoded to reconstruct the intrinsic X-ray source profile. This process requires the original transmittance pattern of each MCA mask for 12.4 keV X-ray irradiation, which differs from the original binary patterns as shown in section 5.2. Hence, we took raw

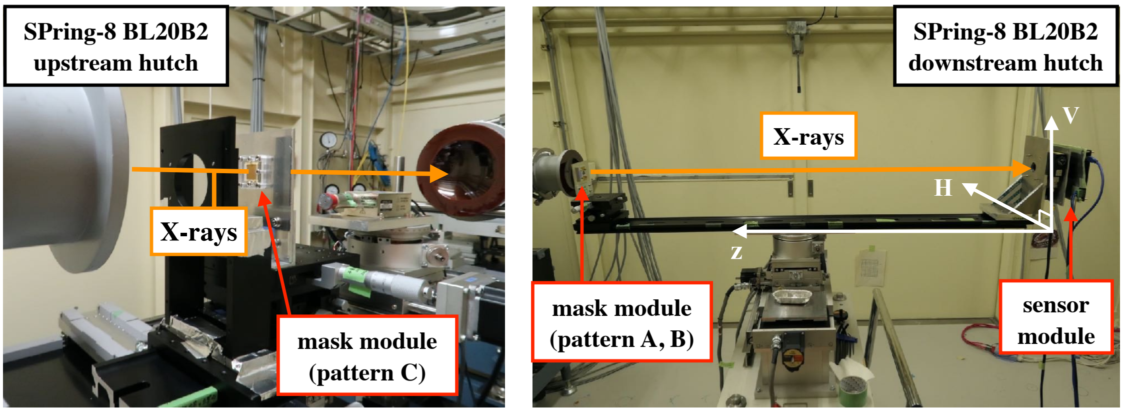

Figure 5.4: Photo of the experimental hutches where we assembled the imaging system. White arrows indicate the coordinate system in the experimental hutches.

frame data at $z = 1.58\,\mathrm{cm}$, i.e., getting the mask and detector as close as possible, and created a folded map for each MCA mask with the same procedure. With the folded maps at $z = 1.58\,\mathrm{cm}$ and X-ray flux measured without the MCA masks, we obtained the original 1×1 period transmittance patterns and employed them in a decoding process.

In this paper, we deciphered a folded map with a following procedure; assuming that a background component can be negligible, a response matrix W follows

$$\begin{cases} \tilde{D} & = W * \tilde{S}, \\ \tilde{D}(j) & = \sum_i W(i,j)\tilde{S}(j), \end{cases} \tag{5.1}$$

where $\tilde{S}$ and $\tilde{D}$ are matrices which represent a source profile and a profile on a detector, respectively. In our analysis, the response matrix W was calculated based on a simple geometry as depicted in Fig. 5.5; the transmittance pattern with grids of 500×500 obtained from the experiment was placed in the mask plane, and a source plane S and detector plane D were set to 50×50 grids (i.e., $i, j = 1, 2, ..., 2500$) same as a folded map. Regarding the i-th grid $S(i)$ as a departure point, we calculated the trajectory of an X-ray photon passing through each mask grid, filled the transmittance at the mask grid into a detector grid $D(j)$ where the X-ray arrives, and derived the average transmittance for each detector grid. Notably, if an X-ray photon protruded from the field of view such as the red arrow shown in Fig. 5.5, it was shifted by an integer multiple of the folding period to fit within the field of view, considering the folding procedure. Since the obtained pattern D corresponded the response vector for a particular $S(i)$, the aforementioned calculation was repeated for all $S(i)$, which yielded 2500 types of D in total. The response matrix W was finally obtained as a concatenation of each D.

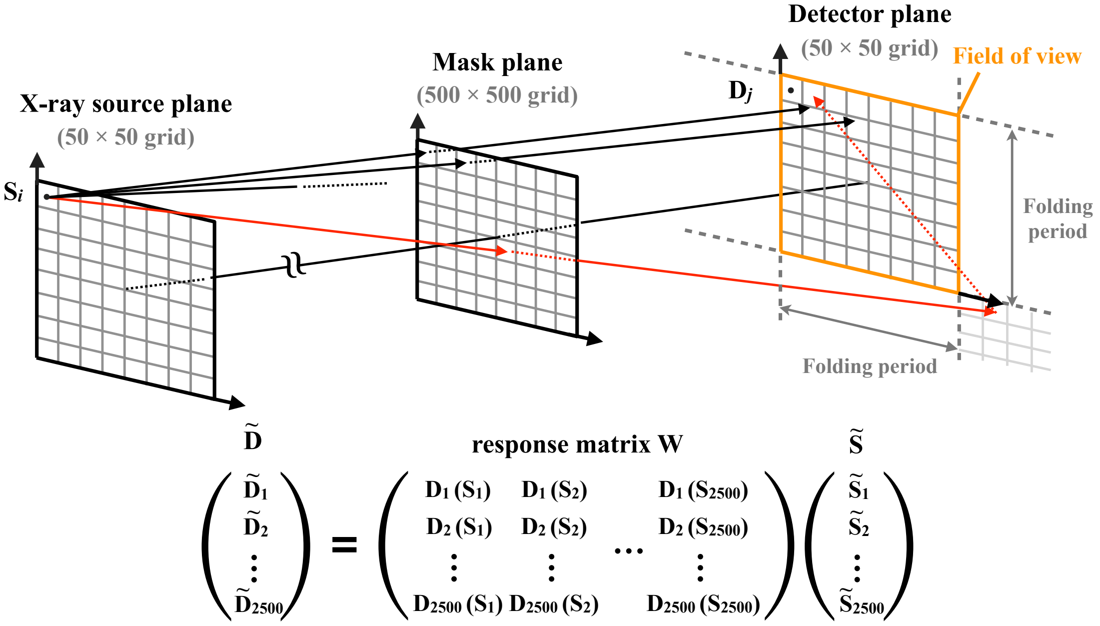

Figure 5.5: Overview of the geometry for deriving the response matrix. The red arrow represents the case that a photon protrudes from the field of view.

In order to reconstruct an X-ray source profile with the response matrix W, we adopted the Expectation-Maximization (EM) algorithm:[109] the algorithm for computing the maximum likelihood by repeating the Expectation-step (E-step) and Maximization-step (M-step) alternately. In our case, E-step and M-step can be described as

$$\begin{cases} \text{E-step: } \tilde{D}^{(n)}(j) & = \sum\limits_i W(i,j)\tilde{S}^{(n)}(i), \\ \text{M-step: } \tilde{S}^{(n+1)}(i) & = \tilde{S}^{(n)}(i) \sum\limits_j \dfrac{\delta(j)W(i,j)}{\tilde{D}^{(n)}(j)}, \end{cases} \tag{5.2}$$

where n and δ represents the iteration number and obtained folded map, respectively.[110] Since the likelihood never decreases at each iteration (see the appendix of Shepp 1982[110]), it converges to the maximum by the repetition of the E-step and M-step, which means that we can estimate the most probable source profile with this algorithm. In this paper, we employed the Kullback-Leibler (KL) divergence, defined by the following equation:

$$KL(D^{(n+1)}, D^{(n)}) = \sum_i D^{(n+1)}(j) \log \frac{D^{(n+1)}(j)}{D^{(n)}(j)}, \tag{5.3}$$

as the measure of convergence, and continued these steps until the KL divergence fell below 10^{-10}. In our analysis, a spatially uniform profile was assumed as the initial values of the iterative algorithm, and the normalization of the estimated source profile was determined so that the total counts of a folded map were preserved.

We note that the statistical uncertainty of a source profile should also be evaluated especially in the case of low photon statistics, though simple calculation of the Poissonian errors for a decoded profile can cause the underestimation of the errors since it ignores the uncertainty associated with the reconstruction with the EM-algorithm. While the uncertainty of the EM-algorithm is generally evaluated by e.g., a bootstrap method[111] and a derivative method using a Hessian matrix,[112] we simply reproduced 100 folded maps fluctuating the original counts according to the Poisson distribution, created 100 source profiles by individually decoding them, and employed the mean and standard deviation of the obtained source profiles as the best-estimate source profile and its errors (notably, it is just rough indication of statistical uncertainty and we ignored other systematic errors such as e.g., the uncertainty of a transmittance pattern).

5.5 Demonstration of Imaging with MCA

5.5.1 Transmittance Patterns of MCA Masks

Figure 5.6 shows the 1×1 period transmittance pattern of each MCA mask at 12.4 keV. We note that we investigated whether images were shifted during data acquisition by dividing the obtained dataset into several parts and comparing the projected profile of the folded map of each part (as depicted in Fig. 5.7). Figure 5.8 shows an example of the shift correction; it represents that the apex of the projected profile moves at a roughly uniform pace before correction. Thus we corrected the position of X-ray events with the image displacement per frame derived by a linear fit of uncorrected data points. The obtained transmittance patterns are slightly different from those of the micrographs shown in section 5.2, but their sharp patterns imply that the mask have certainly periodic structure, which is essential for the Talbot effect. The pattern A, B and C have the entire transmittance of 31.1%, 33.9% and 30.0%, respectively (n.b., only the transmittance of the pattern B was uncorrected for the fluctuation of the beam intensity due to the absence of data). These results show that the transmittance is dramatically improved in comparison with that of the periodic pinhole mask ($\sim 1.3\%$), and hence the adoption of a MCA mask would increase the effective area of MIXIM by about 25 times. Notably, they are lower than the design values of the opening fraction (~ 0.5), mainly because of absorption by the substrates and imperfection of fabrication. The transmittance at 6.2 keV was derived to be about 10% in the same way, which also shows that the thicknesses of the substrates should be reduced for observation at energy below 10 keV.

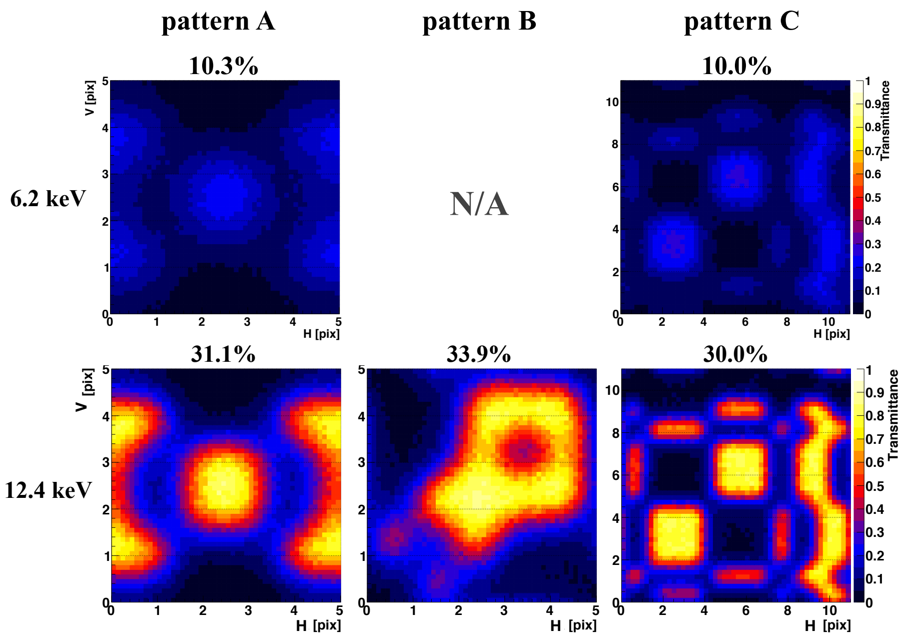

Figure 5.6: Transmittance pattern of each MCA mask at 12.4 keV.

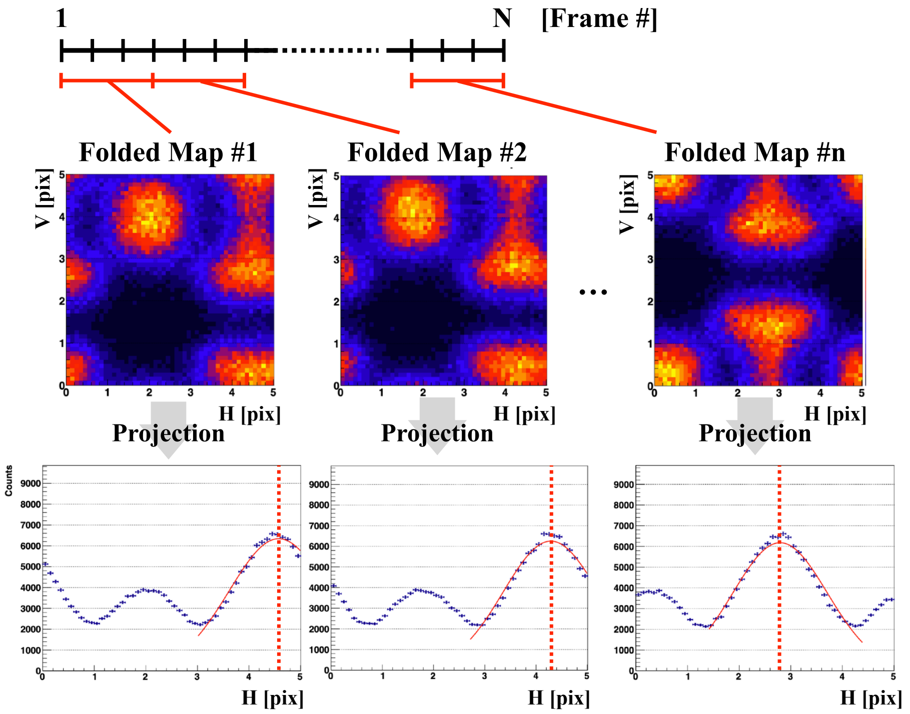

Figure 5.7: Schematic chart of the shift correction of the folded maps. Dividing the obtained dataset into several parts and created the folded map for each part, we derived the image displacement per frame.

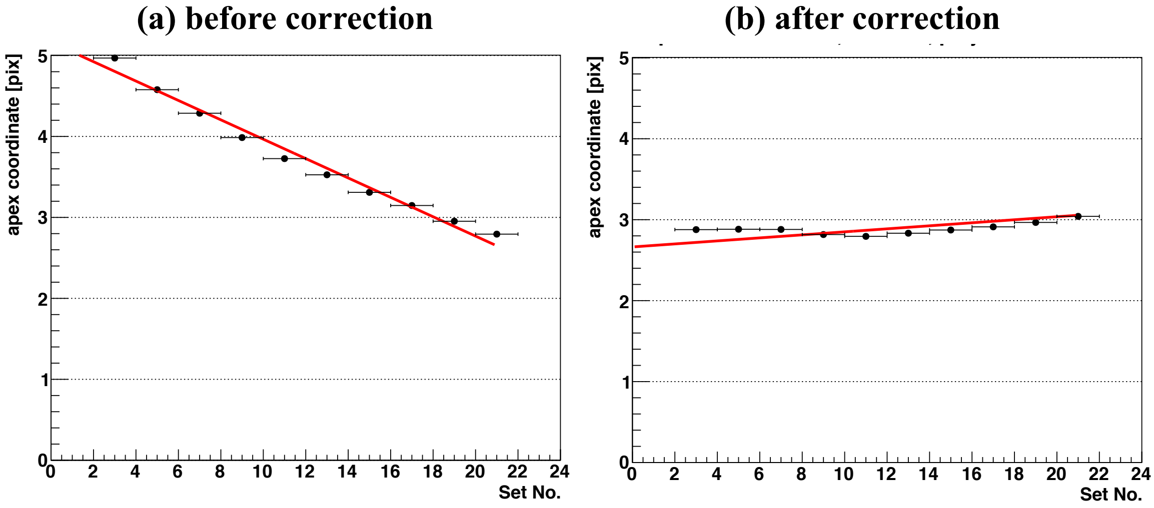

Figure 5.8: The apex position of the projected profile (pattern A) for each divided dataset, (a) before and (b) after shift-correction. Red solid lines denote the results of the linear fit.

5.5.2 Reconstructed Source Profiles

Figure 5.9 (a) shows the folded maps obtained with the MCA masks. These maps were binned in 50×50 bins, and normalized by the average counts per bin. The pattern A and B have the FOV of $1.66'' \times 1.66''$ while the pattern C has that of $0.75'' \times 0.75''$. The folded maps of the pattern A and B roughly agree with the transmittance patterns obtained at $z = 1.58\,\mathrm{cm}$, which demonstrates that such complex aperture patterns can also form self-images for a point source in an X-ray band and can be applicable for MIXIM. Decoding these folded maps with the EM-algorithm, we reconstructed source profiles (we refer to them as decoded maps). Figure 5.9 (b) shows the results; they were smoothed with a Gaussian filter ($\sigma \sim 1$ bin) for better visualization. While the decoded maps indicate a point-source profile for the pattern A and B, the decoded map with the pattern C represents the horizontally elongated beam profile, which is consistent with the X-ray beam divergence. It means that our decoding process succeeded in reconstructing the accurate image without misestimation. Notably, the configuration with the pattern C has a long mask-sensor distance z of 786 cm, which enables us to resolve the beam profile with a higher angular resolution than those with the pattern A and B.

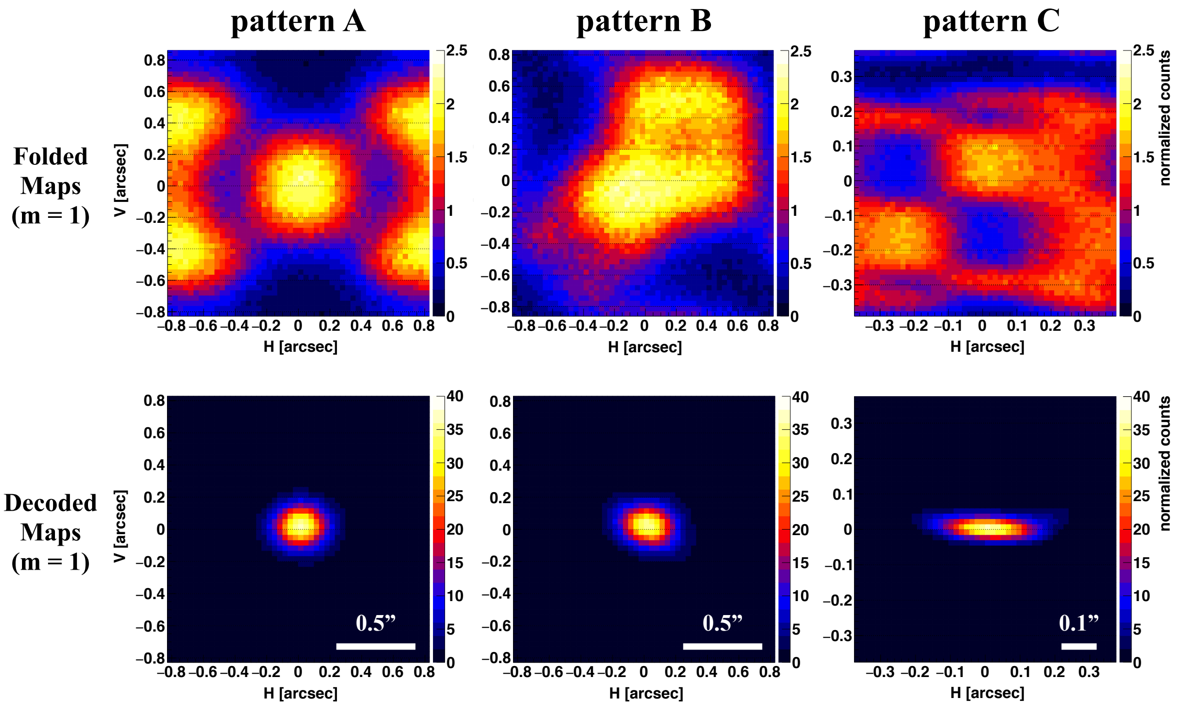

Figure 5.9: Folded map (upper panels) and decoded map (lower panels) of each MCA mask, normalized by the average counts per bin. Both single-pixel and double-pixels are used in these maps.

We then fitted the reconstructed source profiles with a 2D Gaussian function to measure the beam divergence quantitatively. The best-fit models of the pattern A, B and C are displayed in Fig. 5.10, and best-fit parameters are summarized in table 5.1. We note that these results should not be compared with the image width in the case of the multi-pinhole system in section 4.4, since the decoded maps are not actual images but estimated profiles of an X-ray source. It means that a decoded map converges to the delta function in the ideal case where a transmittance pattern and an obtained folded map are perfectly consistent and both of them have an infinite number of bins. In other words, the width of a reconstructed image depends on the uncertainty of a transmittance pattern and the number of bins (i.e., the bin size of folded maps should not be much smaller than the spatial resolution of the detector, since it leads to the underestimation of the width in the case of point-source profiles).

The horizontal FWHM derived by the fit for each pattern is in reasonably good agreement with the horizontal beam divergence of $0.28''$, while the vertical FWHMs are not consistent with the vertical beam divergence of $0.06''$. In our experiment, the beam intensity slightly fluctuated during the measurement of the transmittance pattern, and deviation from the ideal configuration or the slight shift of the imaging system during data acquisition yielded systematic errors. The overestimation of the vertical beam divergence with the pattern A and B is probably ascribed to them. Regarding such non-zero widths in the vertical direction as the angular resolution of this system, the angular resolution is derived to be $\sim 0.2''$ with a baseline of 157 cm. If we adopt a detector with higher spatial resolution and obtain folded maps with an adequate photon statistics and less systematic errors, the angular resolution should be improved by increasing the number of bins even with the same baseline of 157 cm (an increase of the number of bins also results in enormous calculation costs). Meanwhile, the reason that the pattern C underestimated the vertical beam divergence is that the derived sharp beam profile could not be approximated with a simple 2D Gaussian function. It implies that imaging with the pattern C would have an angular resolution high enough to clearly resolve the intrinsic beam profile.

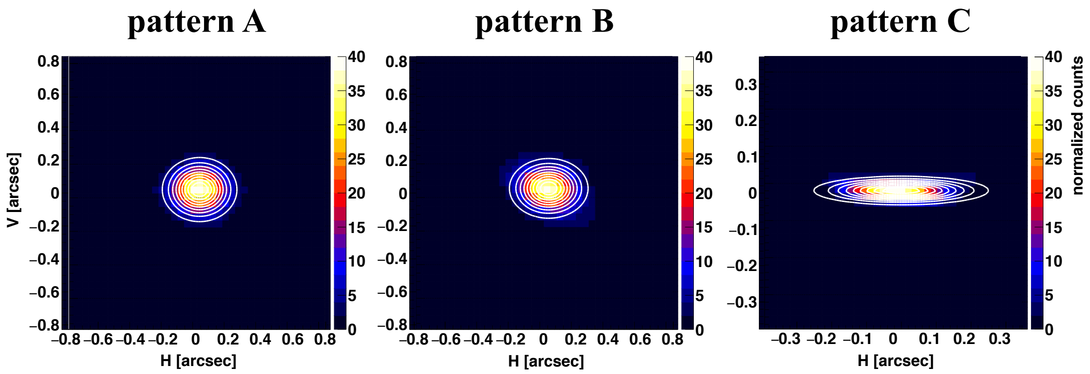

Figure 5.10: Same as the bottom panels of Fig. 5.9, but the best-fit models are overplotted as white contours.

Table 5.1: Summary of the fit with a 2D Gaussian function.

Configuration				Performance index	
Pattern	z (cm)	E (keV)	m	H-FWHM (arcsec)	V-FWHM (arcsec)
A	157	12.4	1	$0.259^{+0.001}_{-0.001}$	$0.208^{+0.001}_{-0.001}$
B				$0.272^{+0.002}_{-0.002}$	$0.193^{+0.001}_{-0.001}$
C	786			$0.274^{+0.023}_{-0.019}$	$0.041^{+0.001}_{-0.001}$

5.5.3 Separation of Two Point-sources

Whereas the extent of the decoded maps roughly represent the angular resolution of this system, it is not necessarily the appropriate evaluation criterion of the angular resolution since the source profile can be misestimated in the decoding process. Hence, we also conducted an experiment assuming the observation of two point sources in the same way as section 4.4, to verify the imaging performance of MIXIM with MCA masks. The configuration is basically the same as Fig. 4.14, while we adopted the MCA mask of the pattern A and adjusted a mask-sensor distance of 157 cm ($m = 1$). We rotated the optical rail in the azimuthal direction in steps of $0.108''$, and obtained frame data with 12.4 keV X-ray irradiation for each step. Combining the events extracted from the on-axis and off-axis (θ_{H} apart from on-axis) data, we simulated the observation of two sources θ_{H} apart from each other. Since the exposure time and the number of frames were fixed for each step, the two sources have the almost same brightness. Figure 5.11 shows the decoded maps with each θ_{H} (from $0.108''$ to $0.648''$). The two sources are correctly reconstructed in terms of both spatial structure and brightness, and they can be clearly distinguished without any prominent artifacts at least in the case of $\theta_{\mathrm{H}} = 0.540''$ (n.b., the horizontally-elongated beam profile slightly deteriorated the resolving capability as mentioned in section 4.4). From these results, we concluded that MIXIM with the pattern A has a high angular resolution of $\sim 0.5''$ even with the baseline of only 157 cm.

5.5.4 Decoding with Low Photon Statistics

Although our decoding process successfully reconstructed source profiles so far as the X-ray beam in SPring-8 provided sufficient photon statistics even in a short observation time, we need to decipher folded maps with limited photon statistics in the case of e.g., the observation of astrophysical X-ray sources with low photon flux. Therefore, we re-analyzed the aforementioned data of “single point source” (see Fig. 5.9) and “two point sources” (see Fig. 5.11), varying the total X-ray event number N from 10 to 10^5. Specifically, we created a folded map with X-ray events (N events in total) randomly extracted from the original event data. We repeated this process 100 times and then deciphered each folded map individually, which yielded 100 independent decoded maps. Notably, in the case of two point sources, we randomly extracted $N/2$ events from both on-axis ($\theta_{\mathrm{H}} = 0.00''$) and off-axis ($\theta_{\mathrm{H}} = 0.54''$) data and blended them so that the total event number had N for each process. Subsequently, the mean and standard deviation of the 100 decoded maps were calculated for each bin, and employed them as the reconstructed source profile and its standard errors.

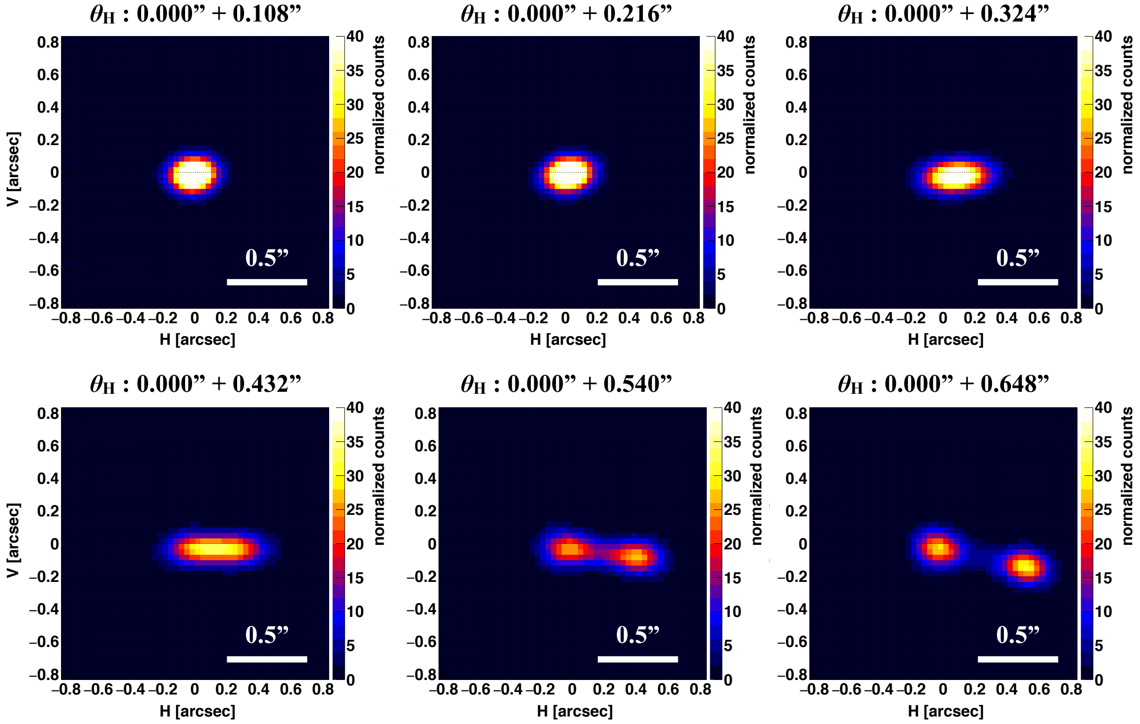

Figure 5.11: Decoded maps obtained by the blend of the on-axis and off-axis data, assuming the observation of two point-sources. θ_H represents the incident angle measured from the beam axis.

Figure 5.12 and 5.13 show the source profiles with N of 10^2, 10^3 and 10^4 in the case of “single point source” and “two point sources”, respectively (each decoded map was binned with 25 × 25 pixels). The decoded maps in the top panels are normalized by the average counts per bin as with Fig. 5.9 and 5.11, while those in the bottom panels are normalized by the standard error for each bin (i.e., they represent the significance for each bin). While the image of the original source profile is clearly reconstructed without prominent artifacts in the decoded maps with $N = 10^4$, those with $N = 10^2$ have relatively blurred profiles; it is ascribed to the fact that the spatial deviation of the source profiles increases as N decreases (n.b., each source profile is not highly blurred in our analysis). these results imply that low statistics result in an increase of the uncertainty of a source position or its profile, whereas its approximate position can be reconstructed even with $N = 10^2$ at least in the case of a single point-source. Notably, the standard errors with these source profiles are larger than the simple statistical errors, and actual observation would have larger uncertainty, due to additional systematic errors (e.g., the uncertainty of a transmittance pattern).

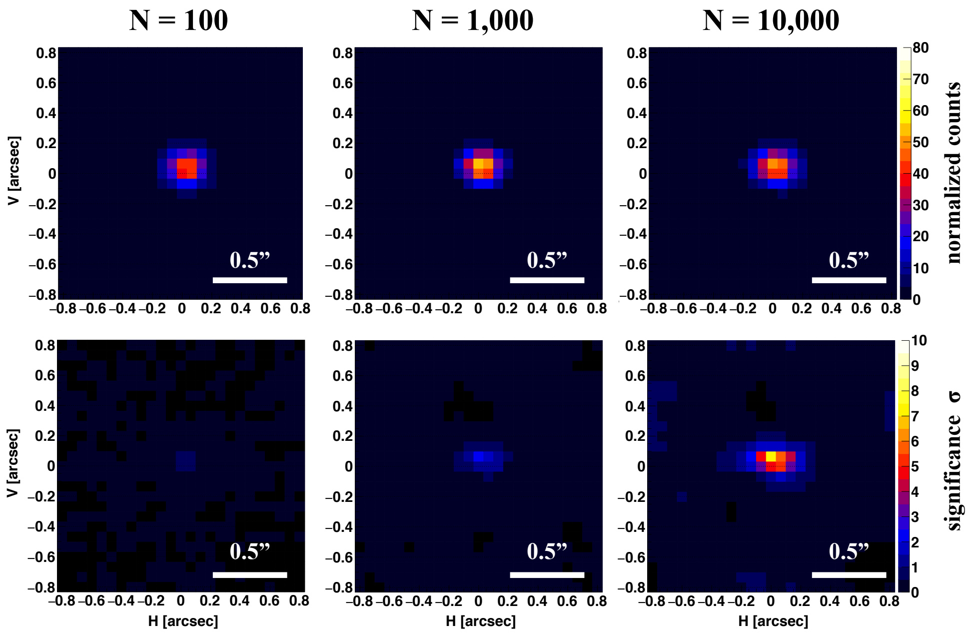

Figure 5.12: From the left, decoded maps with the total X-ray event number of 10^2, 10^3 and 10^4 in the case of a single point source. Those in the top and bottom panels are normalized by the average counts per bin and the significance for each bin, respectively.

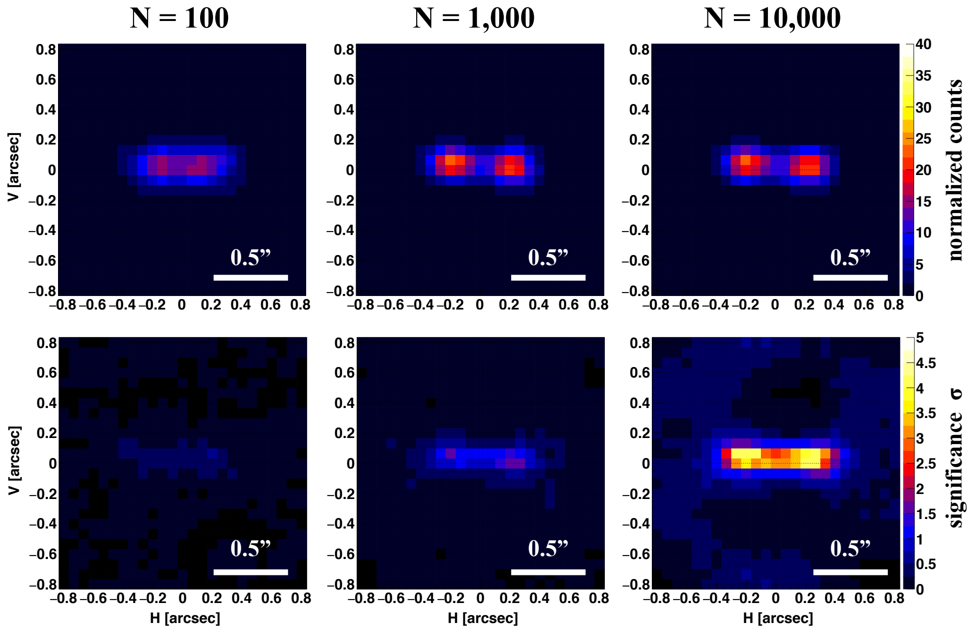

Figure 5.13: Same as Fig. 5.12, but in the case of two identical point sources $0.54''$ apart from each other. It indicates that MIXIM maintains the angular resolution of $\sim 0.5''$ even for $N = 10^3$.

In order to evaluate the spatial deviation of the reconstructed source profiles, we defined three source regions as depicted in the left panel of Fig. 5.14, and calculated the count ratio of events in the source region to those in the entire region, for each of the 100 decoded maps. If these decoded maps have no spatial deviation, the derived count ratios have the almost same value. Thus, we plotted the mean and standard deviation of these ratios varying the event number N, for each region. The right panel of Fig. 5.14 shows the result (the plot color corresponds the region color in the left panel). The ratio for each region settles at a certain value with a low standard deviation when $N > 10^3$, while it gradually declines as N decreases, which means that the image protrudes from the source region in some decoded maps. The large standard deviation implies that the degree of the protrusion is varied among 100 decoded maps. Notably, these ratios are significantly lower than unity even for $N = 10^5$, which means that few percent of the total counts appears as artifacts even with high photon statistics. However, this plot shows that MIXIM with MCA masks has a stable point spread function and maintains high angular resolution if with $N > 10^3$.

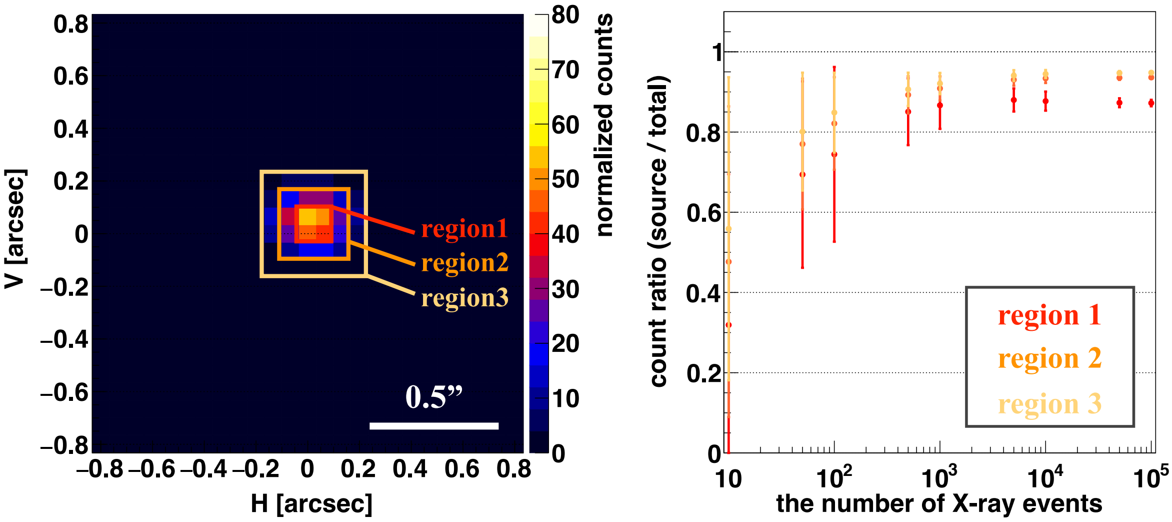

Figure 5.14: (Left) Definition of the source regions, over-plotted onto the decoded map with $N = 10^3$. (Right) The count ratio of the events in the source region to those in the entire region for each N. The plot color matches the used source region defined in the left panel.

5.5.5 Energy Dependence

Whereas self-images are simply blurred as m increases or decreases from unity in the case of a multiple pinhole mask, self-images of MCA masks are supposed to be complexly changed by interference with the shift of m. It implies that an energy shift causes not only the simple deterioration of angular resolution but also misestimation of a source profile. Hence, we shifted the X-ray beam energy from 12.4 keV for the pattern A with the same configuration, and investigated the influence of the energy shift on folded maps and reconstructed source profiles. Figure 5.15 shows the obtained folded maps at a variety of beam energies. They apparently have the similar profiles each other at least within an energy range of ±5%.

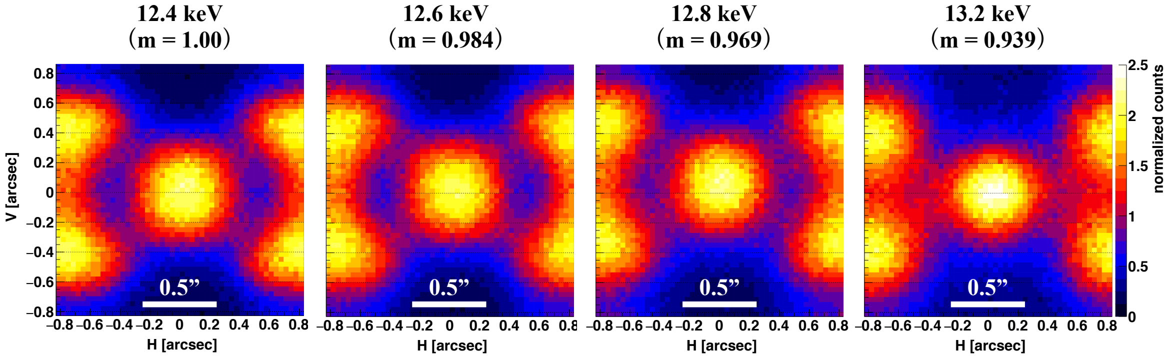

Figure 5.15: From left panels, folded maps with the beam energy of 12.4 keV, 12.6 keV, 12.8 keV and 13.2 keV. All folded maps were obtained with the same configuration (the pattern A, $z = 157$ cm) except for X-ray beam energy.

Then, we reconstructed the X-ray source profile for each folded map, with the transmittance pattern at 12.4 keV. Figure 5.16 (a) shows the results; the visibility of the source profile gradually declines as m departs from unity, as with the result of the multi-pinhole mask. On the other hand, it demonstrates that prominent artifacts do not appear within an energy band ($\Delta E/E$) of ±5%, where it could be resolved with typical solid state detectors (with an energy resolution of $\sim 3\%$) at $m = 1$. We also confirmed that the folded map at 10 keV ($m = 1.24$) represents the totally different profile from the original transmittance pattern. In this case, the reconstructed source profile splits in several peaks and some artifacts appear away from the source, which means that we misestimate the authentic X-ray source profile when we overextend the energy band. Notably, given that only a diffraction effect causes the blurring of the reconstructed source profiles, we can estimate the degree of blurring with the Fresnel diffraction calculation already performed in section 3.2. Hence, we then replaced the transmittance pattern to a "diffracted transmittance pattern", i.e., the diffraction pattern with at $z = 157\,\mathrm{cm}$ assuming that the original transmittance pattern (shown in Fig.5.6) was placed at $z = 0\,\mathrm{cm}$. Consequently, we obtained the reconstructed profiles as displayed in Fig. 5.16 (b); they entirely have less visibility even though the expected diffraction effect due to the energy shift is taken into account, which suggests that the actual aperture pattern and the 1×1 transmittance pattern are not identical. Such a correction does not improve the imaging performance of MIXIM at the moment, but it might be useful if we obtain more accurate transmittance patterns.

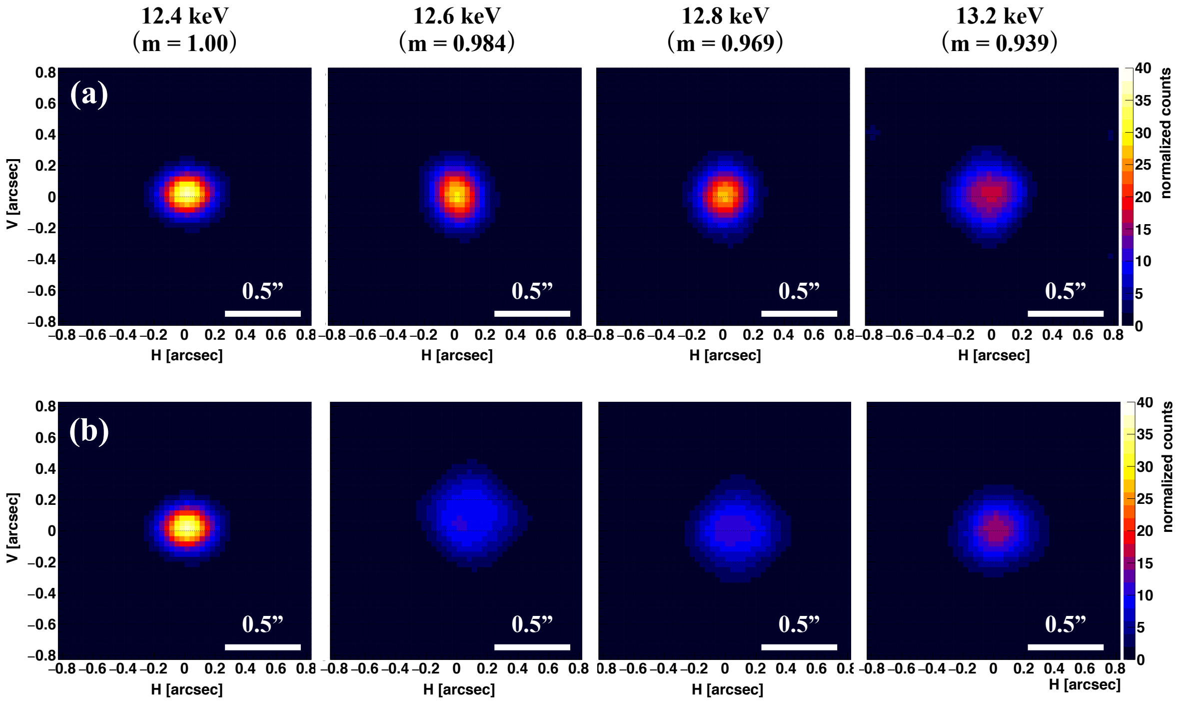

Figure 5.16: (a) From left panels, decoded maps with the beam energy of 12.4 keV, 12.6 keV, 12.8 keV and 13.2 keV. (b) Same as (a), but obtained with the decoding process considering the diffraction effect.

5.6 Reduction of Substrate Thickness

As mentioned in the previous section, thick substrates of MCA masks decline an effective area especially in a soft X-ray band. Hence, we newly employed two types of MCA masks (named as the pattern A′ and C′). These masks have the same design of the previous MCA masks (pattern A and C) as seen in their micrographs (Fig. 5.17), while the thicknesses of the substrates were reduced from 550 µm to 13 µm. In order to evaluate the performance, we performed an experiment in 2021, with the same configuration as that conducted in 2020.

We first obtained transmittance patterns with the new MCA masks for 6.4 keV and 12.4 keV at the distance z of 0.528 cm. Figure 5.18 shows the obtained transmittance pattern for each MCA mask (after correction of the shift during data acquisition), which clearly demonstrates that the reduction of the substrates enhances the transmittance in comparison with the previous MCA masks as shown in Fig. 5.19. In particular, the transmittance at 12.4 keV is the almost same as the opening fraction expected from the original design. Such a reduction of substrates is especially beneficial for performing high-resolution imaging for a particular fluorescent line (e.g., Fe Kα), since fluorescent lines from relatively abundant ions are typically included in a soft X-ray band below 10 keV where the absorption by the substrate is not negligible.

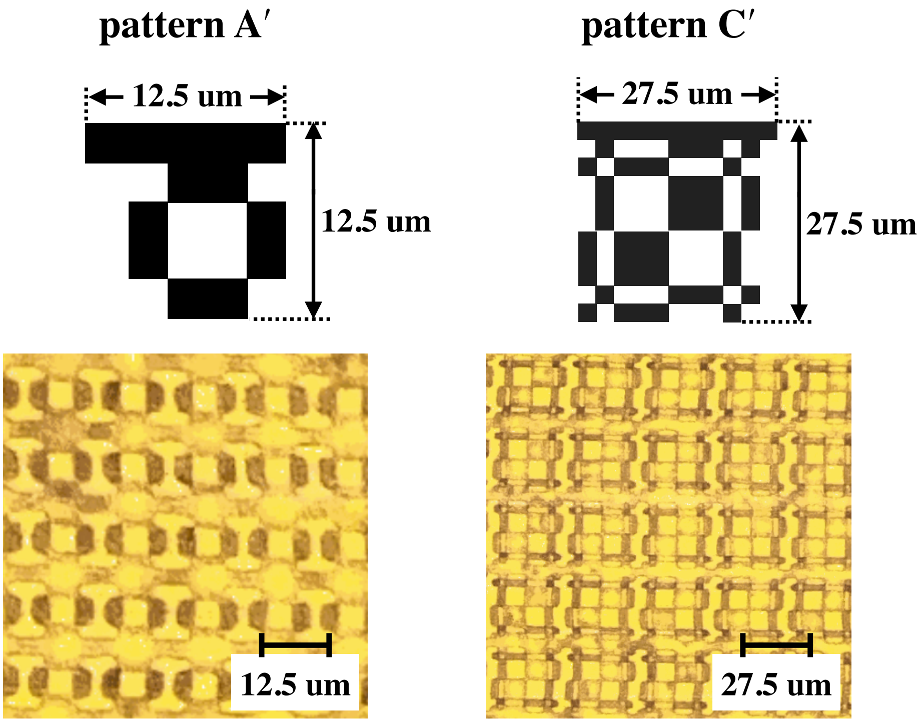

Figure 5.17: Micrographs of the new MCA masks whose substrates were reduced to 13 µm. They were fabricated by the LIGA process, as with the previous masks.

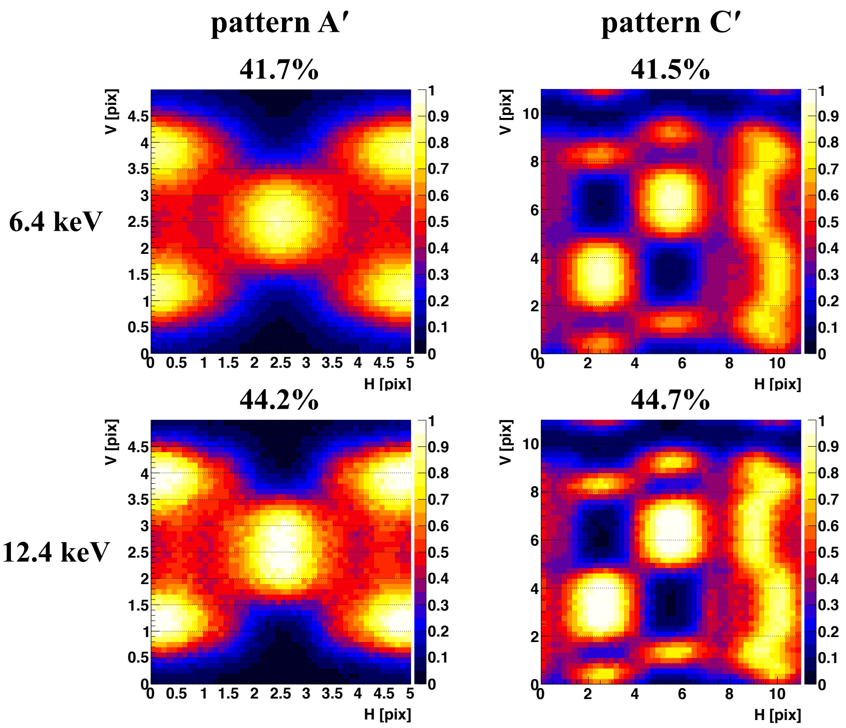

Figure 5.18: Transmittance patterns for pattern A′ and C′, at 6.4 keV and 12.4 keV.

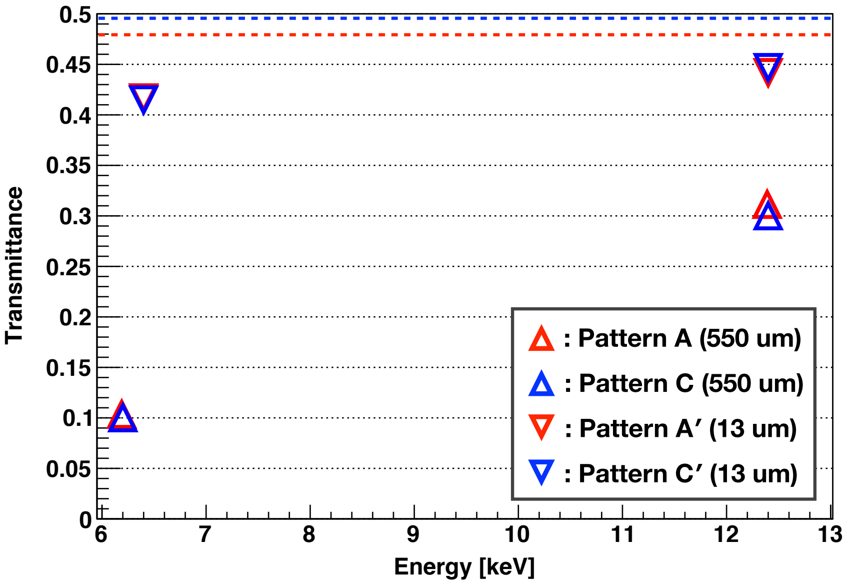

Figure 5.19: Entire transmittance obtained with the pattern A, C, A′ and C′. Dashed lines denote the opening fraction expected from the original mask design. The transmittance of the MCA masks with a substrate thickness of 13 µm significantly increases in comparison with the result with the previous MCA masks.

Figure 5.20 (a) and (b) show the obtained folded maps and decoded maps at 12.4 keV ($m = 1$), respectively. While the folded maps and decoded maps with the pattern A′ are consistent with the results with the previous mask with a substrate thickness of 550 µm, the visibility of the decoded map relatively decreases in the case of the pattern C′. As the transmittance pattern also shows less sharpness in comparison with that obtained in 2020, the pattern C′ might not maintain the periodicity over the entire mask, which can cause the low visibility. The result of the pattern A′ demonstrates that new MCA masks can enhance the effective area of MIXIM maintaining the high angular resolution. On the other hand, the thick substrate is required for the equipment of gold absorbers with high aspect ratio, which is necessary for imaging in a higher energy band. In addition, we should verify that the MCA masks with thin substrates can withstand vibration and acoustic tests in advance for actual observation in orbit. Taking these points into consideration, the thickness of MCA masks should be optimized according to a target energy band.

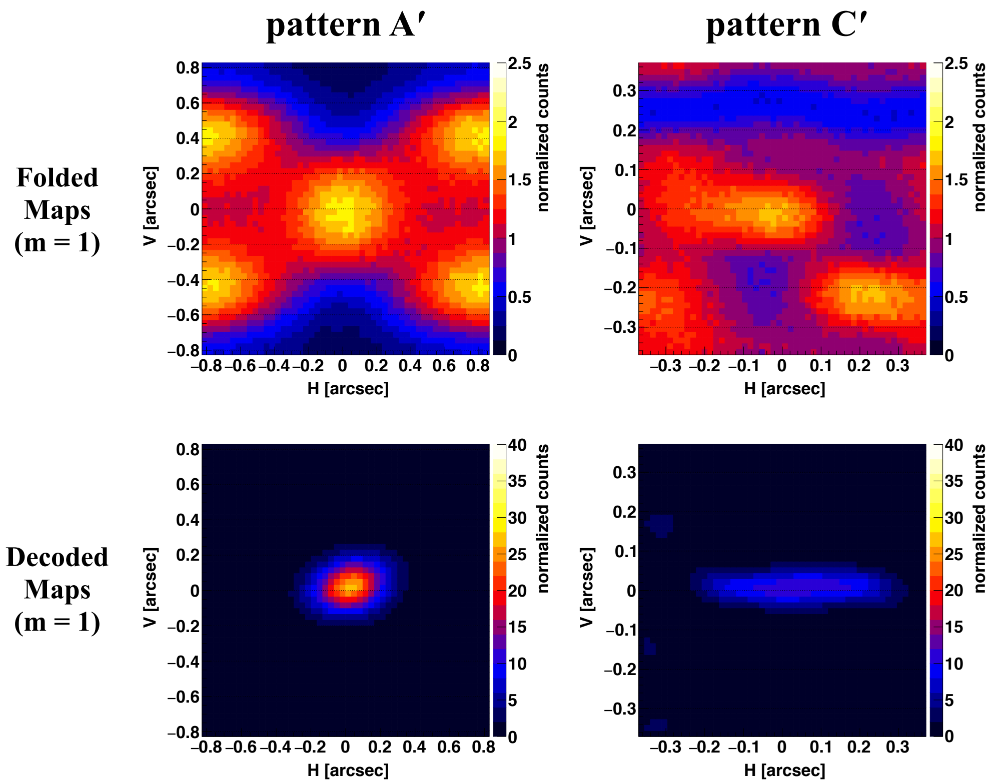

Figure 5.20: (Top) Folded maps and (Bottom) decoded maps obtained with the beam energy of 12.4 keV ($m = 1$). Left and right panels show the pattern A′ and C′, respectively.

5.7 Imaging of a Target with Complex Structure

Finally, we attempted to obtain the image of an X-ray source with more complex spatial structure, by applying the method used in the two point-source observation. In 2022, we assembled the imaging system comprised of the MCA mask (pattern A′) with a substrate thickness of 13 µm and GMAX0505 on the rotation stage, so that the system can rotate in both azimuth and zenith direction in steps of $0.216''$. The distance between the mask and sensor was set to be 1.26 m, where m is unity for 10.0 keV X-rays (the FOV is derived to be $2.16'' \times 2.16''$). This configuration enabled us to move the line of sight two-dimensionally, and obtain the X-ray events for each incident direction (the exposure time and frame number are identical for each step as with the case of two point sources). We first created the folded map for each step and confirmed that the imaging system was rotated in steps of $0.216''$ as expected. Afterwards, we blended the X-ray event data with 16 incident angles as shown in Fig. 5.21, assuming the source with ring-shape structure with a diameter of $1.3''$.

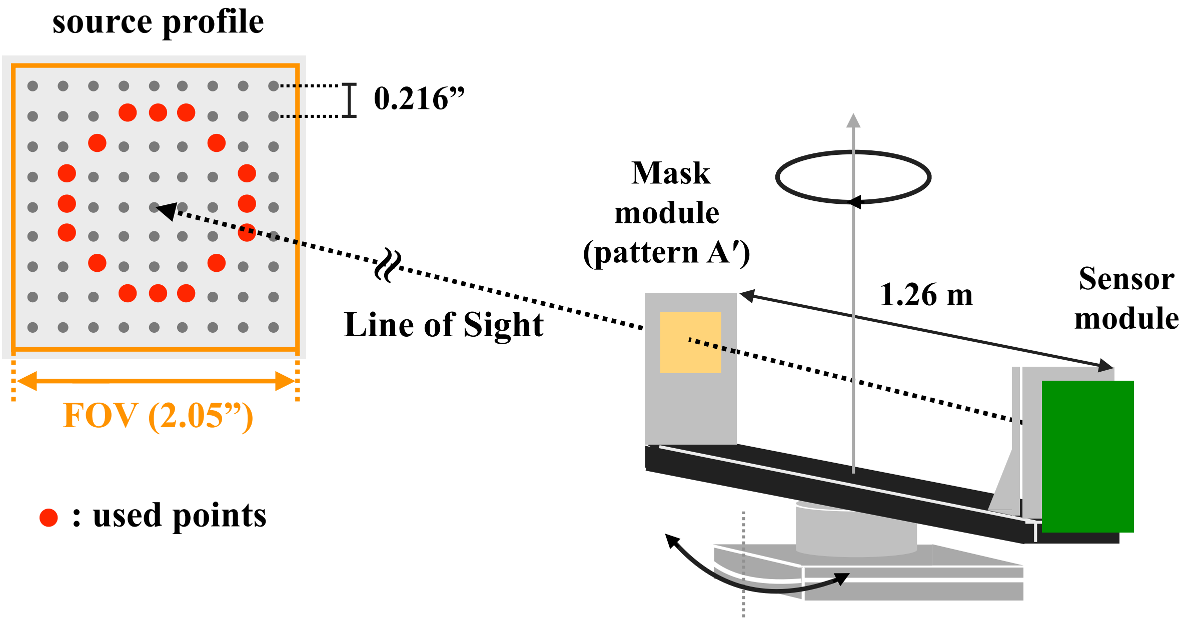

Figure 5.21: Configuration for simulating the observation of X-ray source with complicated structure, such as a “ring-shape” profile. Line of sight can be varied two-dimensionally by shifting the imaging system with the rotation stages. Red points denote the 16 incident angles used in the blended data.

The left panel of Fig. 5.22 shows the obtained folded map binned with 50×50 pixels; it is normalized by the average counts per bin, and has the total X-ray event number of about

8×10^5. Whereas its profile is close to be flat and featureless since it is the superposition of different folded maps with a variety of incident angles, we succeeded in acquiring a ring-shape profile as depicted in the center panel of Fig. 5.22. Apart from that, the right panel of Fig. 5.22 also represents the source profile, but we blended the 16 decoded maps which were individually deciphered for each incident angle. While its profile is slightly sharper than the decoded map created from the blended event data, it also has similar ring-shape structure. Notably, the upper and lower sides of the ring seen in the both decoded maps are roughly twice as bright as the right and left sides, because the horizontally elongated beam profiles overlap each other in the region where the profiles align in the horizontal direction. This experiment demonstrates that our decoding analysis can be applicable even for a source with diffuse structure, though the small difference between two decoded maps implies that it still leaves room for improvement.

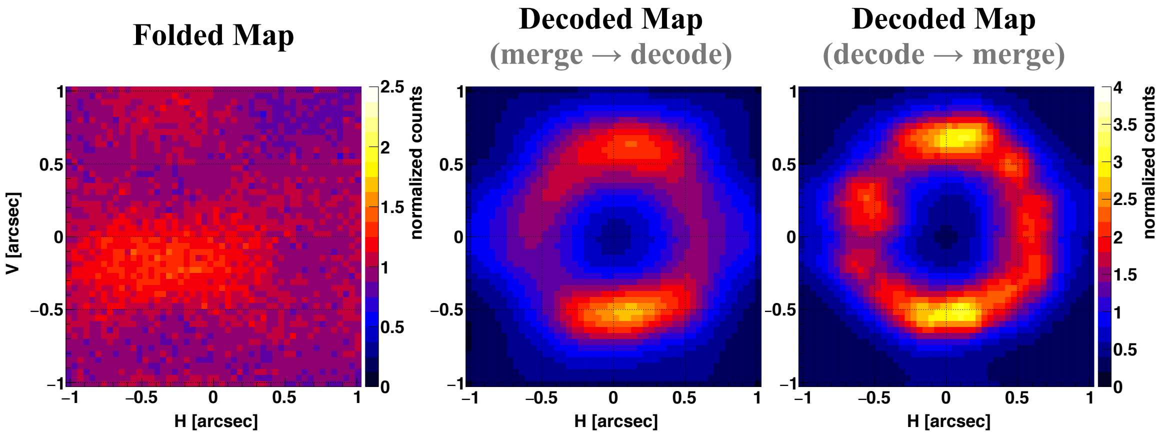

Figure 5.22: (Left) Folded map and (Center) decoded map obtained with the blended event data as shown in Fig. 5.21. (Right) Decoded map with the same dataset, but we individually deciphered each dataset and then added them up to reconstruct the ring-shape profile. These decoded maps are moderately smoothed for better visualization.

Chapter 6

Application to X-ray Imaging Polarimetry

MIXIM has a capability for not only high-resolution X-ray imaging but also X-ray polarimetry, thanks to the adopted CMOS sensor with high spatial resolution. In this chapter, we introduce its principle and past experiments regarding X-ray polarimetry with solid-state detectors, and describe the experiment for the evaluation of the polarimetric performance of the CMOS sensor (see also Asakura et al. 2019[102]).

6.1 Silicon Pixel Sensors as X-ray Polarimeters

As already explained in section 2.2, photoelectron tracking is one of the effective measures for X-ray polarimetry, since the emission angle of a photoelectron depends on the polarization angle of an incident X-ray photon. Such photoelectron tracking X-ray polarimeters require a detector with a spatial resolution high enough to resolve the trajectories of photoelectrons. In the case of gas pixel detectors such as those onboard *IXPE*, the average trajectory lengths at 2 keV and 8 keV are approximately 100 µm and over 1 mm,[82] which can be sufficiently resolved with a spatial resolution of few tens of µm (e.g., the detector of IXPE has a spatial resolution of 50 µm). It enables us to perform polarimetry in a soft X-ray band, whereas their effective areas are quite low to conduct practical observations above 10 keV. On the other hand, silicon pixel sensors have much higher effective areas in comparison with gas pixel detectors, which implies that they would have a capability to exploit the 10–20 keV band where existing X-ray polarimeters have almost no sensitivity. However, the mean free path of photoelectrons in silicon detectors is estimated to be less than 1 µm at 10 keV, according to the empirical formula of $r\ (\mu\mathrm{m}) = [E_\mathrm{e}/10\ (\mathrm{keV})]^{1.75}$, where E_e is the initial photoelectron energy.[113] It indicates that photoelectron tracking with silicon pixel sensors necessitates much higher spatial resolution than that with currently used gas pixel detectors to obtain X-ray polarimetric information at least in a 10–20 keV band.

The first proof-of-concept experiment of X-ray polarimetry with a CCD was conducted by Tsunemi et al. in 1992;[114] they succeeded in detecting X-ray polarization with a CCD with a pixel size of 12 µm within an energy range from 15 keV to 37 keV. They assumed that the striding direction of double-pixel events reflects the spread direction of primary charge clouds which represents the emission direction of photoelectrons, and derived the number ratio of vertically striding double-pixel events to the entire double-pixel events, while rotating the CCD. The number ratio had a significant modulation while its amplitude was less than 5% even at 37 keV (n.b., they reported that the modulation had a larger amplitude as the incident X-ray energy increased, since an X-ray photon with low energy produces the short track of a photoelectron, which is susceptible to charge diffusion). Afterwards, a similar experiment with a CCD with a smaller pixel size of 6.8 µm was conducted at 33 keV by Buschhorn et al. (1994),[115] of which result indicates that the high spatial resolution leads to enhance the amplitude of modulation (i.e., high sensitivity as an X-ray polarimeter). In addition, the employment of the events spreading over multiple pixels could be effective for improving polarimetric performance.[116]

However, the amplitudes of their modulation curves were quite low especially below 30 keV, which means that the conventional X-ray CCDs do not have practical polarimetric sensitivity in such an energy band. In fact, although recent X-ray astronomical satellites were equipped with X-ray CCDs as focal plane detectors, no significant X-ray polarization from astrophysical X-ray sources has been detected with the X-ray CCDs so far mainly due to the pixel size. Meanwhile, we found that GMAX0505, a scientific CMOS sensor with a pixel size of 2.5 µm, can be applied for X-ray imaging in a photon-counting mode. X-ray spectra obtained with this sensor (Fig. 4.4) indicate that some incident X-rays are detected as double-pixel events even at 12.4 keV, which suggests that this fine-pixel sensor is useful not only for X-ray high-resolution imaging but also X-ray polarimetry. Hence, we also evaluated the polarimetric performance of GMAX0505 during the proof-of-concept experiments of MIXIM.

6.2 Performance Evaluation Experiments

6.2.1 Calibration of the Beam Polarization in BL20B2

In order to investigate the accurate polarimetric performance, we first measured the polarization of the synchrotron X-ray beam in BL20B2 which was expected to be highly polarized in the horizontal direction, as mentioned in e.g., Katsuta et al. (2009).[117] We assembled a scattering polarimeter system with a beryllium target with a diameter of

5 mm and a length of 20 mm and XR-100CdTe, a cadmium telluride (CdTe) detector provided by Amptek Inc., in the downstream hutch in BL20B2. We fixed the system so that the X-ray beam hit the beryllium target, and measured the azimuthal distribution of scattered X-rays by rotating XR-100CdTe. Figure 6.1 (a) shows a photo of the actual setup while Fig. 6.1 (b) shows the obtained azimuthal distribution of the X-ray counts. The distribution has peaks at approximately at 0° and 180°, which indicates that the X-ray beam was surely polarized in the horizontal direction, and its modulation was obtained to be 94.05% ± 0.03% at 12.4 keV and 93.26% ± 0.08% at 24.8 keV, respectively. Since the modulation factor of our system was geometrically calculated to be 94.7%, we concluded that the X-ray beam has polarization degree of 99.31% ± 0.03% at 12.4 keV and 98.48% ± 0.08%, which agrees with the expectation.

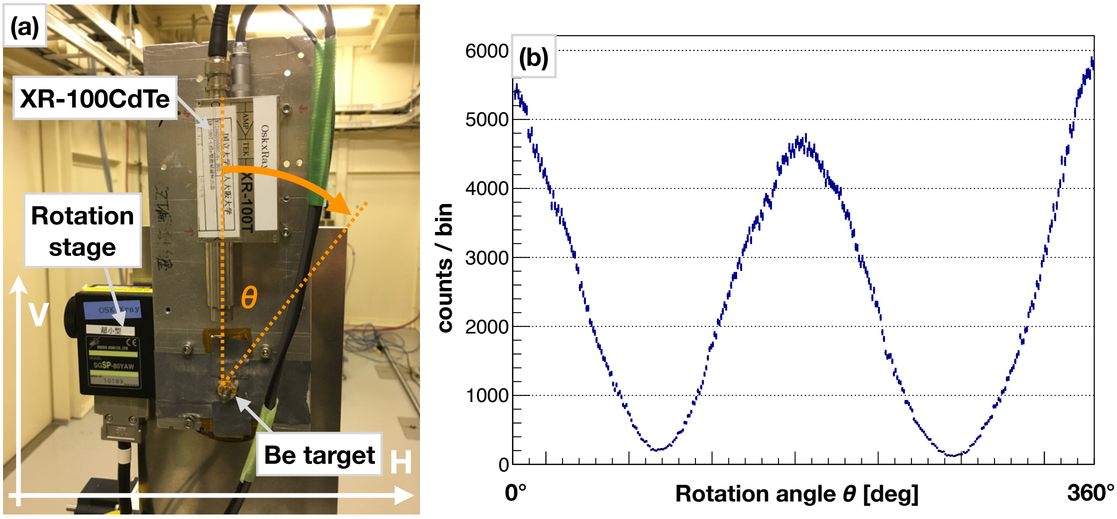

Figure 6.1: (Left) Scattering polarimeter system used for the measurement of X-ray beam polarization properties. (Right) Modulation curve obtained with the scattering polarimeter. The high amplitude implies that the X-ray beam has a high degree of polarization.

6.2.2 Polarization Measurement with GMAX0505

After the calibration of the X-ray beam polarization, we irradiated the X-ray beam to GMAX0505 for the evaluation of the polarimetric performance. Notably, we should derive the modulation factor (MF) for both the horizontal and vertical axes of GMAX0505, since the striding direction of double-pixel events can be anisotropic even for an unpolarized X-rays. Hence, we rotated GMAX0505 from 0° to 90° as displayed in Fig. 6.2, took data for each detector angle at 12.4 keV and 24.8 keV, and counted the number of double-pixel events only within the energy range around the photopeak to filter out the background. Notably, since 24.8 keV X-rays surpass the observable energy range with an usual gain (a register value of 4), we used a “low gain” (a register value of 0, ~ 12.7 eV/ch) during the data acquisition at 24.8 keV. In the event selection procedure, event and split thresholds were aligned with those with a usual gain. Figure 6.3 (a) and (b) show actual images of 12.4 keV and 24.8 keV X-ray events, respectively. Whereas more than half events were detected as single-pixel events for 12.4 keV, some events spread over multiple pixels. As for 24.8 keV events, the majority of them were categorized as double-pixel or extended pixels. The high ratio of double-pixel events at 24.8 keV is apparently advantageous for X-ray polarimetry, though it should be noted that the absolute detection efficiency of double-pixel events at 24.8 keV is much lower than that at 12.4 keV. The energy dependence of the single-pixel, double-pixel and extended event ratios were also measured from 10 keV to 20 keV in a step of 0.5 keV as summarized in Fig. 6.4. It represents that 20–55% of the total detected events can be used in a 10–20 keV band with our current method.

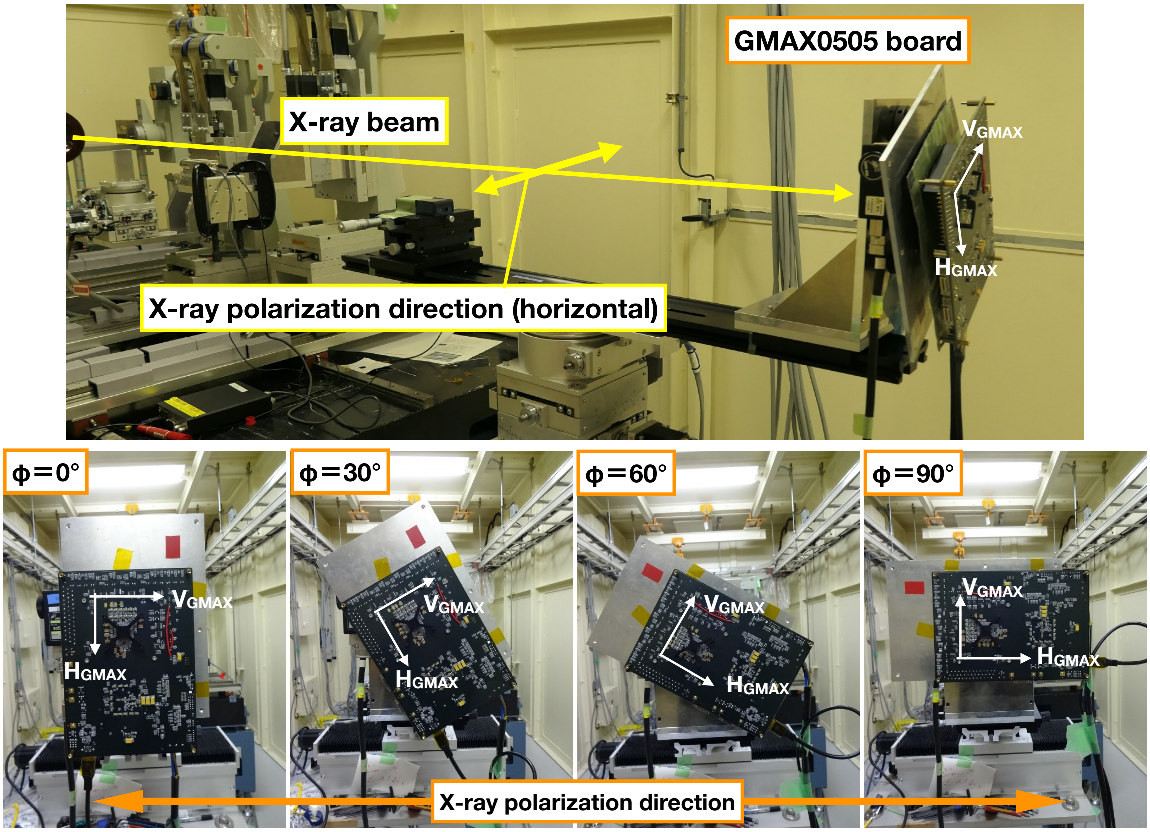

Figure 6.2: Configuration for the evaluation of the polarimetric performance of GMAX0505 (Fig. 4 in Asakura et al. 2019[102]). The X-ray beam is highly polarized in the horizontal direction. The detector angle ϕ can be varied with the rotation stage.

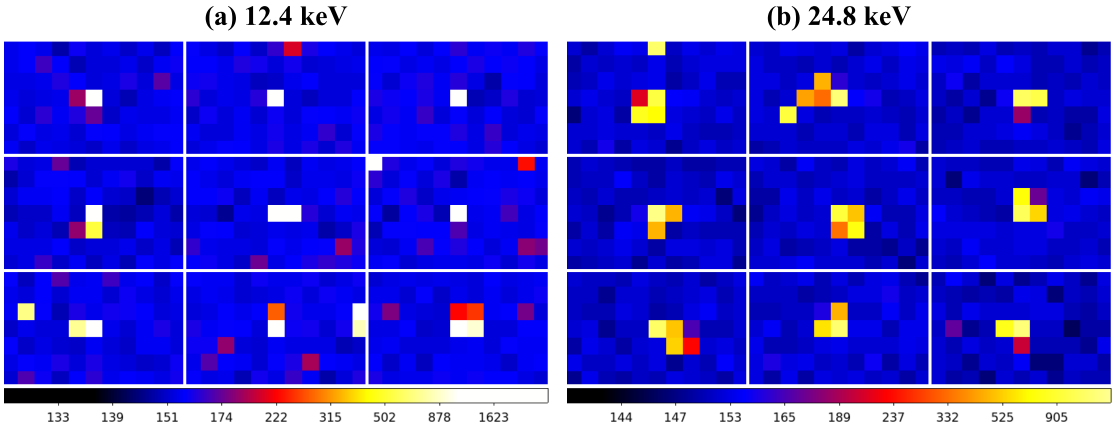

Figure 6.3: Image of some X-ray events randomly extracted from the raw frame data at (a) 12.4 keV and (b) 24.8 keV (Fig. 5 in Asakura et al. 2019[102]). The color scale represents the pulse heights of pixels.

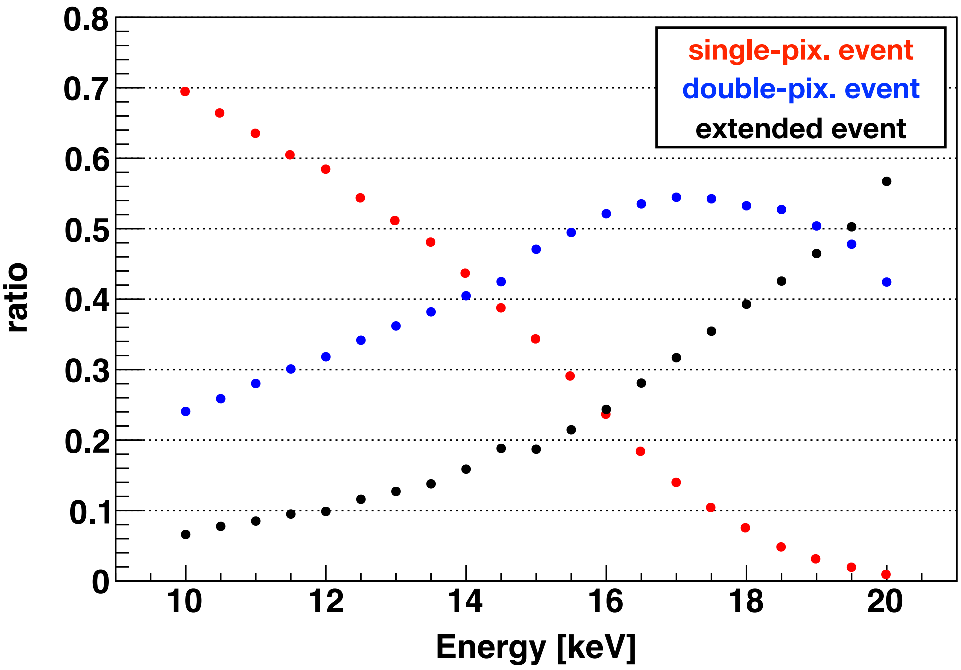

Figure 6.4: Energy dependence of the ratio of the X-ray event types: (red) single-pixel events, (blue) double-pixel events and (black) extended events.

For each detector angle ϕ, the ratio of the horizontally and vertically striding double-pixel events is given by

$$r_{\mathrm{H}}(\phi) = \frac{N_{\mathrm{H}}(\phi)}{N_{\mathrm{H}}(\phi) + N_{\mathrm{V}}(\phi)}, \quad r_{\mathrm{V}}(\phi) = \frac{N_{\mathrm{V}}(\phi)}{N_{\mathrm{H}}(\phi) + N_{\mathrm{V}}(\phi)}. \tag{6.1}$$

Figure 6.5 shows the angular dependence of r_{H} at 12.4 keV and 24.8 keV, from which we clearly see the modulation due to the anisotropy. It represents that a modulation with higher X-ray energy yields a larger amplitude, as seen in the previous experiments with X-ray CCDs. We note that the average of the modulated r_{H} is shifted from 0.5 at both 12.4 keV and 24.8 keV, which means that double-pixel events detected with GMAX0505 have tendency to spread in the vertical axis. With these ratios, we defined the modulation factor of the horizontal axis ($\mathrm{MF_H}$) and vertical axis ($\mathrm{MF_V}$) as the following equation:

$$\mathrm{MF_H} = \frac{1}{P}\frac{r_{\mathrm{H}}(90^\circ) - r_{\mathrm{H}}(0^\circ)}{r_{\mathrm{H}}(90^\circ) + r_{\mathrm{H}}(0^\circ)} \tag{6.2}$$

$$\mathrm{MF_V} = \frac{1}{P}\frac{r_{\mathrm{V}}(90^\circ) - r_{\mathrm{V}}(0^\circ)}{r_{\mathrm{V}}(90^\circ) + r_{\mathrm{V}}(0^\circ)}, \tag{6.3}$$

where P is the polarization degree of the incident X-ray beam. Substituting the derived results, we consequently derived $\mathrm{MF_H}$ and $\mathrm{MF_V}$ as tabulated in table 6.1. The modulation factors demonstrate that GMAX0505 has higher polarimetric sensitivity than existing X-ray CCDs, and can be used for X-ray polarimetry in a 10–20 keV band where existing X-ray polarimeters have not covered so far.

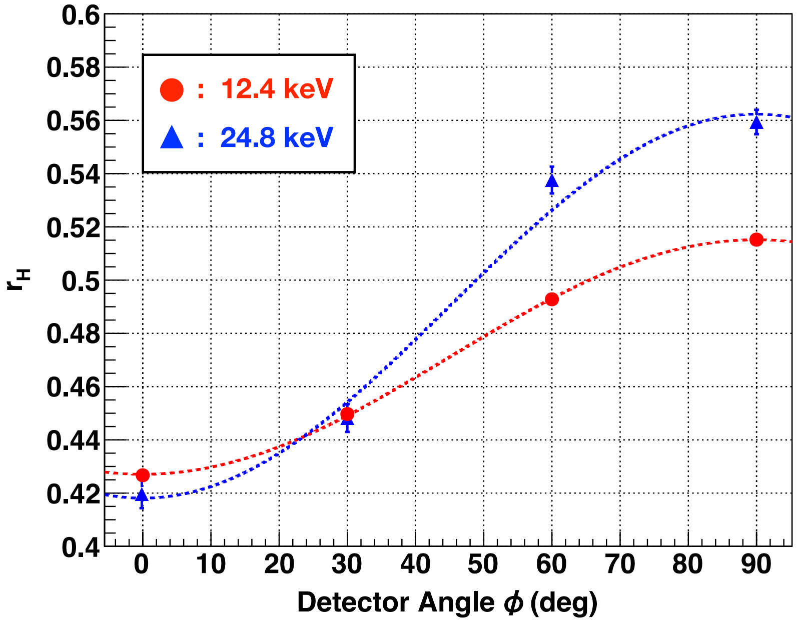

Figure 6.5: Number ratio of horizontally-striding double-pixel events for each detector angle, at (red) 12.4 keV and (blue) 24.8 keV (the same as Fig. 8 in Asakura et al. 2019,[102] but with different event and split thresholds). Significant modulation appears in both energy, which indicates that GMAX0505 has polarimetric sensitivity.

Table 6.1: $\mathrm{MF_H}$ and $\mathrm{MF_V}$ for each X-ray energy.

X-ray energy (keV)	$\mathrm{MF_H}$ (%)	$\mathrm{MF_V}$ (%)
12.4	9.47 ± 0.27	8.43 ± 0.24
24.8	14.5 ± 0.7	13.9 ± 0.7

Whereas we employed the X-ray events within the entire area irradiated by the X-ray beam, we also divided the area into several regions and derived r_H for each region to investigate the spatial dependence of the polarimetric performance. Top panels of Fig. 6.6 shows the distribution of r_H for 12.4 keV and 24.8 keV X-rays (at $\phi = 90°$), while bottom panels represent r_H with area numbers as the horizontal axis, with statistical errors. We see that r_H for each area are consistent with each other, which means that the anisotropy of striding directions is spatially uniform.

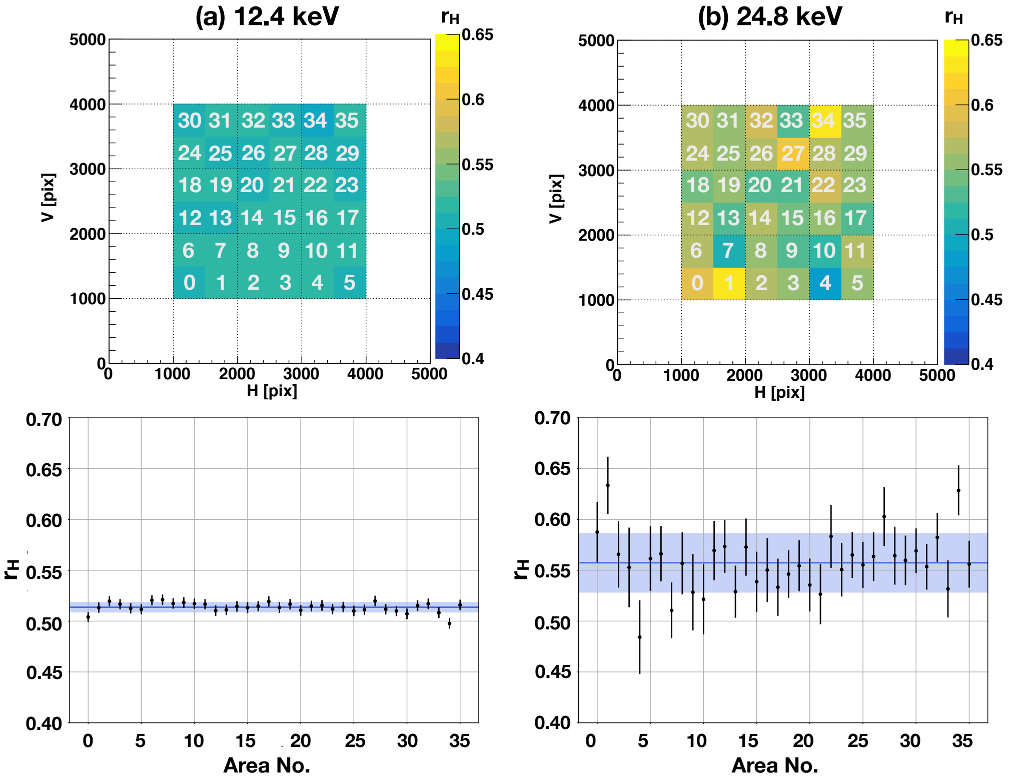

Figure 6.6: (Top) Distribution of r_H at (a) 12.4 keV and (b) 24.8 keV, with the area numbers. (Bottom) r_H for each area with area numbers as the horizontal axis. The blue line and shaded area show the mean and standard deviation of all points, respectively.

6.2.3 Geant4 Simulation

We also evaluated the modulation factor of GMAX0505 by performing numerical simulation with the Geant4 software.[118–120] In the simulation, we used the Geant4 version 10.03.03 and employed the Livermore model as a physics model (taking into account atomic deexcitation processes such as fluorescence X-rays and Auger electrons). Geometry was simply comprised of 5×5 silicon pixels with a size of $2.5\,\mu\mathrm{m} \times 2.5\,\mu\mathrm{m}$ (same as that of GMAX0505), and their thickness was set to be $5\,\mu\mathrm{m}$ estimated from the detection efficiency derived with a 12.4 keV X-ray beam in BL20B2.[102] We shot 10^7 perfectly polarized photons into the center pixel (the incident position was randomly determined), calculated pulse height distribution for each event, and categorized the events into three types as with our analysis procedure for the experimental data. We note that electric noise and diffusion during carrier collection were ignored in our simulation. MF was derived from the counts of horizontally and vertically striding double-pixel events, and we took the average value of the 10 independent simulation results for each X-ray energy.

Figure 6.7 shows the energy dependence of the MF obtained with both the numerical simulation and experiment. The simulation also indicates a linear increase of the MF as the incident X-ray energy increases within an energy range of 10–30 keV. Whereas the split threshold was aligned to the case of the usual gain, a simulation with the low gain provided the almost same result. The simulation and experimental results are consistent at 12.4 keV, while MF derived from the experiment has smaller values compared with the simulation at 24.8 keV. Notably, while the simulation assumes a flat detection layer and ignores a charge collection process, the internal electric field of GMAX0505 is actually not uniform as shown in Yokoyama et al. (2018),[100] which might be one of the reasons of the difference between these results. Although a more detailed simulation is required to estimate the polarimetric performance more accurately, we demonstrated that GMAX0505 has a significant MF of approximately 10–15% in a 10–20 keV band.

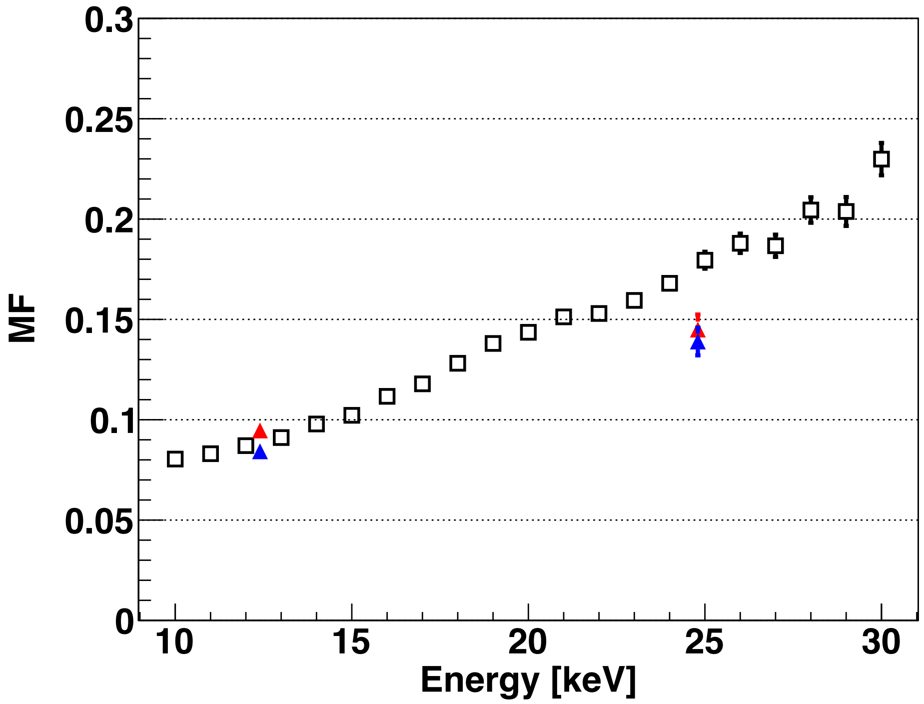

Figure 6.7: Energy dependence of the modulation factor from 10 keV to 30 keV, derived from the (box) numerical simulation and (triangle) experiment. Red and blue plots represent $\mathrm{MF_H}$ and $\mathrm{MF_V}$, respectively.

6.3 Application to MIXIM

6.3.1 Analysis Procedures

In the case of a multiple pinhole mask, imaging polarimetry can be easily performed with double-pixel events; we can derive polarization information in a particular area by using the only double-pixel events detected within the area. On the other hand, MIXIM with a MCA mask has to conduct more complicated analysis, since the detector coordinates does not correspond one-to-one with the sky coordinates due to the encodement. Hence, we need to employ a decoding process including polarization information to realize X-ray polarimetry with a MCA mask.

Figure 6.8 shows a schematic overview of the decoding process with polarization information. It is important that X-ray polarimetry with double-pixel events can detect only Stokes parameters of I and Q, i.e., linear polarization in the horizontal and vertical direction; striding directions have no anisotropy when incident X-rays have a polarization angle of ±45°, which cannot be distinguished with the case of non-polarized X-rays.

Therefore, we decompose a polarization vector for each source grid into the horizontal and vertical direction (i.e., it doubles the element number of a source matrix $\tilde{S}$). In addition, the obtained pattern $\tilde{D}$ has to be comprised of double-pixel events, and also be classified into the horizontally-striding and vertically-striding components to obtain the information of photoelectron trajectories (i.e., $\tilde{D}$ also has the same element number as that of $\tilde{S}$). Thus W, the 5000×5000 response matrix connecting $\tilde{S}$ and $\tilde{D}$, is described as shown in Fig. 6.8; whereas W is basically derived with the same procedures as those explained in section 5.4, we track X-ray photons passing through mask grids for each S_{H} and S_{V}, and fill the transmittance into both D_{H} and D_{V} when it arrives a detector plane. At this time, the distribution ratio between D_{H} and D_{V} is determined by the modulation factor of GMAX0505 acquired from the experiment. Repetition of this process yields 5,000 types of D in total, of which concatenation can be regarded as the response matrix W for imaging polarimetry.

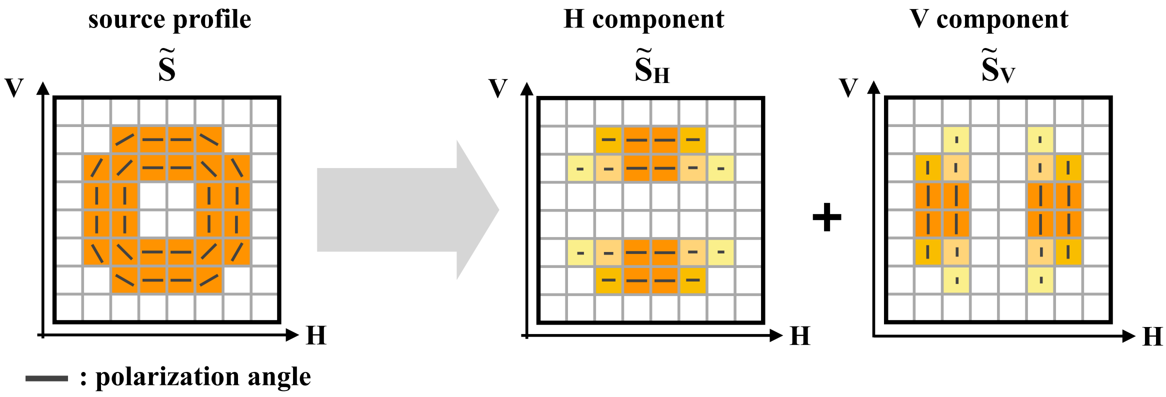

$$\overset{\tilde{\mathrm{D}}}{\begin{pmatrix} \tilde{D}_{H,1} \\ \tilde{D}_{H,2} \\ \vdots \\ \tilde{D}_{V,1} \\ \tilde{D}_{V,2} \\ \vdots \end{pmatrix}} = \overset{\textbf{response matrix W}}{\begin{pmatrix} D_{H,1}(S_{H,1}) & \cdots & D_{H,1}(S_{H,2500}) & D_{H,1}(S_{V,1}) & \cdots & D_{H,1}(S_{V,2500}) \\ \vdots & & \vdots & \vdots & & \vdots \\ D_{H,2500}(S_{H,1}) & \cdots & D_{H,2500}(S_{H,2500}) & D_{H,2500}(S_{V,1}) & \cdots & D_{H,2500}(S_{V,2500}) \\ D_{V,1}(S_{H,1}) & \cdots & D_{V,1}(S_{H,2500}) & D_{V,1}(S_{V,1}) & \cdots & D_{V,1}(S_{V,2500}) \\ \vdots & & \vdots & \vdots & & \vdots \\ D_{V,2500}(S_{H,1}) & \cdots & D_{V,2500}(S_{H,2500}) & D_{V,2500}(S_{V,1}) & \cdots & D_{V,2500}(S_{V,2500}) \end{pmatrix}} \overset{\tilde{\mathrm{S}}}{\begin{pmatrix} \tilde{S}_{H,1} \\ \tilde{S}_{H,2} \\ \vdots \\ \tilde{S}_{V,1} \\ \tilde{S}_{V,2} \\ \vdots \end{pmatrix}}$$

Figure 6.8: Schematic drawing of decomposition of the source profile into two components, and the response matrix for X-ray imaging polarimetry. It additionally includes the information of source polarization vectors and striding directions of photoelectrons.

In order to verify this decoding process, we re-analyzed the experimental data used in section 5.5; we assumed the observation of a single point source (see Fig. 5.9) and two point sources $0.54''$ apart from each other (see $\theta_{\mathrm{H}} = 0.54''$ in Fig. 5.11). From the blended event data, we created two types of folded maps (binned in 25×25 bins): the folded map made with horizontally striding double-pixel events and vertically striding double-pixel events. With the new response matrix, we deciphered these folded maps using EM-algorithm as with the analysis in section 5.4. Although the degree of freedom increases in the case of imaging polarimetry, we used the same equation (Eq. 5.2) in both E-step and M-step, and searched the most probable source profile by repeating these steps (the initial source profile was assumed to be uniform and entirely non-polarized).

6.3.2 Decoding Results

As a consequence of the decoding process explained in the previous section, two patterns of the source profile (horizontal and vertical components) were obtained, as displayed in the top panels of Fig. 6.9 and 6.10. They are normalized by the average counts of all double-pixel events per bin, hence the profile of the horizontal component has much more counts than that of the vertical component due to the horizontally polarized incident X-rays (n.b., the vertical component remains to some extent even if X-rays are perfectly polarized in the horizontal direction, because of the low MF). We also confirmed that the angular resolution of the imaging system is not deteriorated even when we increased the degree of freedom.

From these results, we plot the distribution of an intensity I and polarization degree P, which are given by

$$\left\{ \begin{array}{ll} I & = N_{\mathrm{H}} + N_{\mathrm{V}}, \\ P & = (N_{\mathrm{H}} - N_{\mathrm{V}})/(N_{\mathrm{H}} + N_{\mathrm{V}}), \end{array} \right. \tag{6.4}$$

where N_{H} and N_{V} are the event numbers of the horizontal and vertical components, respectively. The bottom panels of Fig. 6.9 and 6.10 show the results; the obtained source intensity profiles agree with the previous results without the polarimetric information, and the polarization degree for each bin is additionally reconstructed with this analysis technique. The polarization degree ranges from -1 to 1, and its sign corresponds to the polarization direction (positive and negative values represent the horizontal and vertical directions, respectively). Defining source regions as the area depicted as white lines in Fig. 6.9 and 6.10, we also derived the polarization degree for each source region to be 50–70%. These values are significantly lower than the intrinsic polarization degree of the X-ray beam ($\sim$ 100%), which shows that our process could underestimate the polarization degree at present. As one of the possible reasons is that the low MF of the sensor yields less difference between the horizontal and vertical components even with high photon statistics (n.b., the total number of double-pixel events in these data is the order of 10^5). It might be solved by performing imaging polarimetry in a higher energy band, though it causes a decrease of the detection efficiency. Notably, the polarization degree in the area outside the source regions is rather meaningless since it is derived with a few photons appeared as artifacts. While X-ray sources have the same polarization direction in this case, imaging polarimetry of targets with more complex structure and spatially varied polarization vectors would be likely to misestimate the authentic source information. Although we leave them to future work, we should calibrate the response matrix more accurately and develop sophisticated decoding algorithm.

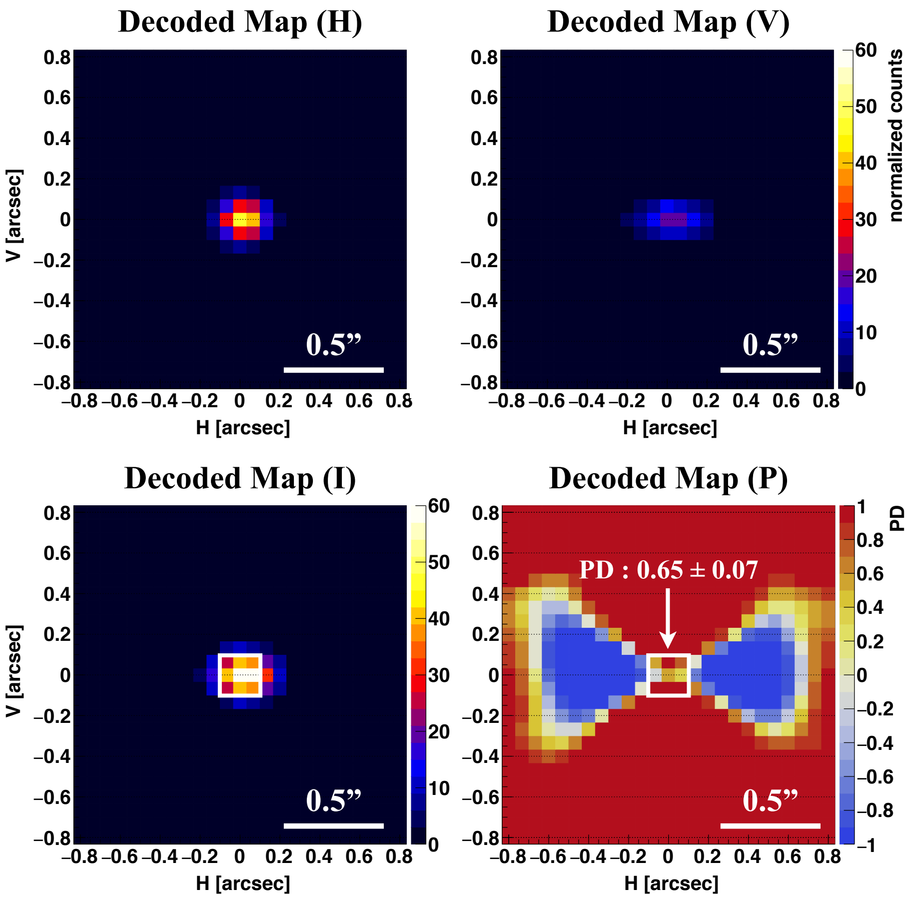

Figure 6.9: (Top) Horizontal (H) and vertical (V) components of the reconstructed source profile with the EM-algorithm. (Bottom) Distribution of the source intensity (I) and polarization degree (P), derived from the top panels.

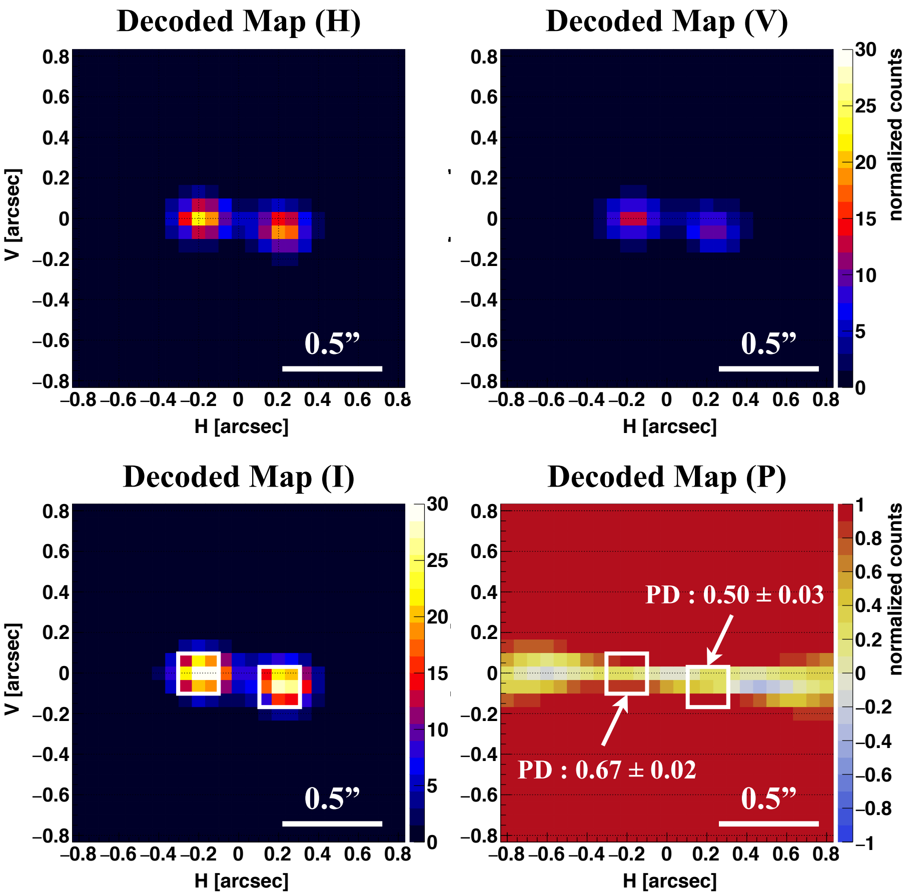

Figure 6.10: Same as Fig. 6.9, but in the case of two point sources 0.54″ apart from each other. White lines denote the source regions defined for calculating the polarization degree.

Chapter 7

Discussion

7.1 Specific Performance

7.1.1 Angular Resolution

Angular resolution, the most remarkable feature of MIXIM, is an increasing function of the system size as with general interferometers. Although X-ray interferometers with a formation flight of multiple satellites would obtain an angular resolution of micro-arcseconds in principle, such large size projects have less feasibility in practice, considering a variety of technical difficulties (as mentioned in section 2.1). In recent years, phase fresnel lenses (PFLs) have also been developed as practical approaches for high resolution X-ray imaging. PFLs are optics with both high angular resolution and high efficiency whereas they are for monochromatic X-ray imaging. In fact, Krizmanic et al. (2020) reported that they succeeded in achieving an angular resolution of 20 milli-arcseconds at 8 keV, with 3 mm diameter PFL produced by Micro-ElectroMechanical Systems (MEMS) fabrication techniques.[121] However, its focal length was $\sim 100\,\mathrm{m}$ even for a small diameter, which also makes a decrease of the system size difficult. Besides, MIXIM is a scalable imaging system and can maintain moderately high angular resolution even with the small system size, as demonstrated in the experiments; a small prototype MIXIM with a system size of $\sim 1\,\mathrm{m}$ achieved an high angular resolution of $\sim 0.5''$, or MIXIM can be configured to an even smaller size (e.g., a 6U CubeSat) for an increase of feasibility, in return for some deterioration of the angular resolution. We should note that a detector with a high spatial resolution can be beneficial also for other proposed X-ray interferometers;[122] e.g., employing such a detector can reduce the size of the 100 m-long *MAXIM* prototype,[49] though the developer team has to resolve the inherent problem of fringe spacing.

MIXIM, being a scalable imaging system, can be scaled up to a size of a large satellite or larger, in order to increase the angular resolution (its scalable mission plans are also discussed in Hayashida et al. 2020[123]). In our estimate, MIXIM with a distance of $z = 100\,\mathrm{m}$ is expected to have an angular resolution of $0.01''$ for 12.4 keV with $d \sim 70\,\mathrm{\mu m}$ and $f = 0.1$ ($m = 2$). Notably, the adoption of higher m enhances the angular resolution for the same slits and wavelength, though it also elongates the distance and a high energy resolution will be crucial to maintain the imaging performance, as our estimate in section 3.2 shows. In particular, an important advantage of MIXIM is potential use in a higher-energy X-ray band; whereas such high-energy X-rays are difficult to focus with conventional X-ray mirrors, MIXIM is well capable of obtaining high-resolution imaging in such a high-energy band by employing fine-pitch masks with thick absorbers and a detector with a high spatial resolution and high detection efficiency.

7.1.2 Field of View

Whether we adopted a multi-pinhole or MCA mask, MIXIM has an inherently narrow FOV (approximately dz^{-1}). In particular, not only a small d but also the wrap-around effect constrains the FOV of MIXIM; this effect increases the background level in the case that other X-ray sources reside outsize the FOV or when an observational target has a more extended structure than the FOV. It implies that only shifting the pointing direction to scan the sky cannot solve the problem. Thus, MIXIM's observational targets should be almost point-like at a wavelength of interest. Notably, an increase of the pitch d practically leads to an even narrower FOV, since it also needs the extension of the distance z to maintain the X-ray interferometry with the same m according to Eq. 3.1 ($z \propto d^2$). Hence, to achieve simultaneously a high angular resolution and wide FOV, the system size and opening fraction are both required to be reduced, which results in an accordingly reduced effective area of MIXIM.

7.1.3 Effective Area

Effective area is basically determined by the transmittance of a mask, the imaging area and detection efficiency of a sensor. The transmittance can increase to $\sim 50\%$ at most with the employment of a MCA mask as demonstrated in section 5.6, and this value would be nearly unchanged regardless of the mission scale of MIXIM. On the other hand, imaging area is directly linked to the mission scale; it can be enhanced by employing multiple sensors, though a spacecraft bus size limits the capacity especially in the case of a nano-satellite or micro-satellite. The current system with GMAX0505 has an imaging area of $1.64\,\mathrm{cm}^2$, and its detection efficiency is 10.5% and 1.9% at 5.9 keV and 12.4 keV, respectively, which means that the effective area per sensor is estimated to be $\sim 0.1\,\mathrm{cm}^2$

even at 5.9 keV. It should be noted that these values are derived with all event types including extended events, whereas the actual detection efficiency gets lower when we perform X-ray imaging polarimetry with double-pixel events. Although it is quite low in comparison with existing X-ray observatories with effective areas of hundreds or thousands of cm^2, MIXIM actually does not require such large effective area since only bright X-ray sources should be observational targets due to its background-limited sensitivity (mentioned in section 7.2). In addition, GMAX0505, is not originally optimized for high-resolution X-ray imaging; we should employ a semiconductor detector with both high spatial resolution and effective area in the future.

7.1.4 Polarimetric Sensitivity

If we employ GMAX0505 as the detector of MIXIM, MIXIM would be able to perform X-ray imaging polarimetry in a 10–20 keV band, where X-ray polarimeters launched so far cannot cover as mentioned in section 2.2. Polarimetric measurement in this energy band is important because it can avoid the contamination of unpolarized thermal X-rays with temperature of few keV, and obtain relatively high photon statistics compared with the observation above 20 keV. Whereas a fine-pixel CMOS sensor such as GMAX0505 has a unique observable energy band, its modulation factor is relatively lower even at 24.8 keV than any other existing X-ray polarimeters; the gas pixel detectors onboard IXPE have a modulation factor of 20–65% in 2–8 keV,[80] and Compton scattering type polarimeters typically have a modulation factor of 30–50% in hard X-ray and soft Gamma-ray bands.[72,124]

Notably, the high spatial resolution could compensate the low modulation factor, in combination with high-performance optics. Even though the accumulated polarization degree in the entire source region is not so high, partial regions resolved with high angular resolution would yield highly polarized signals (e.g., torus-like structure surrounding a primary X-ray source entirely shows no polarization in the case of a face-on view, each region has a polarization vector in the tangential direction.) A fine-pixel CMOS sensor is especially suitable for observation of such an X-ray source with spatially complicated reflectors. We also note that such polarimetric measurement for each partial region needs much more X-ray photons to detect a significant polarization. With our current analysis procedures, only double-pixel events are used for imaging polarimetry, which leads to a decrease of effective area. Hence, we should embrace extended events in our polarimetric analyses, especially around 20 keV where an extend event ratio exceeds 50% (see Fig. 6.4).

7.1.5 Attitude Determination and Control

In order to achieve high-resolution imaging, an imaging system has to be equipped with a high-precision aspect determination system (the determination uncertainty should be less than the angular resolution of the imaging system to make the best of its performance). In the case of *Chandra*, its star tracker (STT) comprised of a 11.2 cm optical telescope and two CCD detectors was installed at HRMA to measure the spacecraft aspect by observing bright guide stars (the spread of image reconstruction was required to be $0.5''$).[125] This STT, manufactured by Ball Aerospace, has the highest performance among those onboard existing X-ray observatories, while its large size (the telescope has a focal length of 990 mm) and high-cost is not suitable for small-scale missions such as the prototype of MIXIM (n.b., Ball Aerospace has newly developed the CT-2020, a low-cost commercial star tracker with a size of ~ 30 cm and a precision of $< 1.5''$). On the other hand, a variety of compact STTs for nano-satellites and micro-satellites are commercially available in recent years, though their typical precisions of a few arcseconds are insufficient for X-ray imaging with sub-arcseconds (or even more higher) angular resolution.

Whereas the performance of current commercial STTs limits the angular resolution of MIXIM at present, a high-precision aspect determination system has been actively developed since it is required for not only high-resolution X-ray imaging but also a number of missions in a broad range of fields. For example, ASTERIA, a 6U CubeSat mission for the demonstration of high-precision space-based photometry, was launched in 2017, and achieved a pointing stability of $0.5''$ (RMS) over 20 minutes in orbit even with its small mass.[126] Whereas its key technologies were thermal and pointing stability with an accurate piezoelectric stage, it also demonstrates that the aspect could be accurately determined with the well-developed imaging system and software of ASTERIA. Hence, it is not technically unfeasible to deploy MIXIM on nano-satellites at least in terms of attitude determination. Notably, high-precision pointing control is not absolutely necessary for achieving high-resolution imaging, if with a high-precision aspect determination system; we can correct the sky coordinates of obtained images according to the spacecraft aspect information, whereas unstable observation would result in a decrease of effective exposure time since a target frequently disappears from its narrow field of view.

7.2 Future Plan for Astronomical Observation

7.2.1 Background

If we apply MIXIM to X-ray astronomical observations, background effects are crucial problem since MIXIM does not have a focusing capability, which results in a decrease of signal-to-noise ratio compared with focusing optics. Although MIXIM only uses X-ray events within an energy band of interest and filters out other events, some background components are inevitably included and contaminate or misestimate the authentic image of an observational target. In particular, cosmic X-ray background (CXB) and non X-ray background (NXB) have to be considered, regardless of the type of observational targets.

CXB, the integrated X-ray emission of unresolved AGNs, is uniformly distributed over the sky, which means that this background component intrudes into a sensor from outside of the FOV of MIXIM, and strongly contaminates an image as the wrap-around effect in the case of a simple configuration with only a mask and sensor. Hence, MIXIM requires an additional parallel hole collimator to block X-rays coming from the outside of the FOV such as CXB; if we install a mask (a multi-pinhole mask or a MCA mask) onto a collimator with a length of 120 cm and a hole size of 1 cm (as shown in Fig. 7.1), X-rays with incident angles of more than 1° are blocked, which considerably reduces the intrusion of CXB. The spectrum of CXB is approximated to be a power-law with a photon index of 1.4 and a normalization of $\sim 10.7\,\mathrm{photons\,s^{-1}\,cm^{-2}\,keV^{-1}}$.[127] Given that we employ a system with the aforementioned collimator, the photon flux of CXB is estimated to be $3.5 \times 10^{-5}\,\mathrm{cts\,s^{-1}\,cm^{-2}}$ in a iron K-shell (Fe K) band (6.3–6.5 keV) and $9.3 \times 10^{-5}\,\mathrm{cts\,s^{-1}\,cm^{-2}}$ in a 9.5–10.5 keV band ($\Delta E/E = \pm 5\%$ at 10 keV). If other X-ray sources with incident angles of less than 1° reside in the sky, their X-ray events cannot also be eliminated. Thus we should take into account such additional background especially when we observe e.g., AGNs.

On the other hand, NXB is mainly ascribed to charged particles entering a detector from a variety of directions. While CXB can be estimated from the observational results of other X-ray observatories, accurate estimation of NXB is more difficult since it depends on the altitude of an orbit and the configuration of an instrument. The Earth's magnetic fields prevent low energy particles to enter the instrument if with a low Earth orbit with an altitude of ~ 550 km (e.g., *Suzaku*), whereas such particles would increase the background level in the case of a highly elliptical orbit such as *XMM-Newton*.[128] Even XIS onboard *Suzaku* cannot perfectly remove NXB as shown in the night Earth spectra (see Koyama et al. 2007[129]), from which the NXB level of FI CCDs was derived to be $1.4 \times 10^{-2}\,\mathrm{cts\,s^{-1}\,cm^{-2}}$ in a 0.5–10 keV band. Notably, NXB has been subtracted from

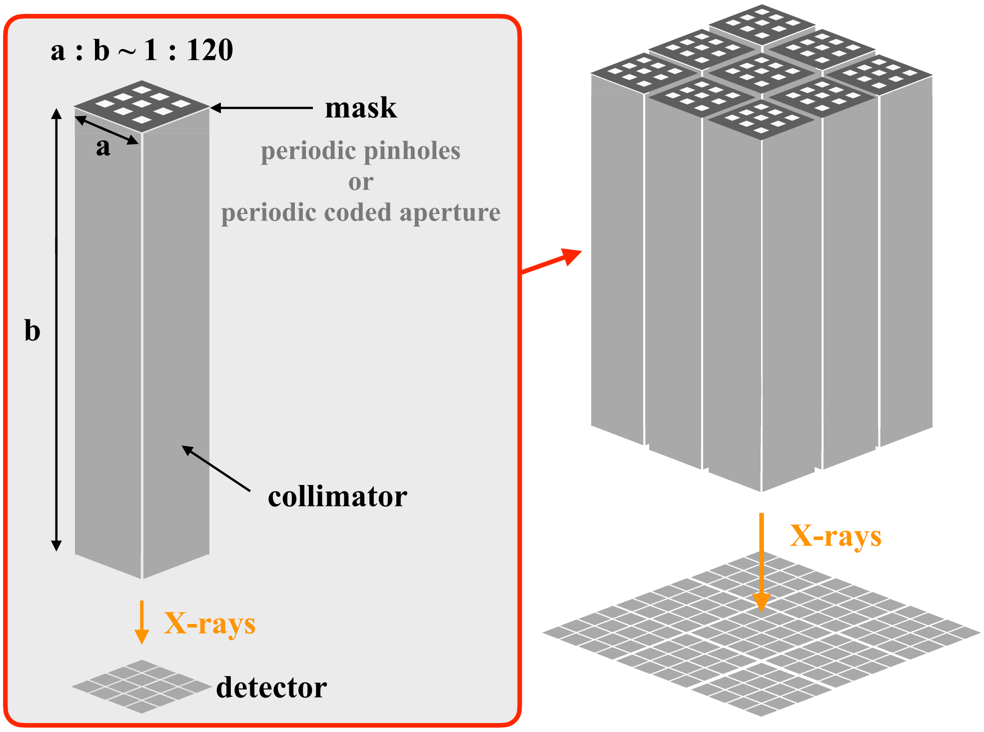

Figure 7.1: Schematic illustration of MIXIM with collimators to block off-axis X-rays. This aspect ratio can block X-rays with incident angles of more than 1°.

these spectra to some extent with event grade selection; this technique has been widely applied with X-ray CCDs onboard recent X-ray observatories (including XIS). Assuming that the NXB has a constant spectrum (excluding fluorescent lines) and its normalization is linearly dependent of the volume of a detection layer, the NXB level of GMAX0505 is estimated to be $2.1 \times 10^{-5}\,\mathrm{cts\,s^{-1}\,cm^{-2}}$ in a 6.3–6.5 keV band. We also note that a sensor with a pixel size of a few µm would furthermore reduce the NXB level compared with X-ray CCDs since its high spatial resolution enhances the capability to distinguish charged particle events and X-ray events by resolving their trajectories, though it also necessitates a thick detection layer which leads to an increase of the detector volume. In addition, the installation of active shields such as Hard X-ray Detector onboard *Suzaku* might be also effective to reduce the NXB especially when we perform high-resolution imaging in a hard X-ray band.

7.2.2 Observational Targets

As mentioned in Uttley et al. (2021),[1] high-resolution X-ray imaging would enable us to reveal a wide range of astrophysical questions; Figure 7.2 shows typical X-ray sources with the distances and expected angular sizes as the horizontal and vertical axes, respectively. It includes not only nearby galactic sources such as X-ray binaries (XRBs), stars and exoplanets, but also extragalactic supermassive black holes (SMBHs). Observation of XRBs with an angular resolution higher than milli-arcseconds could directly obtain the binary system parameters (e.g., their orbits), which is important to determine the physical properties of both compact objects and companion stars. In addition, X-ray emitting jets seen in some XRBs are also interesting targets, which gives a clue to understand the unsolved mechanism of the jets. In the case of nearby stars, the feasibility of observation increases since their angular diameters are typically larger than the orbits of XRBs. Whereas spatially-resolved images of stellar coronae are obtained only for the Sun so far, high-resolution X-ray imaging of nearby stars facilitates the statistical study of stellar coronal structure. Notably, if an observed star has planets and some of them transit the stellar disc, planets could be detected as an absorption feature in the spatially resolved X-ray image. Even for SMBHs with a distance of over a few Mpc, high-resolution X-ray imaging plays an important role; active galactic nucleus (AGN), which hosts a SMBH in the center, has complicated structure mainly comprised of the accretion disk, X-ray corona, broad line region (BLR), narrow line region (NLR) and obscuring torus. Although its geometry has been built up from spectroscopic, photometric and polarimetric observations and partially resolved with recent interferometers in radio and infrared bands (e.g., ALMA, VLTI), the entire structure (especially in the central region) has not yet been fully understood. Whereas direct imaging in an X-ray band would be powerful diagnostic tool to investigate the X-ray emitting central region, it is difficult for existing X-ray observatories including *Chandra* to resolve such structure even for nearby AGNs. Thus X-ray observation with much higher angular resolution has been required for complete understanding of the whole system of AGNs. Such observation could also result in the discovery of binary SMBHs which provides us crucial information about galaxy mergers.

However, observable targets for MIXIM are actually limited in terms of the FOV and sensitivity; they should be brighter than $\sim 1\,\mathrm{mCrab}$ and almost point-like at a wavelength of interest to obtain an explicit X-ray source profile. In fact, observation of dim X-ray sources is also difficult for other X-ray interferometers without focusing optics since their effective areas are low especially in a hard X-ray band, but they have moderate FOVs if with a various length of baselines as distinct from MIXIM. Hence, we propose specific some observational targets for MIXIM, considering its features and limitation.

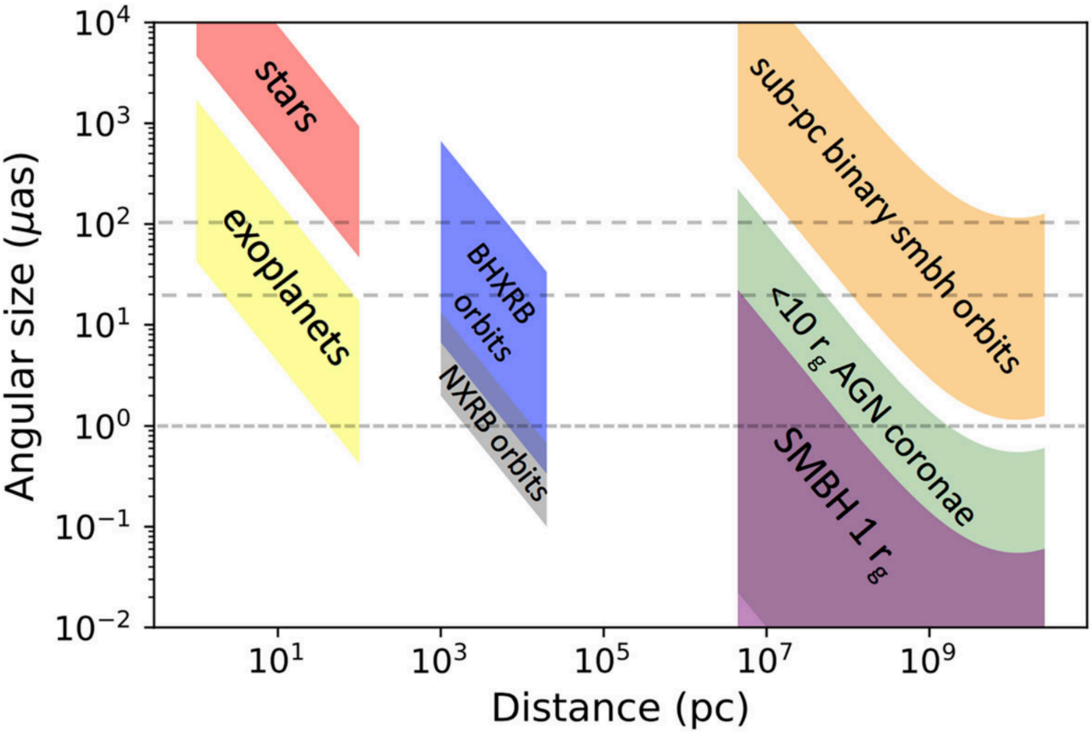

Figure 7.2: Summary plot of the observational targets of high-resolution X-ray imaging, with the distances and expected angular sizes as the horizontal and vertical axes, respectively (Fig. 1 in Uttley et al. 2021[1]).

Obscuring Tori of Nearby AGNs

One of the most promising targets for MIXIM is a nearby Compton-thick AGN, of which the central SMBH is heavily obscured by a thick torus. *Chandra* has already found spatially extended Fe K emission from some Compton-thick AGNs, such as e.g., the Circinus galaxy[130] and NGC 1068.[131] In recent years, Jones et al. (2021) systematically analyzed the *Chandra* observation data of Compton-thick AGNs and summarized their properties.[132] Although they gave clues to grasp the geometry of AGN tori, the detailed structure of and within the tori cannot be resolved with the current X-ray observatories, even for nearby AGNs with a distance of a few Mpc. It should be noted that observations with radio or infrared interferometers succeeded in obtaining images with higher angular resolutions than 0.5″,[133–135] though their results only show not the entire structure but certain aspects (such as temperature and density) of AGNs. In contrast, high-resolution imaging of such AGNs in Fe K band would directly provide the overall distribution of neutral gas and dust, thanks to the high transmittance of X-rays.

If we observe Fe K emission from the Circinus galaxy (one of the nearest Seyfert galaxies with a distance of 4.2 Mpc), its strong Fe Kα emission flux was obtained to be $2.14 \pm 0.06 \times 10^{-4}\,\mathrm{cts\,s^{-1}\,cm^{-2}}$ from an observation with *XMM-Newton*.[136] *Chandra* observations revealed that about 50% of the Fe Kα emission is distributed within the central region with a radius of 10 pc (an image in a Fe Kα band and spectra of the central and surrounding regions are shown in Fig. 7.3), and its velocity width of $\sim 1700\,\mathrm{km\,s^{-1}}$ suggests that the neutral iron resides in the optical broad line region (i.e., $\sim 10^{-3}$ pc).[137] However, it still has some ambiguity in determining the specific neutral iron distribution within the spatially-unresolved central region. If MIXIM deployed on a single satellite (~ 10 m) observes the Circinus galaxy with an angular resolution of $0.05''$, it would have a potential to resolve the pc-scale structure, and directly distinguish whether the Fe K emission is concentrated within the inner 1 pc or not. (n.b., the significant detection might be difficult due to the background component when the Fe K emission has an extended profile). In this case, an effective area of $\sim 10\,\mathrm{cm^2}$ is required to acquire 10^3 photons in total within an effective exposure time of 1 Ms. High-resolution imaging polarimetry of reflected X-rays from the torus or circumnuclear disk would also be useful to investigate their geometry, though even the Circinus galaxy has X-ray flux of $8 \times 10^5\,\mathrm{cts\,s^{-1}\,cm^{-2}}$ in a 9.5–10.5 keV band where the reflection component would be dominant. It is comparable to the CXB flux in the same energy band, which implies that it is quite difficult to obtain the reflected X-ray profile even for just imaging. Other nearby AGNs such as e.g., NGC 1068, NGC 4945, and Mrk 3 also have a Fe K emission line, though observations of these targets would also be difficult since its flux in the Fe K band is lower than that of the Circinus galaxy.

Jet Structure of XRBs and AGNs

Relativistic jets launched from XRBs and AGNs are also interesting targets for MIXIM in terms of the study of their evolution and mechanism in detail. For some micro-quasars with relatively large scale jets, spatially-resolved X-ray observation produced intriguing results; *Chandra* detected moving X-ray emission associated with an X-ray flare from the jet regions of XTE J1550-564, which provided the evidence of the gradual deceleration of the jet.[138] In addition, doppler-shifted iron lines were detected from the jet regions of SS 433, which demonstrates the reheating of the jet component.[139] One of the nearest quasar 3C 273 also has the bright jet with an angular extent of ~ 10 arcsec.[140] However, these targets whose global jet structure has already been resolved by *Chandra* are too diffused for MIXIM.

Besides, some bright XRBs show jet features in multi-wavelength observations, even though *Chandra* cannot obtain their spatial structure. Cyg X-1, a very bright black hole

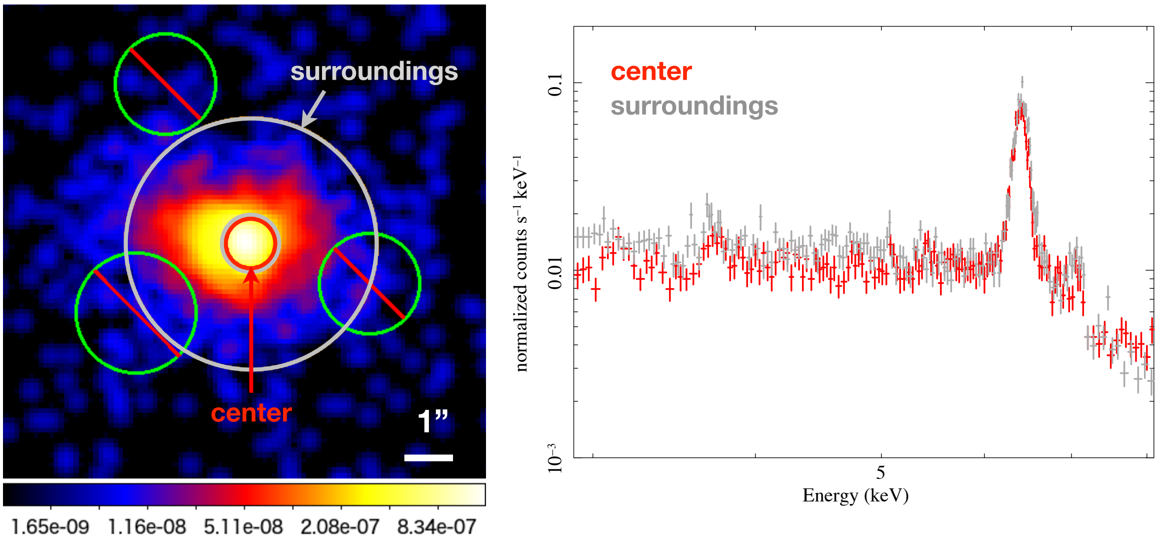

Figure 7.3: (left) Flux image in a Fe Kα band of the Circinus galaxy obtained with *Chandra*. (right) Background-subtracted spectra within the (red) central and (gray) surrounding regions. These regions have the almost same Fe Kα flux.

XRB, has been observed in a wide energy range from radio to Gamma-rays; its jet structure was clearly resolved by the recent observations with the Very Long Baseline Array (VLBA) at 8.4 GHz,[141] and GeV emission associated with the jet was also detected (only in the hard state) from *Fermi* observations.[142] Multiple X-ray observations with *Suzaku* indicate that the main spectral components of Cyg X-1 in an X-ray band are emission from the accretion disk and hot corona,[143] and the recent lepto-hadronic model for the broad-band spectral energy distribution of Cyg X-1 also suggests that the contribution of the jet emission would be less than 5% in an X-ray band.[144] However, since the total flux of Cyg X-1 is $1 \times 10^{-8}\,\mathrm{erg\,cm^{-2}\,s^{-1}}$ in a 10–50 keV band (n.b., in a hard state),[145] even a few percent of the flux would be about 100 times higher than the estimated CXB level in a 9.5–10.5 keV band. Given that the jet in an X-ray band has also the spatial extent of ~ 10 milli-arcseconds as with that in a radio band, MIXIM would resolve its spatial structure if with an angular resolution of a few milli-arcseconds. Whereas such a high angular resolution has not yet been demonstrated so far, we could improve the current maximum angular resolution of $\sim 0.05''$ at $z \sim 9$ m by decreasing the sizes of both the detector pixel and mask aperture element with the same z, or extending z with e.g., the employment of free flyer satellites. Notably, simultaneous observation with masks with different pitches provides the Cyg X-1 profiles in several energy bands, which substantially represents the X-ray spectrum for each region. Whereas it is difficult to accurately separate the jet and corona components from only spectroscopic information in a featureless X-ray band, MIXIM has a potential to directly resolve the degeneracy of these components with its imaging capability, and contribute to the understanding of the jet mechanism.

Stellar Coronae and Flares

Nearby stars bright in an X-ray band such as e.g., Capella, Algol, UX Ari and HR 1099 would be also observable for MIXIM. Capella, the brightest stellar X-ray source on the average among them (mainly consisting of two cool giant stars), has a variety of coronal emission lines as shown in the spectrum obtained with *Chandra*.[146] The observed Fe XVII line flux (in a 0.68–0.78 keV band) of $\sim 7 \times 10^{-3}\,\mathrm{cts\,cm^{-2}\,s^{-1}}$ is an order of magnitude higher than the estimated CXB level in the same band, which represents that it would be used as the tracer of the X-ray coronal activity. However, since the angular sizes of the giant stars are a few milli-arcseconds even with a distance of only $\sim 13\,\mathrm{pc}$,[147] a sub-milliarcseconds angular resolution would be required to investigate the detailed coronal structure. Algol, UX Ari and HR 1099 (RS CVn stars) are also famous for their giant flares,[148–150] and previous studies suggest that the flare loop sizes would be comparable with the entire binary systems. Thus, high-resolution X-ray imaging might directly capture the evolution of flare loops if with such large flares during observations.

Notably, the Sun, the brightest X-ray source in the sky, is also an interesting observational target. As distinct from the aforementioned stars, past observations have already obtained clear X-ray images in the case of the Sun; X-Ray Telescope onboard Hinode[151] provides an angular resolution of $\sim 1''$ in a soft X-ray band, and Hard X-ray Telescope onboard Yohkoh[152] supplied hard X-ray images with an angular resolution of $\sim 5''$. Whereas MIXIM is not suitable for soft X-ray observations of the solar corona due to its too large angular size, hard X-ray polarimetric imaging of large solar flares with MIXIM might be beneficial to investigate the particle acceleration mechanism.

Chapter 8

Summary

In order to realize unprecedentedly high-resolution X-ray imaging, we have developed MIXIM: a novel X-ray imaging system comprised of a mask and an X-ray detector. In the case of a simple pinhole camera, an increase of the mask-detector distance or a decrease of the aperture size improves the angular resolution to some extent, though the improvement has a serious limit due to a diffraction effect. Hence, for circumventing the diffraction problem, we apply to MIXIM the Talbot effect: an interference phenomenon that a mask with equally-spaced apertures forms a self-image for a monochromatic parallel light. It enables MIXIM to overcome the limitation, and conduct imaging with a very high angular resolution for a single wavelength. Its performance is higher than any other existing X-ray observatories even with a system size of $\sim 50\,\mathrm{cm}$ at 12.4 keV in principle.

Therefore, we employed a mask with equally-spaced apertures and performed proof-of-concept experiments of MIXIM at SPring-8 BL20B2. One of the key components is GMAX0505, a CMOS sensor with a higher spatial resolution than those of the sensors we used so far. With this sensor and a grating with a pitch of 9.6 µm, we succeeded in performing 1D-imaging with an angular resolution of $0.5''$ at 12.4 keV with only a system size of $< 1\,\mathrm{m}$, which surpasses the results of the previous experiments. Furthermore, we also obtained 2D images with a multiple pinhole mask, for the first time with MIXIM. The highest angular resolution achieved in our experiments is estimated to be $\sim 0.05''$ with a mask-detector distance of 866.5 cm, which demonstrated the powerful performance and high scalability of MIXIM.

In addition, we newly adopted MCA masks to improve the low effective area of MIXIM. Whereas they have complicated aperture patterns, our experiment demonstrated that the MCA masks surely form self-images in an X-ray band and they can be applied to MIXIM. Since obtained images are the convolution of an X-ray source profile and a mask aperture pattern, decoding process is required to reconstruct the original source profile. Our decoding process with EM algorithm successfully deciphered the obtained images, even in the case that the X-ray source has a complex pattern or limited photon statistics. While the system with the novel masks maintained compactness and high angular resolution, its effective area increased about 25 times compared with that with a multiple pinhole mask.

MIXIM also has a potential to perform X-ray imaging polarimetry in an unexploited 10–20 keV band, because its fine-pixel CMOS sensor can measure the emission direction of a photoelectron of which distribution depends on the polarization direction of an incident X-ray photon. The performance of GMAX0505 as an X-ray polarimeter was evaluated with a highly polarized X-ray beam at SPring-8 BL20B2, and its modulation factor was derived to be 9.47% and 14.5% at 12.4 keV and 24.8 keV, respectively. Although these values are lower than existing X-ray and Gamma-ray polarimeters, this capability would be beneficial in association with the high-resolution imaging performance.

As a consequence, these proof-of-concept experiments verified that MIXIM has high imaging performance even with its compact size, which is a great advantage in terms of the feasibility of the actual deployment on a satellite. Notably, its specific configuration should be optimized according to observational targets since the size of MIXIM is adjustable. As interferometers have explored new fields in a variety of wavelengths, MIXIM would reveal the unresolved fine spatial structures of a variety of X-ray sources in the future.

Acknowledgments

First of all, I would like to express my gratitude to the great support by the members of the X-ray astrophysics group in Osaka University; Dr. Kiyoshi Hayashida has always provided guidance for me as the deviser and leader of MIXIM, even when he was laid up with illness. The results described in this thesis would not have been obtained without his assistance and advices throughout my study life. I extend my heartfelt condolence to him, and pray that his soul may rest in peace. Prof. Hironori Matsumoto, my supervisor, taught me not only helpful advices about this thesis but also fundamental physics and logicality, which must be useful from now on whatever I work on. His explicit instructions and explanation frequently guided me when I was in trouble. Dr. Hirofumi Noda also supported my various studies including the development of MIXIM. In particular, experiments with Soft X-ray Imager (SXI) onboard *XRISM* with him were a precious experience. He is a role model as a young researcher for me since his enthusiasm for studies always encourages me. I am also grateful to Prof. Emer. Hiroshi Tsunemi, Dr. Hiroshi Nakajima and Dr. Hirokazu Odaka for a lot of helpful comments and discussions about the experimental results, and thank all graduate students who cooperated with the proof-of-concept experiments of MIXIM.

I would also like to show my appreciation to my external collaborators; Dr. Toru Tamagawa, Chief Scientist at RIKEN, gave valuable comments as a reviewer of this thesis, and introduced me to a working group of *IXPE*, from which I learned a lot about X-ray imaging polarimetry. In addition, I wish to extend my gratitude to beamline scientists at SPring-8 for their support with the experiments, and all the member of the SXI team since I had a very good experience as an experimental astrophysicist. Finally, I would like to thank my parents for their kind supports during my graduate student life.

References

[1] P. Uttley, R. d. Hartog, C. Bambi, et al. The high energy universe at ultra-high resolution: the power and promise of x-ray interferometry. *Experimental Astronomy*, Vol. 51, No. 3, pp. 1081–1107, 2021.

[2] T. Chattopadhyay. Hard X-ray polarimetry—an overview of the method, science drivers, and recent findings. *Journal of Astrophysics and Astronomy*, Vol. 42, No. 2, p. 106, 2021.

[3] W. Forman, C. Jones, L. Cominsky, et al. The fourth Uhuru catalog of X-ray sources. *Astrophysical Journal, Supplement*, Vol. 38, pp. 357–412, 1978.

[4] S. S. Holt. Temporal X-Ray Astronomy with a Pinhole Camera. *Astrophysics and Space Science*, Vol. 42, No. 1, pp. 123–141, 1976.

[5] E. Caroli, J. B. Stephen, G. Di Cocco, et al. Coded Aperture Imaging in X-Ray and Gamma-Ray Astronomy. *Space Science Reviews*, Vol. 45, No. 3-4, pp. 349–403, 1987.

[6] R. L. Blake, A. J. Burek, E. Fenimore, et al. Solar x-ray photography with multiplex pin-hole camera. *Review of Scientific Instruments*, Vol. 45, No. 4, pp. 513–516, 1974.

[7] Y. Tanaka, M. Fujii, H. Inoue, et al. X-ray astronomy satellite Tenma. *Publications of the Astronomical Society of Japan*, Vol. 36, No. 4, pp. 641–658, 1984.

[8] S. D. Barthelmy, L. M. Barbier, J. R. Cummings, et al. The Burst Alert Telescope (BAT) on the SWIFT Midex Mission. *Space Science Reviews*, Vol. 120, No. 3-4, pp. 143–164, 2005.

[9] P. Ubertini, F. Lebrun, G. Di Cocco, et al. IBIS: The Imager on-board INTEGRAL. *Astronomy and Astrophysics*, Vol. 411, pp. L131–L139, 2003.

[10] R. Giacconi, G. Branduardi, U. Briel, et al. The Einstein (HEAO 2) X-ray Observatory. *Astrophysical Journal*, Vol. 230, pp. 540–550, 1979.

[11] I. M. Gioia, T. Maccacaro, R. E. Schild, et al. The Einstein Observatory Extended Medium-Sensitivity Survey. I. X-Ray Data and Analysis. *Astrophysical Journal, Supplement*, Vol. 72, p. 567, 1990.

[12] F. D. Seward. Einstein Observations of Galactic Supernova Remnants. *Astrophysical Journal, Supplement*, Vol. 73, p. 781, 1990.

[13] J. Truemper. The ROSAT mission. *Advances in Space Research*, Vol. 2, No. 4, pp. 241–249, 1982.

[14] M. V. Zombeck, L. P. David, F. R. H. Jr., et al. Orbital performance of the high-resolution imager (HRI) on ROSAT. *EUV, X-Ray, and Gamma-Ray Instrumentation for Astronomy VI*, Vol. 2518, pp. 304 – 321. International Society for Optics and Photonics, SPIE, 1995.

[15] W. Voges, B. Aschenbach, T. Boller, et al. The ROSAT all-sky survey bright source catalogue. *Astronomy and Astrophysics*, Vol. 349, pp. 389–405, 1999.

[16] M. C. Weisskopf, H. D. Tananbaum, and others. *Chandra X-ray Observatory (CXO): overview*, Vol. 4012 of *Society of Photo-Optical Instrumentation Engineers (SPIE) Conference Series*, pp. 2–16. 2000.

[17] M. C. Weisskopf, B. Brinkman, C. Canizares, et al. An overview of the performance and scientific results from the chandra x-ray observatory. *Publications of the Astronomical Society of the Pacific*, Vol. 114, No. 791, p. 1, 2002.

[18] S. S. Murray, G. K. Austin, J. H. Chappell, et al. In-flight performance of the Chandra high-resolution camera. *X-Ray Optics, Instruments, and Missions III*, Vol. 4012 of *Society of Photo-Optical Instrumentation Engineers (SPIE) Conference Series*, pp. 68–80, 2000.

[19] G. P. Garmire, M. W. Bautz, P. G. Ford, et al. Advanced CCD imaging spectrometer (ACIS) instrument on the Chandra X-ray Observatory. *X-Ray and Gamma-Ray Telescopes and Instruments for Astronomy.*, Vol. 4851 of *Society of Photo-Optical Instrumentation Engineers (SPIE) Conference Series*, pp. 28–44, 2003.

[20] H. Tananbaum, M. C. Weisskopf, W. Tucker, et al. Highlights and discoveries from the Chandra X-ray Observatory. *Reports on Progress in Physics*, Vol. 77, No. 6, p. 066902, 2014.

[21] K. Mitsuda, M. Bautz, H. Inoue, et al. The X-Ray Observatory Suzaku. *Publications of the Astronomical Society of Japan*, Vol. 59, pp. S1–S7, 2007.

[22] T. Takahashi, M. Kokubun, K. Mitsuda, et al. Hitomi (ASTRO-H) X-ray Astronomy Satellite. *Journal of Astronomical Telescopes, Instruments, and Systems*, Vol. 4, No. 2, pp. 1 – 13, 2018.

[23] P. J. Serlemitsos, Y. Soong, K.-W. Chan, et al. The X-Ray Telescope onboard Suzaku. *Publications of the Astronomical Society of Japan*, Vol. 59, No. sp1, pp. S9–S21, 2007.

[24] F. Jansen, D. Lumb, B. Altieri, et al. XMM-Newton observatory. I. The spacecraft and operations. *Astronomy and Astrophysics*, Vol. 365, pp. L1–L6, 2001.

[25] R. Sunyaev, V. Arefiev, V. Babyshkin, et al. SRG X-ray orbital observatory. Its telescopes and first scientific results. *Astronomy and Astrophysics*, Vol. 656, p. A132, 2021.

[26] P. Predehl, R. Andritschke, V. Arefiev, et al. The eROSITA X-ray telescope on SRG. *Astronomy and Astrophysics*, Vol. 647, p. A1, 2021.

[27] S. L. O'Dell, T. L. Aldcroft, C. Atkins, et al. Toward active x-ray telescopes II. *Adaptive X-Ray Optics II*, Vol. 8503 of *Society of Photo-Optical Instrumentation Engineers (SPIE) Conference Series*, p. 850307, 2012.

[28] R. M. Prestage. The Green Bank Telescope. *Ground-based and Airborne Telescopes*, Vol. 6267, p. 626712. International Society for Optics and Photonics, SPIE, 2006.

[29] A. A. Michelson and F. G. Pease. Measurement of the Diameter of α Orionis with the Interferometer. *Astrophysical Journal*, Vol. 53, pp. 249–259, 1921.

[30] R. Hanbury Brown, J. Davis, and L. R. Allen. The stellar interferometer at Narrabri Observatory I. A. description of the instrument and the observational procedure. *Monthly Notices of the RAS*, Vol. 137, p. 375, 1967.

[31] R. Hanbury Brown, J. Davis, and L. R. Allen. The Angular Diameters of 32 Stars. *Monthly Notices of the RAS*, Vol. 167, pp. 121–136, 1974.

[32] J. L. Pawsey. Observation of Million Degree Thermal Radiation from the Sun at a Wavelength of 1.5 Metres. *Nature*, Vol. 158, No. 4018, pp. 633–634, 1946.

[33] M. Ryle and D. D. Vonberg. Solar Radiation on 175 Mc./s. *Nature*, Vol. 158, No. 4010, pp. 339–340, 1946.

[34] P. F. Scott, M. Ryle, and A. Hewish. First Results of Radio Star Observations Using the Method of Aperture Synthesis. *Monthly Notices of the Royal Astronomical Society*, Vol. 122, No. 1, pp. 95–111, 1961.

[35] J. H. Blythe. A new type of pencil beam aerial for radio astronomy. *Monthly Notices of the RAS*, Vol. 117, p. 644, 1957.

[36] J. H. Blythe. Results of a survey of galactic radiation at 38 Mc/s. *Monthly Notices of the RAS*, Vol. 117, p. 652, 1957.

[37] K. I. Kellermann and J. M. Moran. The development of high-resolution imaging in radio astronomy. *Annual Review of Astronomy and Astrophysics*, Vol. 39, No. 1, pp. 457–509, 2001.

[38] A. R. Thompson, J. M. Moran, and J. Swenson, George W. *Interferometry and Synthesis in Radio Astronomy, 3rd Edition.* 2017.

[39] A. Labeyrie. Interference fringes obtained on Vega with two optical telescopes. *Astrophysical Journal, Letters*, Vol. 196, pp. L71–L75, 1975.

[40] M. Shao and D. H. Staelin. First fringe measurements with a phase-tracking stellar interferometer. *Appl. Opt.*, Vol. 19, No. 9, pp. 1519–1522, 1980.

[41] D. Mozurkewich, D. J. Hutter, K. J. Johnston, et al. Preliminary Measurements of Star Positions with the Mark III Stellar Interferometer. *Astronomical Journal*, Vol. 95, p. 1269, 1988.

[42] M. Shao and M. M. Colavita. Long-baseline optical and infrared stellar interferometry. *Annual Review of Astronomy and Astrophysics*, Vol. 30, No. 1, pp. 457–498, 1992.

[43] J. D. Monnier. Optical interferometry in astronomy. *Reports on Progress in Physics*, Vol. 66, No. 5, p. 789, 2003.

[44] S. Gillessen, F. Eisenhauer, G. Perrin, et al. GRAVITY: a four-telescope beam combiner instrument for the VLTI. *Optical and Infrared Interferometry II*, Vol. 7734 of *Society of Photo-Optical Instrumentation Engineers (SPIE) Conference Series*, p. 77340Y, 2010.

[45] B. Lopez, S. Lagarde, W. Jaffe, et al. An Overview of the MATISSE Instrument — Science, Concept and Current Status. *The Messenger*, Vol. 157, pp. 5–12, 2014.

[46] U. Bonse and M. Hart. An x-ray interferometer. *Applied Physics Letters*, Vol. 6, No. 8, pp. 155–156, 1965.

[47] W. C. Cash. Maxim: micro-arcsecond x-ray imaging mission. *Interferometry in Space*, Vol. 4852 of *Society of Photo-Optical Instrumentation Engineers (SPIE) Conference Series*, pp. 196–209, 2003.

[48] K. C. Gendreau, W. C. Cash, A. F. Shipley, et al. MAXIM Pathfinder x-ray interferometry mission. *X-Ray and Gamma-Ray Telescopes and Instruments for Astronomy.*, Vol. 4851 of *Society of Photo-Optical Instrumentation Engineers (SPIE) Conference Series*, pp. 353–364, 2003.

[49] W. Cash, A. Shipley, S. Osterman, et al. Laboratory detection of X-ray fringes with a grazing-incidence interferometer. *Nature*, Vol. 407, No. 6801, pp. 160–162, 2000.

[50] R. Willingale, G. Butcher, and T. J. Stevenson. The optical demonstration of an x-ray interferometer. *Optics for EUV, X-Ray, and Gamma-Ray Astronomy II*, Vol. 5900, p. 59001G. International Society for Optics and Photonics, SPIE, 2005.

[51] R. Willingale, G. I. Butcher, M. Ackermann, et al. A slatted mirror for an x-ray interferometer manufactured in silicon. *Optics for EUV, X-Ray, and Gamma-Ray Astronomy VI*, Vol. 8861, p. 88611S. International Society for Optics and Photonics, SPIE, 2013.

[52] R. Novick, M. C. Weisskopf, and others. Detection of X-Ray Polarization of the Crab Nebula. *Astrophysical Journal, Letters*, Vol. 174, p. L1, 1972.

[53] M. C. Weisskopf, E. H. Silver, and others. A precision measurement of the X-ray polarization of the Crab Nebula without pulsar contamination. *Astrophysical Journal, Letters*, Vol. 220, pp. L117–L121, 1978.

[54] K. S. Long, G. A. Chanan, and R. Novick. The X-ray polarization of the CYG sources. *Astrophysical Journal*, Vol. 238, pp. 710–716, 1980.

[55] M. C. Weisskopf, H. L. Kestenbaum, K. S. Long, et al. An upper limit to the linear X-ray polarization of Scorpius X-1. *Astrophysical Journal, Letters*, Vol. 221, pp. L13–L16, 1978.

[56] E. H. Silver, M. C. Weisskopf, H. L. Kestenbaum, et al. The first search for X-ray polarization in the Centaurus X-3 and Hercules X-1 pulsars. *Astrophysical Journal*, Vol. 232, pp. 248–254, 1979.

[57] M. C. Weisskopf, G. G. Cohen, H. L. Kestenbaum, et al. The X-ray polarization experiment on the OSO-8. In *NASA Special Publication*, Vol. 389, pp. 81–96. 1976.

[58] P. E. Kaaret, J. Schwartz, P. Soffitta, et al. Status of the stellar x-ray polarimeter for the Spectrum-X-Gamma mission. *X-Ray and Ultraviolet Polarimetry*, Vol. 2010, pp. 22 – 27. International Society for Optics and Photonics, SPIE, 1994.

[59] K. Jahoda. The Gravity and Extreme Magnetism Small Explorer. *Space Telescopes and Instrumentation 2010: Ultraviolet to Gamma Ray*, Vol. 7732 of *Society of Photo-Optical Instrumentation Engineers (SPIE) Conference Series*, p. 77320W, 2010.

[60] O. Klein and Y. Nishina. Über die streuung von strahlung durch freie elektronen nach der neuen relativistischen quantendynamik von dirac. *Zeitschrift für Physik*, Vol. 52, No. 11, pp. 853–868, 1929.

[61] M. Forot, P. Laurent, and others. Polarization of the Crab Pulsar and Nebula as Observed by the INTEGRAL/IBIS Telescope. *Astrophysical Journal*, Vol. 688, p. L29, 2008.

[62] A. J. Dean, D. J. Clark, and others. Polarized gamma-ray emission from the crab. *Science*, Vol. 321, No. 5893, pp. 1183–1185, 2008.

[63] E. Jourdain and J. P. Roques. 2003-2018 Monitoring of the Crab Nebula Polarization in Hard X-Rays with INTEGRAL SPI. *Astrophysical Journal*, Vol. 882, No. 2, p. 129, 2019.

[64] P. Laurent, J. Rodriguez, J. Wilms, et al. Polarized Gamma-Ray Emission from the Galactic Black Hole Cygnus X-1. *Science*, Vol. 332, No. 6028, p. 438, 2011.

[65] E. Jourdain, J. P. Roques, M. Chauvin, et al. Separation of two contributions to the high energy emission of cygnus x-1: Polarization measurements with integral spi*. *The Astrophysical Journal*, Vol. 761, No. 1, p. 27, 2012.

[66] H. Collaboration and others. Detection of polarized gamma-ray emission from the Crab nebula with the Hitomi Soft Gamma-ray Detector†. *Publications of the Astronomical Society of Japan*, Vol. 70, No. 6, 2018. 113.

[67] S. V. Vadawale, T. Chattopadhyay, N. P. S. Mithun, et al. Phase-resolved X-ray polarimetry of the Crab pulsar with the AstroSat CZT Imager. *Nature Astronomy*, Vol. 2, pp. 50–55, 2018.

[68] M. Chauvin, H. G. Florén, M. Friis, et al. Accretion geometry of the black-hole binary cygnus x-1 from x-ray polarimetry. *Nature Astronomy*, Vol. 2, No. 8, pp. 652–655, 2018.

[69] M. Chauvin, H. G. Florén, M. Friis, et al. The PoGO+ view on Crab off-pulse hard X-ray polarization. *Monthly Notices of the RAS*, Vol. 477, No. 1, p. L45, 2018.

[70] McGlynn, S., Clark, D. J., Dean, A. J., et al. Polarisation studies of the prompt gamma-ray emission from grb 041219a using the spectrometer aboard integral*. *A&A*, Vol. 466, No. 3, pp. 895–904, 2007.

[71] D. Götz, P. Laurent, F. Lebrun, F. Daigne, et al. Variable polarization measured in the prompt emission of grb 041219a using ibis on board integral. *The Astrophysical Journal*, Vol. 695, No. 2, p. L208, 2009.

[72] D. Yonetoku, T. Murakami, S. Gunji, et al. DETECTION OF GAMMA-RAY POLARIZATION IN PROMPT EMISSION OF GRB 100826a. *The Astrophysical Journal*, Vol. 743, No. 2, p. L30, 2011.

[73] D. Yonetoku, T. Murakami, S. Gunji, et al. Magnetic Structures in Gamma-Ray Burst Jets Probed by Gamma-Ray Polarization. *Astrophysical Journal, Letters*, Vol. 758, No. 1, p. L1, 2012.

[74] M. Kole, N. De Angelis, F. Berlato, et al. The POLAR gamma-ray burst polarization catalog. *Astronomy and Astrophysics*, Vol. 644, p. A124, 2020.

[75] J. Hulsman. POLAR-2: a large scale gamma-ray polarimeter for GRBs. In *Society of Photo-Optical Instrumentation Engineers (SPIE) Conference Series*, Vol. 11444 of *Society of Photo-Optical Instrumentation Engineers (SPIE) Conference Series*, p. 114442V, 2020.

[76] H. Feng, W. Jiang, M. Minuti, et al. PolarLight: a CubeSat X-ray polarimeter based on the gas pixel detector. *Experimental Astronomy*, Vol. 47, No. 1-2, pp. 225–243, 2019.

[77] H. Feng, H. Li, X. Long, et al. Re-detection and a possible time variation of soft x-ray polarization from the crab. *Nature Astronomy*, Vol. 4, No. 5, pp. 511–516, 2020.

[78] X. Long, H. Feng, H. Li, et al. A significant detection of x-ray polarization in sco x-1 with polarlight and constraints on the corona geometry. *The Astrophysical Journal Letters*, Vol. 924, No. 1, p. L13, 2022.

[79] H. Feng and R. Bellazzini. The x-ray polarimetry window reopens. *Nature Astronomy*, Vol. 4, No. 5, pp. 547–547, 2020.

[80] M. C. Weisskopf, B. Ramsey, and others. The imaging x-ray polarimetry explorer (ixpe). *Results in Physics*, Vol. 6, pp. 1179 – 1180, 2016.

[81] B. D. Ramsey, S. D. Bongiorno, J. K. Kolodziejczak, et al. Optics for the imaging x-ray polarimetry explorer. *Journal of Astronomical Telescopes, Instruments, and Systems*, Vol. 8, No. 2, p. 024003, 2022.

[82] L. Baldini, M. Barbanera, R. Bellazzini, et al. Design, construction, and test of the Gas Pixel Detectors for the IXPE mission. *Astroparticle Physics*, Vol. 133, p. 102628, 2021.

[83] J. Vink, D. Prokhorov, R. Ferrazzoli, et al. X-ray polarization detection of cassiopeia a with ixpe. *The Astrophysical Journal*, Vol. 938, No. 1, p. 40, 2022.

[84] R. Taverna, R. Turolla, F. Muleri, et al. Polarized x-rays from a magnetar. *Science*, Vol. 378, No. 6620, pp. 646–650, 2022.

[85] S. L. O'Dell, P. Attinà, L. Baldini, et al. The Imaging X-Ray Polarimetry Explorer (IXPE): technical overview II. *UV, X-Ray, and Gamma-Ray Space Instrumentation for Astronomy XXI*, Vol. 11118, p. 111180V. International Society for Optics and Photonics, SPIE, 2019.

[86] K. Hayashida, H. Kurubi, H. Nakajima, et al. A new type of multiple image x-ray interferometer for arcseconds and sub-arcseconds sources. *Space Telescopes and Instrumentation 2016: Ultraviolet to Gamma Ray*, Vol. 9905, pp. 1563 – 1570. International Society for Optics and Photonics, SPIE, 2016.

[87] T. Mihara, M. Nakajima, M. Sugizaki, et al. Gas Slit Camera (GSC) onboard MAXI on ISS. *Publications of the Astronomical Society of Japan*, Vol. 63, No. sp3, pp. S623–S634, 2011.

[88] M. Sugizaki, T. Mihara, M. Serino, et al. In-Orbit Performance of MAXI Gas Slit Camera (GSC) on ISS. *Publications of the Astronomical Society of Japan*, Vol. 63, No. sp3, pp. S635–S644, 2011.

[89] H. Tsunemi, H. Tomida, H. Katayama, et al. In-Orbit Performance of the MAXI/SSC onboard the ISS. *Publications of the Astronomical Society of Japan*, Vol. 62, No. 6, pp. 1371–1379, 2010.

[90] H. Tomida, H. Tsunemi, M. Kimura, et al. Solid-State Slit Camera (SSC) Aboard MAXI. *Publications of the Astronomical Society of Japan*, Vol. 63, pp. 397–405, 2011.

[91] K. Asakura, K. Hayashida, T. Kawabata, et al. Multi-image x-ray interferometer module: I. design concept and proof-of-concept experiments with fine-pitch slits. *Journal of Astronomical Telescopes, Instruments, and Systems*, in prep.

[92] H. Talbot, Esq. F.R.S. Lxxvi. facts relating to optical science. no. iv. *The London, Edinburgh, and Dublin Philosophical Magazine and Journal of Science*, Vol. 9, No. 56, pp. 401–407, 1836.

[93] Lord Rayleigh F.R.S. Xxv. on copying diffraction-gratings, and on some phenomena connected therewith. *The London, Edinburgh, and Dublin Philosophical Magazine and Journal of Science*, Vol. 11, No. 67, pp. 196–205, 1881.

[94] A. Momose, S. Kawamoto, I. Koyama, et al. Demonstration of X-Ray Talbot Interferometry. *Japanese Journal of Applied Physics*, Vol. 42, No. 7B, p. 866, 2003.

[95] F. Pfeiffer, T. Weitkamp, O. Bunk, et al. Phase retrieval and differential phase-contrast imaging with low-brilliance X-ray sources. *Nature Physics*, Vol. 2, No. 4, pp. 258–261, 2006.

[96] J. Wen, Y. Zhang, and M. Xiao. The talbot effect: recent advances in classical optics, nonlinear optics, and quantum optics. *Adv. Opt. Photon.*, Vol. 5, No. 1, pp. 83–130, 2013.

[97] J. W. Goodman. *Introduction to Fourier optics*. 2005.

[98] A. Takeda, T. G. Tsuru, T. Tanaka, et al. Improvement of spectroscopic performance using a charge-sensitive amplifier circuit for an X-ray astronomical SOI pixel detector. *Journal of Instrumentation*, Vol. 10, No. 6, p. C06005, 2015.

[99] S. Goto, K. Takeshita, Y. Suzuki, et al. Construction and commissioning of a 215-m-long beamline at spring-8. *Nuclear Instruments and Methods in Physics Research Section A: Accelerators, Spectrometers, Detectors and Associated Equipment*, Vol. 467-468, pp. 682–685, 2001. 7th Int.Conf. on Synchrotron Radiation Instrumentation.

[100] T. Yokoyama, M. Tsutsui, and others. High performance 2.5um global shutter pixel with new designed light-pipe structure. In *2018 IEEE International Electron Devices Meeting (IEDM)*, pp. 10.5.1–10.5.4, 2018.

[101] T. Tanaka, H. Uchida, H. Nakajima, et al. Soft X-ray Imager aboard Hitomi (ASTRO-H). *Journal of Astronomical Telescopes, Instruments, and Systems*, Vol. 4, p. 011211, 2018.

[102] K. Asakura, K. Hayashida, and others. X-ray imaging polarimetry with a 2.5-μm pixel cmos sensor for visible light at room temperature. *Journal of Astronomical Telescopes, Instruments, and Systems*, Vol. 5, No. 3, pp. 1 – 7, 2019.

[103] K. Asakura, K. Hayashida, T. Hanasaka, et al. Subsub-arcseconds x-ray imaging with multi-image x-ray interferometer module (MIXIM): experimental results. *Space Telescopes and Instrumentation 2020: Ultraviolet to Gamma Ray*, Vol. 11444, p. 114441D. International Society for Optics and Photonics, SPIE, 2020.

[104] H. Tsunemi, K. Mori, E. Miyata, et al. Improvement of the spatial resolution of the acis using split-pixel events. *The Astrophysical Journal*, Vol. 554, No. 1, p. 496, 2001.

[105] K. Patorski and S. Kozak. Self-imaging with nonparabolic approximation of spherical wave fronts. *J. Opt. Soc. Am. A*, Vol. 5, No. 8, pp. 1322–1327, 1988.

[106] K. Asakura, K. Hayashida, S. Sakuma, et al. Sub-arcsecond x-ray imaging with Multi-Image X-ray Interferometer Module (MIXIM): introduction of a periodic coded-aperture mask. *Space Telescopes and Instrumentation 2022: Ultraviolet to Gamma Ray*, Vol. 12181, p. 1218129. International Society for Optics and Photonics, SPIE, 2022.

[107] M. J. Cieślak, K. A. Gamage, and R. Glover. Coded-aperture imaging systems: Past, present and future development – a review. *Radiation Measurements*, Vol. 92, pp. 59–71, 2016.

[108] S. R. Gottesman and E. E. Fenimore. New family of binary arrays for coded aperture imaging. *Appl. Opt.*, Vol. 28, No. 20, pp. 4344–4352, 1989.

[109] A. P. Dempster, N. M. Laird, and D. B. Rubin. Maximum likelihood from incomplete data via the em algorithm. *Journal of the Royal Statistical Society. Series B (Methodological)*, Vol. 39, No. 1, pp. 1–38, 1977.

[110] L. A. Shepp and Y. Vardi. Maximum likelihood reconstruction for emission tomography. *IEEE Trans Med Imaging*, Vol. 1, No. 2, pp. 113–122, 1982.

[111] B. Efron. Missing data, imputation, and the bootstrap. *Journal of the American Statistical Association*, Vol. 89, No. 426, pp. 463–475, 1994.

[112] P. A. Ruud. Extensions of estimation methods using the em algorithm. *Journal of Econometrics*, Vol. 49, No. 3, pp. 305–341, 1991.

[113] J. Janesick, T. Elliott, S. Collins, et al. CCD advances for X-ray scientific measurements in 1985. *X-ray instrumentation in astronomy*, Vol. 597 of *Proceedings of the International Society for Optical Engineering*, pp. 364–380, 1986.

[114] H. Tsunemi, K. Hayashida, and others. Detection of x-ray polarization with a charge coupled device. *Nuclear Instruments and Methods in Physics Research Section A: Accelerators, Spectrometers, Detectors and Associated Equipment*, Vol. 321, No. 3, pp. 629 – 631, 1992.

[115] G. Buschhorn, R. Kotthaus, W. Kufner, et al. X-ray polarimetry using the photoeffect in a ccd detector. *Nuclear Instruments and Methods in Physics Research Section A: Accelerators, Spectrometers, Detectors and Associated Equipment*, Vol. 346, No. 3, pp. 578 – 588, 1994.

[116] K. Hayashida, S. Tanaka, H. Tsunemi, Y. Hashimoto, et al. Optimization of polarimetry sensitivity for x-ray ccd. *Nuclear Instruments and Methods in Physics Research Section A: Accelerators, Spectrometers, Detectors and Associated Equipment*, Vol. 436, No. 1, pp. 96 – 101, 1999.

[117] J. Katsuta, T. Mizuno, Y. Ogasaka, et al. Evaluation of polarization characteristics of multilayer mirror for hard x-ray observation of astrophysical objects. *Nuclear Instruments and Methods in Physics Research Section A: Accelerators, Spectrometers, Detectors and Associated Equipment*, Vol. 603, No. 3, pp. 393–400, 2009.

[118] S. Agostinelli, J. Allison, and others. Geant4—a simulation toolkit. *Nuclear Instruments and Methods in Physics Research Section A: Accelerators, Spectrometers, Detectors and Associated Equipment*, Vol. 506, No. 3, pp. 250 – 303, 2003.

[119] J. Allison, K. Amako, and others. Geant4 developments and applications. *IEEE Transactions on Nuclear Science*, Vol. 53, No. 1, pp. 270–278, 2006.

[120] J. Allison, K. Amako, and others. Recent developments in geant4. *Nuclear Instruments and Methods in Physics Research Section A: Accelerators, Spectrometers, Detectors and Associated Equipment*, Vol. 835, pp. 186 – 225, 2016.

[121] J. Krizmanic, G. Skinner, Z. Arzoumanian, et al. Phase Fresnel Lens Development for X-ray and Gamma-ray Astronomy. *arXiv e-prints*, p. arXiv:2008.12810, 2020.

[122] H. Noda, T. Hayashi, S. Yamada, et al. Position-sensitive transition edge sensor with sub-micrometer accuracy developed for future x-ray interferometry mission. *Space Telescopes and Instrumentation 2022: Ultraviolet to Gamma Ray*, Vol. 12181, p. 121812D. International Society for Optics and Photonics, SPIE, 2022.

[123] K. Hayashida, K. Asakura, A. Ishikura, et al. Sub-arcseconds to micro-arcsecond x-ray imaging with multi image x-ray interferometer method (MIXIM): concept and scalabe mission plans. *Space Telescopes and Instrumentation 2020: Ultraviolet to Gamma Ray*, Vol. 11444, p. 114441C. International Society for Optics and Photonics, SPIE, 2020.

[124] M. Chauvin, H. G. Florén, M. Friis, et al. Shedding new light on the Crab with polarized X-rays. *Scientific Reports*, Vol. 7, p. 7816, 2017.

[125] R. A. Cameron, T. L. Aldcroft, W. A. Podgorski, et al. Initial performance of the attitude control and aspect determination subsystems on the Chandra Observatory. *X-Ray Optics, Instruments, and Missions III*, Vol. 4012 of *Society of Photo-Optical Instrumentation Engineers (SPIE) Conference Series*, pp. 658–668, 2000.

[126] C. M. Pong. On-orbit performance & operation of the attitude & pointing control subsystems on asteria. 2018.

[127] M. Markevitch, M. W. Bautz, and others. Chandra Spectra of the Soft X-Ray Diffuse Background. *Astrophysical Journal*, Vol. 583, No. 1, pp. 70–84, 2003.

[128] Carter, J. A. and Read, A. M. The xmm-newton epic background and the production of background blank sky event files*. *A&A*, Vol. 464, No. 3, pp. 1155–1166, 2007.

[129] K. Koyama, H. Tsunemi, T. Dotani, et al. X-Ray Imaging Spectrometer (XIS) on Board Suzaku. *Publications of the Astronomical Society of Japan*, Vol. 59, pp. 23–33, 2007.

[130] D. A. Smith and A. S. Wilson. A Chandra Observation of the Circinus Galaxy. *Astrophysical Journal*, Vol. 557, No. 1, pp. 180–192, 2001.

[131] A. J. Young, A. S. Wilson, and P. L. Shopbell. A Chandra X-Ray Study of NGC 1068. I. Observations of Extended Emission. *Astrophysical Journal*, Vol. 556, No. 1, pp. 6–23, 2001.

[132] M. L. Jones, K. Parker, G. Fabbiano, et al. Extended X-Ray Emission in Compton Thick AGN with Deep Chandra Observations. *Astrophysical Journal*, Vol. 910, No. 1, p. 19, 2021.

[133] T. Izumi, K. Wada, R. Fukushige, S. Hamamura, et al. Circumnuclear multiphase gas in the circinus galaxy. ii. the molecular and atomic obscuring structures revealed with alma. *The Astrophysical Journal*, Vol. 867, No. 1, p. 48, 2018.

[134] K. R. W. Tristram, K. Meisenheimer, W. Jaffe, et al. Resolving the complex structure of the dust torus in the active nucleus of the circinus galaxy. *A&A*, Vol. 474, No. 3, pp. 837–850, 2007.

[135] K. R. W. Tristram, L. Burtscher, W. Jaffe, et al. The dusty torus in the Circinus galaxy: a dense disk and the torus funnel. *Astronomy and Astrophysics*, Vol. 563, p. A82, 2014.

[136] S. Molendi, S. Bianchi, and G. Matt. Iron and nickel line properties in the X-ray-reflecting region of the Circinus galaxy. *Monthly Notices of the RAS*, Vol. 343, No. 1, pp. L1–L4, 2003.

[137] X. W. Shu, T. Yaqoob, and J. X. Wang. Chandra high-energy grating observations of the fe kα line core in type ii seyfert galaxies: A comparison with type i nuclei. *The Astrophysical Journal*, Vol. 738, No. 2, p. 147, 2011.

[138] S. Corbel, R. P. Fender, A. K. Tzioumis, et al. Large-Scale, Decelerating, Relativistic X-ray Jets from the Microquasar XTE J1550-564. *Science*, Vol. 298, No. 5591, pp. 196–199, 2002.

[139] S. Migliari, R. Fender, and M. Méndez. Iron Emission Lines from Extended X-ray Jets in SS 433: Reheating of Atomic Nuclei. *Science*, Vol. 297, No. 5587, pp. 1673–1676, 2002.

[140] H. L. Marshall, D. E. Harris, J. P. Grimes, et al. Structure of the X-Ray Emission from the Jet of 3C 273. *Astrophysical Journal, Letters*, Vol. 549, No. 2, pp. L167–L171, 2001.

[141] J. C. A. Miller-Jones, A. Bahramian, J. A. Orosz, et al. Cygnus X-1 contains a 21-solar mass black hole—Implications for massive star winds. *Science*, Vol. 371, No. 6533, pp. 1046–1049, 2021.

[142] Zanin, R., Fernández-Barral, A., de Oña Wilhelmi, E., et al. Gamma rays detected from cygnus with likely jet origin. *A&A*, Vol. 596, p. A55, 2016.

[143] K. Makishima, H. Takahashi, S. Yamada, et al. Suzaku Results on Cygnus X-1 in the Low/Hard State. *Publications of the Astronomical Society of Japan*, Vol. 60, p. 585, 2008.

[144] D. Kantzas, S. Markoff, T. Beuchert, et al. A new lepto-hadronic model applied to the first simultaneous multiwavelength data set for Cygnus X-1. *Monthly Notices of the RAS*, Vol. 500, No. 2, pp. 2112–2126, 2021.

[145] M. L. Parker, J. A. Tomsick, J. M. Miller, et al. NuSTAR and Suzaku Observations of the Hard State in Cygnus X-1: Locating the Inner Accretion Disk. *Astrophysical Journal*, Vol. 808, No. 1, p. 9, 2015.

[146] C. R. Canizares, D. P. Huenemoerder, D. S. Davis, et al. High-Resolution X-Ray Spectra of Capella: Initial Results from the Chandra High-Energy Transmission Grating Spectrometer. *Astrophysical Journal, Letters*, Vol. 539, No. 1, pp. L41–L44, 2000.

[147] G. Torres, A. Claret, and P. A. Young. Binary orbit, physical properties, and evolutionary state of capella (α aurigae). *The Astrophysical Journal*, Vol. 700, No. 2, p. 1349, 2009.

[148] J. H. M. M. Schmitt and F. Favata. Continuous heating of a giant X-ray flare on Algol. *Nature*, Vol. 401, No. 6748, pp. 44–46, 1999.

[149] E. Franciosini, R. Pallavicini, and G. Tagliaferri. BeppoSAX observation of a large long-duration X-ray flare from UX Arietis. *Astronomy and Astrophysics*, Vol. 375, pp. 196–204, 2001.

[150] R. A. Osten, A. Brown, T. R. Ayres, et al. A Multiwavelength Perspective of Flares on HR 1099: 4 Years of Coordinated Campaigns. *Astrophysical Journal, Supplement*, Vol. 153, No. 1, pp. 317–362, 2004.

[151] T. Kosugi, K. Matsuzaki, T. Sakao, et al. The Hinode (Solar-B) Mission: An Overview. *Solar Physics*, Vol. 243, No. 1, pp. 3–17, 2007.

[152] T. Kosugi, T. Sakao, S. Masuda, et al. The Hard X-Ray Telescope (HXT) Onboard Yohkoh: Its Performance and Some Initial Results. *Publications of the Astronomical Society of Japan*, Vol. 44, pp. L45–L49, 1992.